

# Efficient Simulation of Molecular Gas Transport for Micro- and Nanoscale Applications

by

Gregg Arthur Radtke

Submitted to the Department of Mechanical Engineering  
in partial fulfillment of the requirements for the degree of

Doctor of Philosophy in Mechanical Engineering

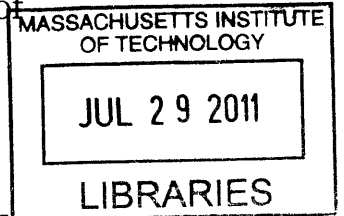
at the

MASSACHUSETTS INSTITUTE OF TECHNOLOGY

June 2011

© Massachusetts Institute of Technology 2011. All rights reserved.

**ARCHIVES**



Author .....  
Department of Mechanical Engineering  
May 19, 2011

Certified by .....  
Nicolas G. Hadjiconstantinou  
Associate Professor  
Thesis Supervisor

Accepted by .....  
David E. Hardt  
Chairman, Department Committee on Graduate Theses



# Efficient Simulation of Molecular Gas Transport for Micro- and Nanoscale Applications

by

Gregg Arthur Radtke

Submitted to the Department of Mechanical Engineering  
on May 19, 2011, in partial fulfillment of the  
requirements for the degree of  
Doctor of Philosophy in Mechanical Engineering

## Abstract

We describe and validate an efficient method for simulating the Boltzmann transport equation in regimes typically encountered in nanotechnology applications. These transport regimes are characterized by nonvanishing Knudsen numbers, preventing simple analyses based on the Navier-Stokes equations; and also by small departures from equilibrium (low Mach number, small temperature gradients, etc.), which make the traditional particle methods like the direct simulation Monte Carlo (DSMC) computationally inefficient.

By considering only the deviation from equilibrium, the low-variance particle method introduced herein, simulates molecular gas transport in near-equilibrium regimes with drastically reduced statistical noise compared to the DSMC method. Compared to previous variance reduction methods, the present approach is able to simulate the more general variable-hard-sphere collision model, which more accurately captures the viscosity dependence on the temperature of real gases, compared to the hard sphere and Bhatnagar-Gross-Krook collision models developed previously. The present formulation uses collision algorithms with no inherent time step error, for improved accuracy. Finally, by using a mass-conservative formulation, accurate simulations can be performed in the transition regime requiring as few as ten particles per cell, which is a drastic improvement over previous approaches and enables efficient simulation of multidimensional problems at arbitrarily small deviation from equilibrium.

The new methodology is validated and its capabilities are illustrated by solving a number of benchmark problems. It is subsequently used to evaluate the second-order temperature jump coefficient of a dilute hard sphere gas for the first time.

Thesis Supervisor: Nicolas G. Hadjiconstantinou  
Title: Associate Professor



## Acknowledgments

First and foremost, I would like to thank my adviser, Prof. Nicolas Hadjiconstantinou for taking me into his group, and introducing me to the exciting world of variance-reduced particle simulation methods. Throughout this project and without exception, it has been an absolute pleasure working with him; I appreciate his consistently calm demeanor and patience, excellent sense of humor, and exceptional scientific insight. I would also like to thank the other members of my committee: Prof. Anthony Patera for his deep expertise in mathematics and numerical methods, and Prof. Gang Chen for his broad perspectives on nanoscience and engineering, as well as helping me come to MIT initially.

I am also grateful for the opportunity to spend several delightful semesters as a teacher's assistant for Prof. Bora Mikic, who is undoubtedly the most interesting person I have ever met. I will miss the long afternoon discussions about philosophy, medicine, history, current world events; as well as math, science, and engineering. I would also like to thank Prof. Ian Hunter for getting me involved in a very rewarding consulting experience, which was valuable for my career development.

The current and former members of the Nanoscale Kinetic Transport and Simulation Group—Husain Al-Mohssen, Ghassan Fayad, Colin Landon, Jean-Phillipe Péraud, Toby Klein, Jessica Armour—have provided an often entertaining, but usually productive atmosphere for performing my research. In particular, I will miss the animated discussions with Husain, the many early evening “cannons” with Jean-Phillipe, and the wonderful time hanging out at the RGD conference in northern California with Colin and his wife. I am also thankful for the many friendships I have maintained from the Nanoengineering Group: Vincent Bérubé, Anurag Bajpayee, Daniel Kraemer, Andy Muto, and Jivtesh Garg.

I am grateful to my friends and family from Arizona who have kept up with me despite the long geographical distance. In particular, my parents Art and Lois, my sister Lisa, my brother Scott, my nieces Lauren and Taylor, my nephew Brett, and my friends Daniel Hiemann, Mark Birney, and John Keffler. The many phone calls,

and occasional visits have made the busy times more tractable, and I am glad to have maintained these friendships, with the hope of continuing them as I move back out West.

# Contents

<b>1</b>	<b>Introduction</b>	<b>17</b>
1.1	Particle description of rarefied gas transport . . . . .	20
1.1.1	The variable hard sphere collision model . . . . .	21
1.1.2	The Bhatnagar-Gross-Krook collision model . . . . .	21
1.1.3	Hydrodynamic properties . . . . .	22
1.1.4	Maxwell accommodation boundary interaction model . . . . .	23
1.2	The direct simulation Monte Carlo method . . . . .	24
1.2.1	Collision step . . . . .	25
1.2.2	Hydrodynamic variables . . . . .	26
1.2.3	Rate of convergence . . . . .	26
1.2.4	Statistical error . . . . .	26
1.3	Previous work . . . . .	28
1.3.1	Deviational particle methods . . . . .	29
1.3.2	Weight based methods . . . . .	31
<b>2</b>	<b>Simulating Deviation from Equilibrium</b>	<b>33</b>
2.1	Decomposition of the velocity distribution . . . . .	33
2.2	Deviation from a global equilibrium . . . . .	34
2.3	Deviation from a local equilibrium . . . . .	35
2.4	Discussion . . . . .	37
<b>3</b>	<b>A Mass-conservative Low Variance Simulation Method</b>	<b>41</b>
3.1	Computational method . . . . .	41

3.2	Advection step . . . . .	43
3.2.1	Particle generation at the boundaries . . . . .	45
3.2.2	Mass conservation enforcement . . . . .	50
3.3	Effective body force . . . . .	51
3.3.1	Mass conservation . . . . .	54
3.4	Property evaluation . . . . .	54
3.5	Time integration . . . . .	55
<b>4</b>	<b>Simulation of the Variable Hard Sphere Gas</b>	<b>57</b>
4.1	Alternative form of the VHS collision operator . . . . .	57
4.2	Stochastic collision time steps . . . . .	61
4.3	Particle creation . . . . .	63
4.3.1	Sampling particle trial particle velocities from the $K_{\beta,\max}^{(2)}$ term	67
4.3.2	Sampling particle trial particle velocities from the $K_{\beta,\max}^{(1)}$ term	68
4.4	Particle deletion . . . . .	69
4.5	Mass conservation . . . . .	70
<b>5</b>	<b>Simulation of the Bhatnagar-Gross-Krook Gas</b>	<b>73</b>
5.1	Stochastic collision time steps . . . . .	74
5.2	Particle creation . . . . .	77
<b>6</b>	<b>Validation and Performance</b>	<b>79</b>
6.1	Convergence . . . . .	79
6.2	Variance reduction . . . . .	82
6.3	Validation and demonstration cases . . . . .	83
6.3.1	Couette flow shear stress for the VHS collision model . . . . .	84
6.3.2	Poiseuille and thermal creep flow in rectangular microchannels	84
6.3.3	Lid-driven flow of argon gas . . . . .	87
6.3.4	Response of a gas to a spatially-variable boundary temperature	88
6.3.5	BGK collision model simulations . . . . .	92

<b>7</b>	<b>Selected Applications</b>	<b>95</b>
7.1	Simulation of Knudsen compressors . . . . .	95
7.2	Second order temperature jump . . . . .	96
7.2.1	Theory . . . . .	97
7.2.2	Implementation . . . . .	99
7.2.3	Results . . . . .	102
<b>8</b>	<b>Conclusion</b>	<b>107</b>
<b>A</b>	<b>Particle Sampling Methods</b>	<b>111</b>
A.1	Direct inversion of the cumulative distribution function . . . . .	111
A.1.1	Sampling from an exponential distribution . . . . .	112
A.1.2	Sampling from a Gaussian distribution . . . . .	112
A.1.3	Sampling from a biased Gaussian distribution . . . . .	112
A.1.4	Sampling uniformly from a unit sphere . . . . .	113
A.2	The acceptance-rejection method . . . . .	113
A.3	The ratio-of-uniforms method . . . . .	113
A.3.1	Ratio-of-uniforms sampling of a product of a polynomial and a Gaussian . . . . .	114
A.3.2	Ratio of uniforms sampling of $2\xi^3 e^{-\xi^2}$ . . . . .	117
<b>B</b>	<b>Mass-conservative Simulation Based on a Local Equilibrium</b>	<b>119</b>
B.1	Advection step . . . . .	120
B.2	Collision step . . . . .	122
	<b>Bibliography</b>	<b>124</b>



# List of Figures

1-1	Temperature field (contours) and heat flux distribution (vectors) for the response of argon to an impulsively changed temperature on a $2\lambda$ wide section of its boundary. The DSMC method and the method described in this thesis (denoted as LVDSMC) are compared at a time $t = 10\lambda/c_0$ , showing dramatically improved efficiency for latter method. Both simulations required similar computational resources. . . . .	28
2-1	Transient Couette flow of a BGK gas at $Kn = 0.2/\sqrt{\pi}$ . The LVDSMC result is based on deviation from a spatially-variable equilibrium; six snapshots are shown in blue. A DSMC solution corresponding to the final snapshot and using the same computational resources is shown in red. . . . .	37
2-2	Comparison of the total number of samples required (in arbitrary units) to achieve a fixed level of statistical error in the cell near a wall for steady-state Couette flow simulations of a BGK gas, for deviational approaches based on global and local equilibrium distributions. . . . .	38
6-1	Average number of deviational particles per cell for heat transfer through a layer of argon gas confined between diffusely-reflecting parallel plates at $Kn = 0.1$ . The data (symbols) are shown in terms of the convergence parameters $(\Delta x, \Xi)$ , while the line indicates $\overline{N}_C = \Xi$ , for comparison. . . . .	81

6-2	Absolute error in the steady state heat flux for argon gas confined between diffusely reflecting parallel plates at $Kn = 0.1$ as a function of the parameter $\Xi$ and spatial cell size $\Delta x$ . As discussed in the text $\Delta x$ also controls the time step size through $\Delta t = \Delta x/c_0$ . . . . .	82
6-3	Variance in the cell-based temperature measurement for heat transfer between parallel plates, averaged between two cells adjacent to the wall. The LVDSMC results (symbols) are obtained from simulations, compared to the DSMC values (solid line) obtained from Equation (1.25). . . . .	84
6-4	Validation of the LVDSMC VHS simulation method using a steady shear flow simulation at $Kn = 0.05$ . Shear stress values for hard sphere, helium, argon, and Maxwell molecular gases are considered. . . . .	85
6-5	Flow rate for Poiseuille flow through a rectangular microchannel for various Knudsen numbers and aspect ratios. The LVDSMC results (symbols) are compared with data from Doi [24] (lines). . . . .	86
6-6	Flow rate for thermal creep flow through a rectangular microchannel for various Knudsen numbers and aspect ratios. The LVDSMC results (symbols) are compared with data from Doi [24] (lines). . . . .	87
6-7	Streamwise velocity for Poiseuille flow through a square microchannel with $Kn = 0.1$ . . . . .	88
6-8	Lid-driven flow of argon gas at $Kn = 0.1$ . The contour lines show the density $\epsilon^{-1}(\rho/\rho_0 - 1)$ , while the velocity field $\epsilon^{-1}\mathbf{u}/c_0$ is shown as a vector plot. . . . .	89
6-9	Lid-driven flow of argon gas at $Kn = 1$ . The contour lines show the density $\epsilon^{-1}(\rho/\rho_0 - 1)$ , while the velocity field $\epsilon^{-1}\mathbf{u}/c_0$ is shown as a vector plot. . . . .	89
6-10	Lid-driven flow of argon gas at $Kn = 10$ . The contour lines show the density $\epsilon^{-1}(\rho/\rho_0 - 1)$ , while the velocity field $\epsilon^{-1}\mathbf{u}/c_0$ is shown as a vector plot. . . . .	90

6-11	Response of argon gas to spatially-varying boundary temperature with $Kn = 1$ and $\epsilon \ll 1$ . The contour lines are isotherms (dimensionless temperature: $\epsilon^{-1}(T/T_0 - 1)$ ), while the velocity field $\epsilon^{-1}\mathbf{u}/c_0$ is shown as a vector plot. . . . .	91
6-12	Response of argon gas to spatially-varying boundary temperature with $Kn = 1$ and $\epsilon = 0.05$ . Contour plot of the dimensionless temperature ( $\epsilon^{-1}(T/T_0 - 1)$ ) as obtained by LVDSMC (dashed) and DSMC (solid); the $\epsilon \rightarrow 0$ limit (dash-dot) as obtained by LVDSMC is also shown for comparison. The velocity field $\epsilon^{-1}\mathbf{u}/c_0$ is the LVDSMC solution for $\epsilon = 0.05$ ; the DSMC velocity field was noticeably noisier. . . . .	91
6-13	Response of argon gas to spatially-varying boundary temperature with $Kn = 1$ and $\epsilon = 0.5$ . Contour plot of the dimensionless temperature ( $\epsilon^{-1}(T/T_0 - 1)$ ) as obtained by LVDSMC (dashed) and DSMC (solid). The velocity field $\epsilon^{-1}\mathbf{u}/c_0$ is the LVDSMC solution for $\epsilon = 0.5$ . . . . .	92
6-14	Validation of the LVDSMC simulation method for steady Couette flow of a BGK gas. The Knudsen numbers $k = \frac{\sqrt{\pi}}{2}Kn$ are based on the separation width, and the shear stress is normalized by the free molecular flow limit $(-P_{xy})_{k \rightarrow \infty} = \frac{1}{\sqrt{\pi}}c_0U$ , where the bounding walls have (tangential) velocities $\pm U/2$ . . . . .	93
6-15	Validation of the LVDSMC simulation method for the transient temperature response of a BGK gas with Knudsen number $k = \frac{\sqrt{\pi}}{2}Kn = 0.2$ and initial state $(\rho_0, T_0)$ . Here, the LVDSMC (lines) and DSMC (symbols) results are shown for times $c_0t/L = \{0.02, 0.04, 0.1, 0.2, 0.4, 1, 2\}$ . The temperature is shown in dimensionless form, scaled by the characteristic temperature rise $\Delta T = 0.5T_0$ . . . . .	94
7-1	Simulation of a simple Knudsen compressor with $Kn = 1$ and arbitrarily small temperature gradients. The arrows are velocity vectors and the contours are isothermal lines. . . . .	97

7-2	Fits used to extract the second-order jump coefficient $d_2$ for the hard sphere and BGK collision models. . . . .	103
7-3	Second-order temperature jump solution (Equation (7.6)) to the uniform heat generation problem with Knudsen number $Kn = 0.05$ , where the simulation results (symbols) are compared to the first- (dashed line) and second-order (solid line) jump theories. . . . .	104
7-4	Second-order temperature jump solution (Equation (7.6)) to the uniform heat generation problem with Knudsen number $Kn = 0.1$ , where the simulation results (symbols) are compared to the first- (dashed line) and second-order (solid line) jump theories. . . . .	105

# List of Tables

A.1 Ratio of uniforms bounds . . . . .	114
--	-----



# Chapter 1

## Introduction

In gas flows in which the system length scale is on the order of or smaller than the mean free path  $\lambda$  (the average distance travelled by molecules between successive collisions), the conventional Navier-Stokes (NS) description of fluid dynamics breaks down. Transport in this regime can be described by the Boltzmann Transport Equation (BTE), an integro-differential equation which is difficult to solve in general. Although a variety of techniques have been used to obtain solutions, the prevalent numerical method for solving the BTE is a stochastic particle method known as direct simulation Monte Carlo (DSMC) [14].

At the time of its development, applications for DSMC simulations were motivated by the need to simulate high-altitude, hypersonic flows—a flow regime characterized by large departures from equilibrium conditions. Departure from equilibrium can be characterized by the fundamental inhomogeneity in the physical problem: typically, this is appears as a Mach number ( $Ma$ , i.e. the ratio of the characteristic velocity to the speed of sound) or a dimensionless temperature difference ( $\Delta T/T_0$ , where  $T_0$  is the temperature at reference conditions). The breakdown of NS under these conditions arises from the fact that in the upper atmosphere, due to the low pressure, the molecular mean free path can be large and approach (or exceed) the characteristic length scale of the system of interest. The impressive efficiency of the DSMC approach for this class of problems led to its widespread adoption as the standard method for general rarefied gas flows.

However, more recent applications have focused on the simulation of gas flows in small scale devices under conditions close to equilibrium ( $Ma \ll 1$ ,  $\Delta T/T_0 \ll 1$ ), such as MEMS and NEMS (micro- and nanoelectromechanical) devices. In this case, NS breakdown typically occurs because the system length scale  $L$  is small enough to be on the order of or smaller than the mean free path  $\lambda$  ( $\sim 50$  nm for air at standard conditions). In this regime, the standard stochastic particle methods like DSMC are not so efficient because statistical noise dominates the hydrodynamic signal of interest. For example, Gallis, et. al [25] who used DSMC to calculate the pressure and velocity fields arising from a oscillating microbeam, report that, due to the low flow speeds induced, “very long averaging times” (essentially requiring supercomputing facilities) were required to get a sufficiently smooth solution. As a result, researchers have encountered difficulty using DSMC in such situations, many choosing instead more computationally efficient approximate methods.

For example, Frangi et al. [23] numerically analyzed the gas-phase damping effect on the dynamics of a MEMS accelerometer. The low flow speeds involved would result in a very noisy DSMC simulation, prompting the author to use a PDE-based approach employing the Bhatnagar-Gross-Krook (BGK) collision model, which is only an approximation to the full BTE which DSMC solves. In another study, Han et al. [30] used the DSMC method to simulate flow through a Knudsen compressor, a small-scale device with no moving parts that induces a gas flow as a result of an imposed temperature gradient. In this study, an artificially large temperature gradient was simulated in order to improve the signal-to-noise ratio due to the excessive levels of statistical noise.<sup>1</sup>

This shift in focus—from highly non-equilibrium flows to near-equilibrium flows—has led to significant research activity on low-noise methods for solving gas transport problems. These studies can be roughly divided into three categories: mathematical analysis of the linearized Boltzmann equation, PDE-based methods, and variance-reduced stochastic particle methods. Studies of the linearized Boltzmann equation,

---

<sup>1</sup>For comparison, a noise-free simulation of a Knudsen compressor using the method outlined in this thesis, operating under an arbitrarily small temperature gradient, is presented in Section 7.1.

are typically mathematical in nature [18, 57], and have led to many high quality numerical solutions of fundamental problems. Although they are relevant to many important applications, they are inadequate to treat more general multidimensional problems in complex geometries encountered in MEMS/NEMS devices. PDE-based methods for solving the BTE have the advantage of avoiding the noise issues of stochastic particle methods, but they require considerably more computational resources. This added computational expense is due, primarily, to the high dimensionality of the velocity distribution function  $f(\mathbf{c}, \mathbf{x}, t)$ —the dependent variable appearing in the BTE—which is in general a function of three spatial coordinates ( $\mathbf{x}$ ), three molecular velocities ( $\mathbf{c}$ ), and time ( $t$ ).

Variance-reduced stochastic particle methods have recently been developed in order to efficiently simulate these near-equilibrium flows [9, 22, 33, 52, 29, 53]. Presented in this thesis is an advanced variance-reduced stochastic particle method for solving the BTE. This method features a more general collision algorithm with improved convergence properties, as well as the ability to simulate more general gas interaction models; moreover, we present new algorithms which provide sizable efficiency improvement over acceptance rejection methods; finally, we present algorithms that feature exact mass conservation which is essential for simulating multi-dimensional problems.

In this chapter, introductory material on the BTE governing rarefied gas flows and the standard DSMC particle simulation method is presented, followed by a review of previous variance-reduced methods. Subsequent chapters introduce the computational algorithms, validation and performance considerations, as well as some applications of these algorithms to problems of current interest. Finally, a conclusion is presented along with a discussion of open issues and suggested future research directions.

## 1.1 Particle description of rarefied gas transport

In order to provide the proper context for the computational algorithms developed in this thesis, in the present section we discuss the particle description of rarefied gas transport.

When the molecular mean free path ( $\lambda$ ) is no longer negligible compared to the system length scale ( $L$ ), the continuum-based description (Navier-Stokes and thermal diffusion equation) is no longer valid. This breakdown regime is typically referred to as the rarefied regime due to the original application to flows in the upper atmosphere, and is demarcated in terms of a Knudsen number, defined as the ratio of the mean free path to the system characteristic length scale ( $Kn = \lambda/L$ ). For many problems,  $L$  may be chosen as a relevant physical distance characterizing the simulation domain, but in other cases, in particular for early time transients,  $L$  must be chosen according to the local gradient(s) in the fundamental hydrodynamic variable(s) [14] (e.g.  $\frac{1}{L} = \frac{1}{T} \frac{dT}{dx}$ ).

In this thesis, we focus on a single monatomic gas species with only three (translational) degrees of freedom. The required particle description is the Boltzmann transport equation (BTE), a conservation equation for the velocity distribution function  $f(\mathbf{c}, \mathbf{x}, t)$ ; the latter is proportional to a probability distribution of particle velocities  $\mathbf{c}$  at a particle point in physical space  $\mathbf{x}$  and at a certain time  $t$ . For notational convenience, we will represent  $f(\mathbf{c}, \mathbf{x}, t)$  without its space and time dependence unless necessary for clarity. The BTE can be written in general form as follows:

$$\frac{\partial f(\mathbf{c})}{\partial t} + \mathbf{c} \cdot \frac{\partial f(\mathbf{c})}{\partial \mathbf{x}} + \mathbf{a} \cdot \frac{\partial f(\mathbf{c})}{\partial \mathbf{c}} = \mathcal{Q}[f, f](\mathbf{c}). \quad (1.1)$$

In the above,  $\mathbf{a}$  is a body force per unit mass. In the regimes of interest here (small departure from equilibrium), the gravitational body force is negligible, and thus it will be neglected; relaxing this assumption requires only small modifications to the algorithms presented in this thesis. The right hand side  $\mathcal{Q}[f, f](\mathbf{c})$  is the collision operator; the two most commonly used collision models were considered in the course of this research, and are discussed below.

### 1.1.1 The variable hard sphere collision model

The variable hard sphere (VHS) collision model was introduced by Bird [13] as an alternative to the hard sphere model due to its ability to more realistically capture the temperature dependence of transport coefficients on temperature.

In the VHS model, the dynamic viscosity is given by  $\mu = \mu_{\text{ref}}(T/T_{\text{ref}})^\omega$ , where  $\mu_{\text{ref}}$  is the dynamic viscosity at reference temperature  $T_{\text{ref}}$ , and  $\omega$  is the temperature exponent in the viscosity law. Typically  $\omega \approx 3/4$ , while the hard sphere result is recovered for  $\omega = 1/2$ . The collision operator for the VHS model can be written as

$$\mathcal{Q}[f, f](\mathbf{c}) = C_\beta \int_{\mathcal{S}^2} d^2\Omega \int_{\mathcal{R}^3} d^3\mathbf{c}_* \|\mathbf{c} - \mathbf{c}_*\|^\beta \cdot [f(\mathbf{c}')f(\mathbf{c}'_*) - f(\mathbf{c})f(\mathbf{c}_*)]. \quad (1.2)$$

In the above, primes denote post collision velocities  $\{\mathbf{c}', \mathbf{c}'_*\} = \frac{1}{2}(\mathbf{c} + \mathbf{c}_* \pm \|\mathbf{c} - \mathbf{c}_*\| \boldsymbol{\Omega})$ ; the solid angle  $\boldsymbol{\Omega}$  is integrated over the unit sphere  $\mathcal{S}^2$ . The relative velocity exponent  $\beta$  is related to the temperature coefficient of viscosity via  $\beta = 2(1 - \omega)$ . The constant prefactor is given by  $C_\beta = \frac{1}{4m} d_{\text{ref}}^2 c_{\text{r,ref}}^{1-\beta}$ , where  $m$  is the molecular mass,  $d_{\text{ref}}$  is the reference molecular diameter, and  $c_{\text{r,ref}} = 4\sqrt{RT_{\text{ref}}/\pi}$  is the mean relative molecular speed at reference temperature  $T_{\text{ref}}$ . Here,  $R = k_{\text{B}}/m$  denotes the gas constant, where  $k_{\text{B}}$  is the Boltzmann constant. In the VHS model, the mean free path has a temperature dependence given by  $\lambda^{-1} = \sqrt{2}\pi(\rho_0/m)d_{\text{ref}}^2(T_{\text{ref}}/T_0)^{\omega-1/2}$ , where  $\rho_0$  and  $T_0$  are the reference density and temperature. The hard sphere ( $\beta = 1$ ) and Maxwell molecule ( $\beta = 0$ ) collision models are well-known special cases.

### 1.1.2 The Bhatnagar-Gross-Krook collision model

The Bhatnagar-Gross-Krook (BGK) collision model [12]

$$\mathcal{Q}[f, f](\mathbf{c}) \approx -\frac{f(\mathbf{c}) - f^{\text{loc}}(\mathbf{c})}{\tau} \quad (1.3)$$

is a useful approximation to the collision dynamics of many systems which is reasonably accurate for many situations. This model is widely used, because it is far more

tractable mathematically, while still capturing much of the essential physics of more general collision models. Here,  $f^{\text{loc}}$  is a local Maxwell-Boltzmann (equilibrium) distribution based on the local hydrodynamic properties: mass density  $\rho$ , mean velocity  $\mathbf{u}$ , and temperature  $T$ .

$$f^{\text{loc}}(\mathbf{c}) = \frac{\rho}{\pi^{3/2} c_{\text{loc}}^3} \exp\left(-\frac{\|\mathbf{c} - \mathbf{u}\|^2}{c_{\text{loc}}^2}\right) \quad (1.4)$$

In the above,  $c_{\text{loc}} = \sqrt{2RT}$  is the most probable molecular velocity based on the local temperature.

In a dilute gas, the relaxation time  $\tau$  is inversely proportional to the local density, which can be represented as  $\tau = \rho_{\text{ref}}\tau_{\text{ref}}/\rho$ , where  $\tau_{\text{ref}}$  is the relaxation time at a reference state with density  $\rho_{\text{ref}}$ . The mean free path for this model is  $\lambda = \frac{2}{\sqrt{\pi}}c_0\tau_0$ , based on the relaxation time  $\tau_0$  and most probable velocity  $c_0 = \sqrt{2RT_0}$  of the global equilibrium state.

The key deficiency of the BGK model is that it predicts a Prandtl number  $Pr = c_p\mu/K$  of unity, in contrast to real gases for which  $Pr \approx \frac{2}{3}$ . Here,  $K$  is the thermal conductivity,  $\mu$  is the dynamic viscosity, and  $c_p$  is the specific heat at constant pressure. An incorrect Prandtl number is especially problematic for non-isothermal flows, because in these problems thermal and hydrodynamic fields are coupled. Because of this, the ellipsoidal statistical BGK (ES-BGK) model [16] has been introduced, which allows an arbitrary  $Pr$  to be prescribed.

### 1.1.3 Hydrodynamic properties

The connection between the molecular description ( $f$ ), and the desired hydrodynamic properties is made via moments (integrals weighted by polynomials in  $\mathbf{c}$ ) of the distribution function [59, 57]. These relationships are summarized below for the mass density, mean velocity, pressure tensor  $\mathbf{P}$  and heat flux  $\mathbf{q}$

$$\rho = \int_{\mathcal{R}^3} d^3\mathbf{c} f(\mathbf{c}) \quad (1.5)$$

$$\mathbf{u} = \frac{1}{\rho} \int_{\mathcal{R}^3} d^3\mathbf{c} \mathbf{c} f(\mathbf{c}) \quad (1.6)$$

$$\mathbf{P} = \int_{\mathcal{R}^3} d^3\mathbf{c} (\mathbf{c} - \mathbf{u})(\mathbf{c} - \mathbf{u}) f(\mathbf{c}) \quad (1.7)$$

$$T = \frac{1}{3\rho R} \int_{\mathcal{R}^3} d^3\mathbf{c} \|\mathbf{c} - \mathbf{u}\|^2 f(\mathbf{c}) \quad (1.8)$$

$$\mathbf{q} = \frac{1}{2} \int_{\mathcal{R}^3} d^3\mathbf{c} (\mathbf{c} - \mathbf{u}) \|\mathbf{c} - \mathbf{u}\|^2 f(\mathbf{c}). \quad (1.9)$$

The pressure tensor is related to the more familiar scalar pressure  $p$  and shear stress ( $\boldsymbol{\tau}$ ) variables typically encountered in fluid dynamics via

$$p = \frac{1}{3}(P_{xx} + P_{yy} + P_{zz}) = \rho RT \quad (1.10)$$

$$\boldsymbol{\tau} = p\mathbf{I} - \mathbf{P}. \quad (1.11)$$

In the above,  $\mathbf{I}$  is the  $(3 \times 3)$  identity tensor.

#### 1.1.4 Maxwell accommodation boundary interaction model

The Maxwell accommodation model is perhaps the most widely used boundary interaction model in which no net mass flux through the wall is allowed. It uses a single parameter (the accommodation coefficient,  $\alpha$ ) to represent the percentage of boundary collisions undergoing diffuse reflection.

According to the usual convention, we will define the unit surface normal  $\mathbf{n}$  to point into the gas, and use the definition  $c_n = \mathbf{c} \cdot \mathbf{n}$ . The boundary distribution is parameterized by the velocity  $\mathbf{u}_B$  and temperature  $T_B$  as shown below

$$\phi^B(\mathbf{c}) = \frac{1}{\pi^{3/2} c_B^3} \exp\left(-\frac{\|\mathbf{c} - \mathbf{u}_B\|^2}{c_B^2}\right), \quad c_B = \sqrt{2RT_B} \quad (1.12)$$

This permits the boundary condition to be represented as

$$f(\mathbf{c}) = \alpha \rho_B \phi^B(\mathbf{c}) + (1 - \alpha) f(\mathbf{c} - 2c_n \mathbf{n}), \quad c_n > 0, \quad (1.13)$$

where we have assumed that the walls are stationary in the normal direction:  $\mathbf{u}_B \cdot \mathbf{n} = 0$  (i.e. the boundary does not move in the direction normal to its plane). The “boundary density”  $\rho_B$  is determined by enforcing mass conservation, which is derived by setting the total mass flux at the boundary  $[\int_{\mathcal{R}^3} d^3\mathbf{c} c_n f(\mathbf{c})]$  to zero.

$$\rho_B = -\frac{\int_{c_n > 0} d^3\mathbf{c} c_n f(\mathbf{c})}{\int_{c_n < 0} d^3\mathbf{c} c_n \phi^B(\mathbf{c})} \quad (1.14)$$

## 1.2 The direct simulation Monte Carlo method

The direct simulation Monte Carlo (DSMC) method [3, 26], is a stochastic particle method developed by Bird [14], which has become the prevalent method for simulating general kinetic gas flows. While it was originally proposed based on physical considerations, it has subsequently been proven to provide solutions of the BTE in a stochastic sense [60]. DSMC has enjoyed widespread use due to its natural treatment of the advection operator, ability to capture traveling discontinuities in the velocity distribution function, and straightforward application in complicated geometries.

Formally, DSMC approximates the distribution by computational particles, with positions  $\mathbf{x}_i$  and velocities  $\mathbf{c}_i$

$$f(\mathbf{x}, \mathbf{c}) = mN_{\text{eff}} \sum_{i=1}^N \delta^3(\mathbf{x} - \mathbf{x}_i) \delta^3(\mathbf{c} - \mathbf{c}_i) \quad (1.15)$$

Here,  $N$  is the instantaneous number of computational particles in the simulation, and  $N_{\text{eff}}$  is the number of physical particles represented by each computational particle.

The DSMC method discretizes time by splitting the BTE into an advection step, which simulates the left hand side of Equation (1.1) for time step  $\Delta t$ , followed by a collision step which simulates the right hand side of Equation (1.1) for the same time step. During the advection step (assuming  $\mathbf{a} = \mathbf{0}$ ), the particles are simply moved along their trajectories, i.e.  $\mathbf{x}_i(t + \Delta t) = \mathbf{x}_i(t) + \mathbf{c}_i(t)\Delta t$ . When particles encounter a boundary, they are reflected back into the simulation domain by sampling their velocities from the fluxal boundary distribution:

$$2\sqrt{\pi} \frac{(\mathbf{c} - \mathbf{u}_B) \cdot \mathbf{n}}{c_B} \phi^B(\mathbf{c}), \quad (\mathbf{c} - \mathbf{u}_B) \cdot \mathbf{n} > 0. \quad (1.16)$$

### 1.2.1 Collision step

During the collision step, the state of the gas is advanced in time under the influence of the collision operator. The particles are sorted into spatial cells, and within each cell, pairs of particles are chosen to undergo collisions. For example, in the VHS model, the collision step satisfies

$$\left[ \frac{\partial f(\mathbf{c})}{\partial t} \right]_{\text{coll}} = C_\beta \int_{S^2} d^2\Omega \int_{\mathcal{R}^3} d^3\mathbf{c}_* \|\mathbf{c} - \mathbf{c}_*\|^\beta \cdot [f(\mathbf{c}')f(\mathbf{c}'_*) - f(\mathbf{c})f(\mathbf{c}_*)]. \quad (1.17)$$

According to the above expression, particle pairs are chosen with a probability proportional to  $\|\mathbf{c} - \mathbf{c}_*\|^\beta$ , and their original velocities  $\{\mathbf{c}, \mathbf{c}_*\}$  are replaced by post collision values  $\{\mathbf{c}', \mathbf{c}'_*\} = \frac{1}{2}(\mathbf{c} + \mathbf{c}_* \pm \|\mathbf{c} - \mathbf{c}_*\| \mathbf{\Omega})$ , where  $\mathbf{\Omega}$  is sampled uniformly from the unit sphere. A very desirable feature of this approach is that the mass, momentum, and energy conservation laws are satisfied for each collision, which eliminates random walks in the hydrodynamic variables [14].

The DSMC method has also been implemented based on the BGK approximation [43], where the collision step satisfies

$$\left[ \frac{\partial f(\mathbf{c})}{\partial t} \right]_{\text{coll}} = -\frac{f(\mathbf{c}) - f^{\text{loc}}(\mathbf{c})}{\tau}. \quad (1.18)$$

In this context, individual particles are sampled uniformly from each cell and the velocity is resampled from the local equilibrium distribution:  $f^{\text{loc}}(\mathbf{c})/\rho_{\text{loc}}$ . A key difference between this approach and standard collision operators (such as VHS) is that momentum and energy conservation are not enforced on a collision-pair basis. However, as shown by Macrossan [43], conservation laws can be introduced by shifting and scaling the particles in each cell at the end of each time step.

## 1.2.2 Hydrodynamic variables

Hydrodynamic variables are estimated on a cell-by-cell basis by summing the contributions contained within each cell. Specifically, performing a spatial average of Equations (1.5–1.9) and using Equation (1.15) yields

$$\rho = \frac{mN_{\text{eff}}}{\Delta V} N_C \quad (1.19)$$

$$\rho \mathbf{u} = \frac{mN_{\text{eff}}}{\Delta V} \sum_{i, \text{cell}} \mathbf{c}_i \quad (1.20)$$

$$\mathbf{P} + \rho \mathbf{u} \mathbf{u} = \frac{mN_{\text{eff}}}{\Delta V} \sum_{i, \text{cell}} \mathbf{c}_i \mathbf{c}_i \quad (1.21)$$

$$\rho (3RT + u^2) = \frac{mN_{\text{eff}}}{\Delta V} \sum_{i, \text{cell}} c_i^2 \quad (1.22)$$

$$2(\mathbf{q} + \mathbf{P} \cdot \mathbf{u}) + \rho (3RT + u^2) \mathbf{u} = \frac{mN_{\text{eff}}}{\Delta V} \sum_{i, \text{cell}} \mathbf{c}_i c_i^2. \quad (1.23)$$

In the above, the summations are performed over a single cell containing  $N_C$  particles with physical volume  $\Delta V$ .

## 1.2.3 Rate of convergence

DSMC is second-order accurate in cell size, and first-order convergence in the number of particles per cell [51]. Second-order time convergence behavior has been shown for symmetrized methods like Strang’s method [47, 51], which splits the advection step into two half steps (with time step  $\frac{1}{2}\Delta t$ ) on either side of the collision step.

## 1.2.4 Statistical error

Monte Carlo methods in general exhibit statistical noise which is inversely proportional to the square root of the number of *independent* samples (number of particles times number of ensembles) used in the approximation. While this is ordinarily considered to be a very poor rate of convergence, it is also independent of the number

of dimensions in the problem. Thus, as the number of dimensions in a problem increases, Monte Carlo methods tend to become more attractive in general. This is a fundamental reason why Monte Carlo based stochastic particle methods like DSMC have become the standard computational approach for simulating kinetic gas flows.

For DSMC, in the limit of small departure from equilibrium, the statistical error in the hydrodynamic variables has been characterized in detail [28]. For example, the relative statistical error in the cell-based velocity estimate is

$$\frac{\sigma_{u_x}}{U} = \frac{1}{\sqrt{N_{\text{ens}}N_C}} \frac{1}{\sqrt{\gamma Ma}}. \quad (1.24)$$

In the above,  $\sigma_{u_x}$  is the standard deviation of  $u_x$ ,  $N_C$  is the number of particles in the cell,  $N_{\text{ens}}$  is the number of statistically independent ensembles used to obtain the estimate,  $\gamma$  is the ratio of specific heats (e.g.  $\frac{5}{3}$  for a monoatomic gas), and  $Ma = U/c_s$  is the Mach number based on the characteristic velocity scale  $U$  and the speed of sound  $c_s = (\sqrt{\gamma RT})$  for a dilute gas).

Likewise, the relative statistical error in temperature for a problem with characteristic temperature difference  $\Delta T$  is

$$\frac{\sigma_T}{\Delta T} = \frac{1}{\sqrt{N_{\text{ens}}N_C}} \frac{\sqrt{k_B/c_V}}{\Delta T/T_0}, \quad (1.25)$$

and the remaining hydrodynamic fields show similar behavior [28]. In the above expression,  $c_V$  is the specific heat at constant volume on a molecular basis (e.g.  $c_V = \frac{3}{2}k_B$  for a monoatomic gas).

Both estimates (1.24, 1.25) show the expected dependence on the number of samples for a Monte Carlo method ( $\sim 1/\sqrt{N_{\text{ens}}N_C}$ ), and also a dependence on the departure from equilibrium conditions. Thus, for small Mach numbers or for small temperature perturbations, the statistical error in the hydrodynamic variables becomes very large. Low-variance methods, like the one discussed in this thesis, are capable of estimating the hydrodynamic properties with small relative statistical error levels that are also independent of the departure from equilibrium for near-equilibrium flows.

The resulting performance improvement can be enormous. As an initial demon-

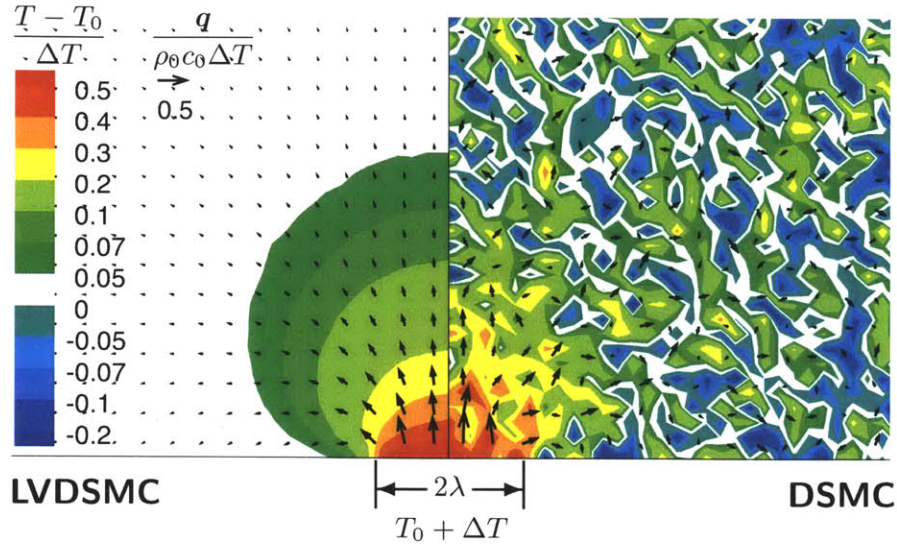


Figure 1-1: Temperature field (contours) and heat flux distribution (vectors) for the response of argon to an impulsively changed temperature on a  $2\lambda$  wide section of its boundary. The DSMC method and the method described in this thesis (denoted as LVDSMC) are compared at a time  $t = 10\lambda/c_0$ , showing dramatically improved efficiency for latter method. Both simulations required similar computational resources.

stration, consider the transient temperature response of an argon gas (VHS model) to a small perturbation in the temperature of its boundary, shown in Figure 1-1. Here, the lower boundary is diffusely reflecting and held at a temperature of  $T_0$ , except for the small region in the center of the simulation (denoted as having a width of  $2\lambda$ ), for which the temperature is impulsively raised to  $T_0 + \Delta T$ , where  $\Delta T = 0.01T_0$ . Shown are the temperature contours and corresponding heat flux vectors at a time  $t = 10\lambda/c_0$  obtained using the DSMC and the low-variance method which is the subject of this thesis. While both simulations required similar computational expense, the low-variance method shows dramatically reduced levels of statistical noise.

### 1.3 Previous work

Stochastic particle methods employing variance-reduction techniques have been developed only recently [9]; these methods have demonstrated considerable efficiency improvements over the DSMC method. These approaches are generally based on an

established variance reduction technique known as the method of control variates [7], in which low uncertainty evaluation of a certain moment is achieved by using information related to the value of a related (correlated) variable (the control). This idea has led to the development of two different types of variance-reduced particle methods: deviational particle methods, and weight-based particle methods.

### 1.3.1 Deviational particle methods

The key principle behind the deviational particle approach [9] is the utilization of a nearby equilibrium state  $f^{\text{eq}}$ , which, in situations close to equilibrium, closely approximates the actual distribution function  $f$ . Based on this equilibrium state, we define the deviational distribution as  $f^{\text{d}} = f - f^{\text{eq}}$ , which can be simulated with dramatically lower variance for the same number of computational particles. However, simulating  $f^{\text{d}}$  with particles leads to additional complications; the most notable is that because  $f^{\text{d}}$  can now take both positive and negative values, signed particles are required for its simulation.

The deviational particle approach was first discussed by Baker and Hadjiconstantinou [9], and led to the development of a variance-reduced particle method [10, 11, 8]. As extensively discussed in [10, 11, 8], methods based on the original Boltzmann collision integral suffer from stability limitations in the collision-dominated regime and require a particle cancelation scheme for stability. This is a severe limitation since it introduces an additional level of discretization (that is, a grid in velocity space) which is not present in DSMC.

A new class of deviational particle methods, known as the low-variance deviational simulation Monte Carlo (LVDSMC) method was introduced by Homolle and Hadjiconstantinou [32, 33, 31]; this method did not require particle cancelation for stability. This method was developed for the hard sphere collision operator, and achieved stability by exploiting the a particular form of the hard-sphere collision operator, originally obtained by Hilbert [17], in which the angular integration within the Boltzmann collision integral is performed analytically. Unlike the method of Baker and Hadjiconstantinou [10, 11] which used a fixed global equilibrium distribution,

the initial LVDSMC approach featured a spatially-variable equilibrium distribution, which is updated every time step in order to minimize the number of particles in the simulation. This approach is particularly advantageous for resolving the Navier-Stokes limit (system length scale much larger than mean free path), as the true distribution function naturally approaches local equilibrium conditions in this case. This is further discussed in Section 2.4.

Subsequent methods were introduced to treat the BGK collision model, which uses an approximation to the full Boltzmann collision integral. These include a relatively straightforward, but easily implementable version based on a fixed equilibrium distribution [29], and a highly-efficient linearized version [52], which is based on a spatially-variable local equilibrium distribution. In the second method [52], a new method for treating the advection part of the BTE based on the ratio-of-uniforms sampling technique was introduced resulting in an improvement in computational efficiency. These studies were also useful for highlighting a key tradeoff governing the choice between a fixed and local equilibrium distribution: namely, it was discovered that using a spatially-variable equilibrium distribution resulted in inferior efficiency when treating problems in multiple spatial dimensions. This is further discussed in Chapters 2. For this reason, much of the research performed by the author and colleagues has focused on the fixed equilibrium distribution in order to produce a more robust, and generally applicable method.

In recent work by Wagner [61], the LVDSMC method was put into a more precise theoretical framework, where a collision algorithm treating the variable hard sphere (VHS) collision model was also introduced. The VHS collision model is a more realistic collision model used for engineering models; it simulates gas models with viscosity which is proportional to the temperature raised to an arbitrary power  $0.5 \leq \omega \leq 1$  (in the hard sphere model, viscosity is proportional to the square root of temperature). The first successful implementation of a stochastic particle method employing the VHS collision algorithm was reported in reference [54], which, like the present approach, was implemented based on a fixed equilibrium distribution.

The resulting state-of-the-art VHS-LVDSMC method is described in this thesis,

and also in a recent publication [53]. One of the key improvements introduced is the introduction of a mass conservation procedure, which leads to a drastic reduction in the number of particles required in the simulation. This directly addressed a key limitation to previous deviational methods which were susceptible to random walks without a substantial number of particles (typically, requiring hundreds or thousands of particles per cell). This issue is particularly important when simulating steady state problems, as the required time for a simulation to reach steady state conditions can be substantial for a large number of particles.

### 1.3.2 Weight based methods

Variance-reduced stochastic particle methods employing particle weights have also appeared in the literature. The first such method was introduced by Chun and Koch for the linearized hard sphere collision model [22] where weights, as well as ghost particles, were used in order to simulate deviation from a fixed equilibrium distribution. However, this approach suffered from the same key deficiency as the original deviational particle method [10, 11]; namely, it required particle cancellation (and associated velocity discretization) for stability. Subsequently, a linearized BGK version [56] was introduced, which due to its similarity to the Hilbert form of the collision integral [29, 53], was stable without the need for a particle cancellation scheme.

A different approach was developed by Al Mohssen and Hadjiconstantinou [2, 1], in which variance-reduction procedures are run in parallel with an essentially unmodified DSMC simulation. This method is referred to as variance-reduced DSMC (VRDSMC). The key to this simulation approach is to construct, via particle weights, an equilibrium simulation that is correlated to the non-equilibrium simulation of interest, which is then exploited to obtain variance-reduced versions of the hydrodynamic properties. This approach was originally proposed by Öttinger [48] in the context of Brownian dynamics simulations. The VRDSMC approach is an important development because it allows variance-reduction to be performed by simple modifications to existing DSMC code bases, with almost no modification to the original DSMC

algorithm. Unfortunately, for the hard sphere collision operator, the DSMC and equilibrium simulations cannot maintain correlation indefinitely, leading to a loss of variance reduction [2, 1]. All evidence suggests that this phenomena is a manifestation of the same limitation, namely loss of stability, originally observed in deviational methods. This phenomena was also observed by Öttinger [48] in Brownian dynamics simulations. In the VRDSMC approach, correlation can be maintained by reconstructing the weights using kernel density estimation (KDE) [2, 1], which results in a tradeoff between stability and the bias error introduced by as a result of KDE. Resolving the continuum limit is particularly problematic, as it requires a large number of particles per cell for reasonable accuracy. In other words, the discovery of stable variance reduction methods using the Hilbert form is of great importance: instabilities seem to be a fundamental limitation of control variate variance reduction, yet appear to be ways of completely alleviating them without introducing numerical artifacts or approximations.

The VRDSMC methodology was also applied to the BGK collision operator [39, 37], resulting in a stable method without requiring a numerical procedure such as KDE, and thus avoiding the bias error issue. While this is a successful method for simulating rarefied gas flows, a more important aspect to this work (as well as References [52, 29]) is the application to other forms of particle transport. The BGK model is also used for phonon and electron transport, for example, where it is referred to as the relaxation time approximation [34, 42, 20, 21]. In particular, both the VRDSMC and deviational particle methods are currently being applied to phonon heat transfer simulations through nanostructured materials, which is an important research field for thermoelectric materials; the initial results [38, 49] are quite promising.

# Chapter 2

## Simulating Deviation from Equilibrium

In this chapter, we review and discuss two different strategies towards low-variance deviational Monte Carlo (LVDSMC). In the interest of simplicity, we limit the discussion to the BGK collision operator. In the first strategy, we simulate deviations from a fixed global equilibrium; in the second, we simulate deviations from a (cell-based) local equilibrium state. We show that, due to the algorithmic complexity associated with the spatially-variable equilibrium approach, methods using a global equilibrium as a control are more efficient for general multidimensional simulations, which is the justification for using this approach for the mass-conservative LVDSMC presented in later chapters. However, the local equilibrium approach in general provides more variance reduction; this effect becomes large in the  $Kn \rightarrow 0$  limit, which has important multiscale implications [55], especially if techniques are developed for dealing with the increased complexity and associated algorithmic complexity.

### 2.1 Decomposition of the velocity distribution

In the LVDSMC method, the key to achieving variance reduction is the decomposition of the velocity distribution

$$f = f^{\text{eq}} + f^{\text{d}}, \quad (2.1)$$

into an equilibrium state  $f^{\text{eq}}$ , and the remainder  $f^{\text{d}}$ , known as the deviational distribution, which is represented in terms of signed particles. The fundamental efficiency improvement for LVDSMC (and deviational particle methods in general) comes as a result of representing only the deviation from equilibrium using particles, thus allowing the majority of the velocity distribution to be represented by  $f^{\text{eq}}$  analytically and without statistical error.

There are two basic approaches for constructing decomposition (2.1), leading to simulation methods with contrasting features. In the first approach,  $f^{\text{eq}}$  is represented by a *global* equilibrium

$$f^0(\mathbf{c}) = \frac{\rho_0}{c_0^3 \pi^{3/2}} \exp\left(-\frac{\|\mathbf{c} - \mathbf{u}_0\|^2}{c_0^2}\right) \quad (2.2)$$

with fixed hydrodynamic properties  $\rho_0$ ,  $\mathbf{u}_0$ ,  $T_0$ , and  $c_0 = \sqrt{2RT_0}$ . The other approach involves choosing a spatially-variable equilibrium state

$$f^{\text{MB}}(\mathbf{c}) = \frac{\rho_{\text{MB}}}{c_{\text{MB}}^3 \pi^{3/2}} \exp\left(-\frac{\|\mathbf{c} - \mathbf{u}_{\text{MB}}\|^2}{c_{\text{MB}}^2}\right) \quad (2.3)$$

with cell-based properties  $\rho_{\text{MB}}(\mathbf{x}, \mathbf{c})$ ,  $\mathbf{u}_{\text{MB}}(\mathbf{x}, \mathbf{c})$ ,  $T_{\text{MB}}(\mathbf{x}, \mathbf{c})$ , and  $c_{\text{MB}}(\mathbf{x}, \mathbf{c}) = \sqrt{2RT_{\text{MB}}(\mathbf{x}, \mathbf{c})}$ , which are independently updated to track *local* equilibrium conditions. LVDSMC methods based on both approaches are discussed in the sections below, in the context of simulating the Boltzmann transport equation with the BGK collision model

$$\frac{\partial f(\mathbf{c})}{\partial t} + \mathbf{c} \cdot \frac{\partial f(\mathbf{c})}{\partial \mathbf{x}} = -\frac{f(\mathbf{c}) - f^{\text{loc}}(\mathbf{c})}{\tau}. \quad (2.4)$$

## 2.2 Deviation from a global equilibrium

Like the DSMC method, LVDSMC is discretized in time by splitting into advection and collision steps. Using  $f^{\text{eq}} = f^0$ , and decomposition (2.1), the left hand side of (2.4) becomes

$$\left[ \frac{\partial f^d(\mathbf{c})}{\partial t} + \mathbf{c} \cdot \frac{\partial f^d(\mathbf{c})}{\partial \mathbf{x}} \right]_{\text{adv}} = 0, \quad (2.5)$$

recovering the same advection equation, now in terms of the deviational distribution. As a consequence, deviational particles are updated during the advection step in the same manner as in DSMC.

The collision step is obtained from the right hand side of (2.4)

$$\left[ \frac{\partial f^d(\mathbf{c})}{\partial t} \right]_{\text{coll}} \Delta t = \underbrace{\frac{\Delta t}{\tau} [f^{\text{loc}}(\mathbf{c}) - f^0(\mathbf{c})]}_{\text{generation}} - \underbrace{\frac{\Delta t}{\tau} f^d(\mathbf{c})}_{\text{deletion}}, \quad (2.6)$$

which is represented by source and sink terms for deviational particles. These are implemented by generating new particles from distribution  $|f^{\text{loc}} - f^0|$ , and adding them to the simulation with sign  $\text{sgn}(f^{\text{loc}} - f^0)$ , and by deleting particles uniformly from the simulation.

This approach results in a simple method, first published in Reference [29]. A more sophisticated version, which has more efficient particle sampling techniques, better time convergence properties, as well as mass conservation, is presented in Chapters 3 and 5 of this thesis.

## 2.3 Deviation from a local equilibrium

Using a spatially-variable equilibrium results in a method which is considerably more efficient in the Navier-Stokes ( $Kn \rightarrow 0$ ) limit, where local equilibrium conditions prevail. Using  $f^{\text{eq}} = f^{\text{MB}}(\mathbf{x})$  in the left hand side of Equation (2.4) results in the following advection equation for deviational particles

$$\left[ \frac{\partial f^d(\mathbf{c})}{\partial t} + \mathbf{c} \cdot \frac{\partial f^d(\mathbf{c})}{\partial \mathbf{x}} \right]_{\text{adv}} = -\mathbf{c} \cdot \frac{\partial f^{\text{MB}}(\mathbf{c})}{\partial \mathbf{x}}. \quad (2.7)$$

This expression is identical to (2.5), except that it includes an inhomogeneous term. The procedures outlined for the global equilibrium form the homogenous part of the solution, while the inhomogeneous part is implemented by generating additional

particles at the cell interfaces [33, 52]. This additional generation term becomes expensive for a large number of cell interfaces, making it inappropriate for large multidimensional problems.

The collision step for this method

$$\left[ \frac{\partial f^d(\mathbf{c})}{\partial t} \right]_{\text{coll}} \Delta t = \underbrace{\frac{\Delta t}{\tau} [f^{\text{loc}}(\mathbf{c}) - f^{\text{MB}}(\mathbf{c})]}_{\text{generation}} - \underbrace{\Delta f^{\text{MB}} - \frac{\Delta t}{\tau} f^d(\mathbf{c})}_{\text{deletion}}, \quad (2.8)$$

has an additional term representing the shift in the equilibrium state  $\Delta f^{\text{MB}}$ , which can be chosen in order to reduce the number of particles generated from the source term.

In the limit of small departure from equilibrium (linearized conditions), it can be shown [52] that the particle generation term in (2.8) goes to zero when the equilibrium properties are updated according to

$$\Delta \rho_{\text{MB}} = \frac{\Delta t}{\tau} (\rho - \rho_{\text{MB}}) \quad (2.9)$$

$$\Delta \mathbf{u}_{\text{MB}} = \frac{\Delta t}{\tau} (\mathbf{u} - \mathbf{u}_{\text{MB}}) \quad (2.10)$$

$$\Delta T_{\text{MB}} = \frac{\Delta t}{\tau} (T - T_{\text{MB}}), \quad (2.11)$$

resulting in a very simple and computationally efficient collision step. In this case, the collision step is performed by shifting the  $f^{\text{MB}}$  properties for each cell toward the local equilibrium conditions for each cell, and by deleting particles from  $f^d$ . These procedures mimic the physics inherent in the BGK model, by relaxing the state of the gas toward the local equilibrium (for each cell).

As an example of the computational efficiency of the resulting method, Figure 2-1 shows a transient Couette flow solution at  $Kn = 0.2/\sqrt{\pi}$ ; this essentially noise-free solution required a CPU time of 70 seconds (on one core of a 3GHz Core2 Quad). For comparison, a DSMC calculation at Mach number  $Ma = 0.02$  (based on wall velocity  $U$ ) using the same CPU time is also shown (only the final time step is shown).

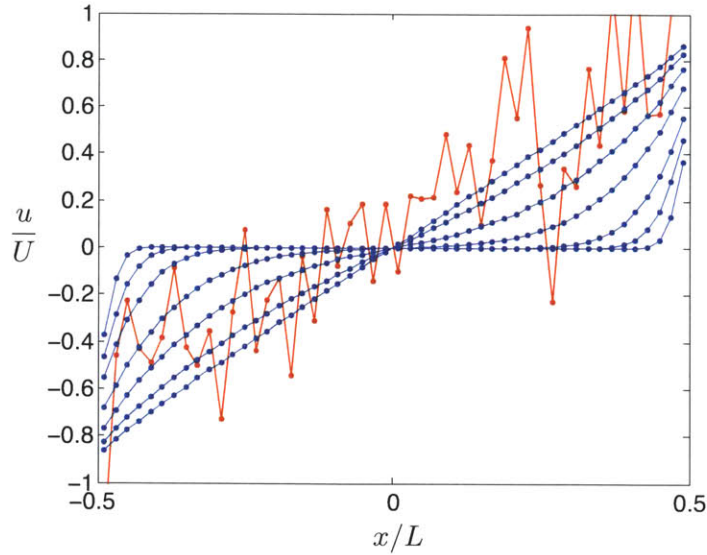


Figure 2-1: Transient Couette flow of a BGK gas at  $Kn = 0.2/\sqrt{\pi}$ . The LVDSMC result is based on deviation from a spatially-variable equilibrium; six snapshots are shown in blue. A DSMC solution corresponding to the final snapshot and using the same computational resources is shown in red.

## 2.4 Discussion

In the course of the research leading up to this thesis, several important tradeoffs were discovered between the two methods. For simulations in a single spatial dimension, a spatially-variable equilibrium is considerably more efficient in the Navier-Stokes ( $Kn \rightarrow 0$ ) limit [52]. This is demonstrated in Figure 2-2, where the total number of samples (the number of particles in simulation multiplied by the number of independent statistical ensembles) required to resolve the flow velocity in the cell adjacent to the wall for a steady Couette flow to a fixed level of statistical uncertainty is shown. This verifies that deviational simulations based on a local equilibrium require increasingly fewer samples (an indication of computational effort) than simulations based on a global equilibrium as the  $Kn \rightarrow 0$  limit is approached.

However, the added complication introduced by a spatially-variable equilibrium distribution makes the resulting method less efficient for multiple spatial dimensions, principally, because it requires particles to be generated at every cell interface

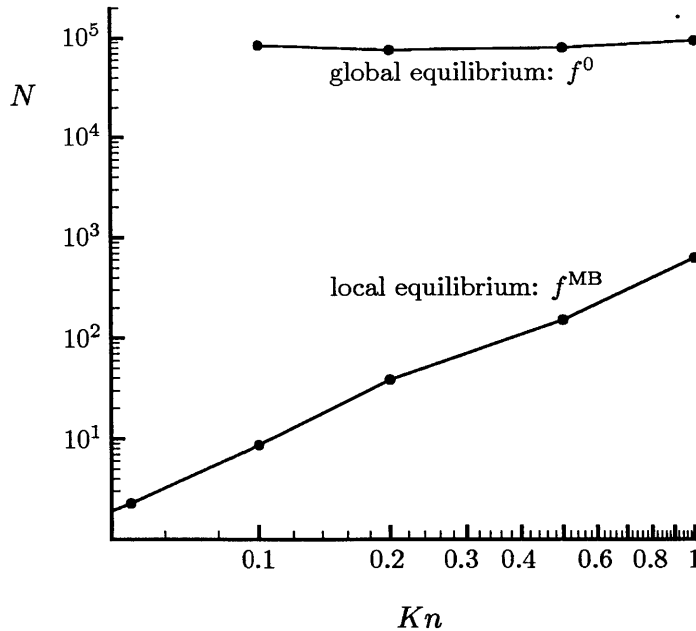


Figure 2-2: Comparison of the total number of samples required (in arbitrary units) to achieve a fixed level of statistical error in the cell near a wall for steady-state Couette flow simulations of a BGK gas, for deviational approaches based on global and local equilibrium distributions.

[32, 33, 31, 52]. Since the objective of this thesis was to develop a general and robust method capable of efficient, large-scale simulations in two- and three-dimensional geometries, we adopted the simpler fixed equilibrium approach. Moreover, the introduction of mass conservation into the simulation approach, which led to drastic efficiency improvements for steady state simulation of large problems, was much easier to implement for a fixed equilibrium. For this reason, a fixed equilibrium is adopted for the particle method discussed in Chapters 3–5, which forms the core of the thesis.

The local equilibrium approach is also used in this thesis, for extracting the second-order temperature jump coefficients for the hard sphere model in Section 7.2, which is a more specialized application requiring efficient resolution in lower Knudsen number ranges. For this reason, a specialized mass-conservative LVDSMC algorithm which treats a spatially-variable equilibrium was developed, which (unlike previous approaches) is not updated during the simulation. This approach is further discussed in Appendix B. In contrast, for extracting the second-order temperature jump co-

efficient for the BGK collision model, the simulation method based on a spatially-variable equilibrium was used, which is briefly described by Equations (2.7)–(2.11) and by Reference [52] in more detail. As the LVDSMC method is considerably more efficient for the BGK model (and thus large number of particles could be simulated), it was not necessary to implement a mass-conservative approach in this case.



# Chapter 3

## A Mass-conservative Low Variance Simulation Method

In this chapter, the basic theory behind the mass-conservative low variance deviational simulation Monte Carlo (LVDSMC) method is developed. This forms the framework for subsequent chapters focusing on the more detailed treatment of mass conservative forms of the variable hard sphere (VHS) and Bhatnagar-Gross-Krook (BGK) collision operators. The discussion in this chapter includes features common to LVDSMC methods such as treatment of the advection operator, evaluation of hydrodynamic properties, and inclusion of “effective body forces,” which allow the simulation of streamwise pressure and temperature gradients without placing computational cells in the streamwise direction. Specific algorithms for performing the collision step will be treated in Chapters 4 and 5.

### 3.1 Computational method

Like the DSMC method, the LVDSMC method simulates the BTE using computational particles. However, unlike DSMC particles, which represent clusters of physical particles, the LVDSMC uses particles to simulate the deviation from a suitably defined equilibrium state. Based on the discussion in Chapter 2, it was concluded that simulating deviation from fixed equilibrium state was the best approach for develop-

ing a general methodology for simulating multiple spatial dimensions. Thus, here the velocity distribution is represented as

$$f = f^0 + f^d, \quad (3.1)$$

where  $f^d$ , is represented in terms of particles using

$$f^d(\mathbf{c}) = mW_{\text{eff}} \sum_{i=1}^N s_i \delta^3(\mathbf{x} - \mathbf{x}_i) \delta^3(\mathbf{c} - \mathbf{c}_i), \quad (3.2)$$

which is analogous to (1.15) for DSMC. In the above expression,  $W_{\text{eff}}$  is a constant particle weight that relates the number of computational particles to simulation particles (like  $N_{\text{eff}}$  for DSMC). However, the relationship between  $W_{\text{eff}}$  and the number of particles in the simulation is not linear (as in DSMC); this is further discussed in Section 6. Additionally, since  $f^d$  (unlike  $f$ ) can take both positive and negative values, a particle sign is introduced:  $s_i \in \{\pm 1\}$ . This extra complexity resulting from the simulation of signed particles can be illustrated by considering a pair of particles which have opposite signs, but are otherwise identical: clearly, this particle pair would not have any influence the velocity distribution  $f$ . Thus, LVDSMC algorithms must be carefully designed, both in order to avoid producing extraneous particle pairs, but also to include a robust mechanism for removing these from the simulation when they do occur. In fact, this was the key drawback of the original deviational particle method [10, 11], which required a brute-force particle cancellation scheme for stability by preventing an otherwise unbounded increase in the number of particles in the simulation.

Like DSMC, the LVDSMC approach is simulated by splitting the time evolution into advection and collision steps, which are shown below in terms of the deviational distribution (3.1).

$$\left[ \frac{\partial f^d(\mathbf{c})}{\partial t} + \mathbf{c} \cdot \frac{\partial f^d(\mathbf{c})}{\partial \mathbf{x}} \right]_{\text{adv}} = 0 \quad (3.3)$$

$$\left[ \frac{\partial f^d(\mathbf{c})}{\partial t} \right]_{\text{coll}} = \mathcal{Q}[f, f](\mathbf{c}) \quad (3.4)$$

Each of these are described in the sections below.

Prior to introducing the specific simulation procedures for each step, we define the basic notation specifying the simulation domain. The entire simulation domain  $\mathcal{D}$  in physical space is partitioned into  $N_{\Delta V}$  spatial cells  $\mathcal{D}_j$ , each with spatial volume  $\Delta V_j$ ,  $j \in 1, 2, \dots, N_{\Delta V}$ ; the total volume is given by  $V = \sum_{j=1}^{N_{\Delta V}} \Delta V_j$ . The set of particles contained within cell  $j$  at the instantaneous state of the simulation is denoted by  $\mathcal{N}_j$ , where  $\bigcup_{j=1}^{N_{\Delta V}} \mathcal{N}_j = \{1, 2, \dots, N\}$ . Likewise, the boundary is discretized into  $N_{\Delta A}$  surface elements, each with area  $\Delta A_k$  and inward-facing surface normal  $\mathbf{n}_k$ , where  $k = \{1, 2, \dots, N_{\Delta A}\}$ .

## 3.2 Advection step

According to Equation (3.3), the advection of deviational particles is governed by the same equation as the advection of DSMC particles, and the particles are updated in the same manner as in DSMC: e.g.  $\mathbf{x}_i(t + \Delta t) = \mathbf{x}_i(t) + \mathbf{c}_i(t)\Delta t_{\text{adv}}$ , where  $\Delta t_{\text{adv}}$  is the advective time step.

Whenever particles encounter a boundary surface, the particles must be reflected according to the boundary condition (1.13, 1.14). Using (3.1), the deviational boundary condition for the  $k^{\text{th}}$  boundary surface (assuming  $\mathbf{u}_{\text{B},k} \cdot \mathbf{n}_k = 0$ ) becomes

$$f^{\text{d}}(\mathbf{c}) + f^0(\mathbf{c}) = \alpha_k \rho_{\text{B},k} \phi^{\text{B},k}(\mathbf{c}) + (1 - \alpha_k) [f^{\text{d}} + f^0](\mathbf{c} - 2(\mathbf{c} \cdot \mathbf{n}_k)\mathbf{n}_k), \quad \mathbf{c} \cdot \mathbf{n}_k > 0. \quad (3.5)$$

If the velocity of the global equilibrium state is also chosen to have a zero normal component for every boundary surface ( $\mathbf{u}_0 \cdot \mathbf{n}_k = 0$ ,  $k = 1, \dots, N_{\Delta A}$ ), then  $f^0(\mathbf{c} - 2(\mathbf{c} \cdot \mathbf{n}_k)\mathbf{n}_k) = f^0(\mathbf{c})$ . The ‘‘boundary density’’ is split into two terms:  $\rho_{\text{B},k} = \rho_{\text{B},k}^{\text{gen}} + \rho_{\text{B},k}^{\text{refl}}$  [52, 29], which gives the deviational boundary condition as

$$f^d(\mathbf{c}) = \alpha_k \rho_{B,k}^{\text{refl}} \phi^{B,k}(\mathbf{c}) + (1 - \alpha_k) f^d(\mathbf{c} - 2(\mathbf{c} \cdot \mathbf{n}_k) \mathbf{n}_k) + \alpha_k [\rho_{B,k}^{\text{gen}} \phi^{B,k} - f^0](\mathbf{c}), \quad \mathbf{c} \cdot \mathbf{n}_k > 0. \quad (3.6)$$

The three terms in Equation (3.6) correspond to three distinct procedures [52, 29]. The first term  $\alpha_k \rho_{B,k}^{\text{refl}} \phi^{B,k}(\mathbf{c})$  represents particles which strike the boundary and are diffusely reflected, while the second term,  $(1 - \alpha_k) f^d(\mathbf{c} - 2(\mathbf{c} \cdot \mathbf{n}_k) \mathbf{n}_k)$ , represents those which are specularly reflected. Both of these represent ordinary DSMC procedures, which are implemented by redrawing the velocity  $\mathbf{c}_i$  of the interacting particle  $i$  from the fluxal boundary distribution

$$2\sqrt{\pi} \frac{\mathbf{c} \cdot \mathbf{n}_k}{c_{B,k}} \phi^{B,k}(\mathbf{c}), \quad \mathbf{c} \cdot \mathbf{n}_k > 0 \quad (3.7)$$

with probability  $\alpha_k$ , and otherwise, the particle velocity is updated according to  $\mathbf{c}_i \rightarrow \mathbf{c}_i - 2(\mathbf{c}_{n_k})_i \mathbf{n}_k$ ; in either case the sign  $s_i$  is preserved and the particle is advected away from the boundary with the remaining time step. Sampling particles from the fluxal boundary distribution is a standard procedure, which is described briefly in Section A.1.3 of Appendix A.

For the LVDSMC method, additional consideration is made to the case of diffuse reflections, as it provides a mechanism for removing particles and thus providing stability in the free-molecular ( $Kn \gg 1$ ) limit, where the collision operator is not dominant. If two particles with opposite sign undergo a diffuse reflection with the same surface element in a time step, they are both removed from the simulation, since these particles have velocities drawn from the same distribution, which are reflected at the same time and from the same physical location within the ordinary discretization parameters ( $\Delta t_{\text{adv}}, \Delta x$ ). Therefore, if  $N_{\text{diff},k}^{\pm}$  positive and negative particles undergo diffuse reflections with surface element  $k$  in a given time step,  $\min\{N_{\text{diff},k}^+, N_{\text{diff},k}^-\}$  particles are removed from each population, chosen randomly and uniformly. This step has negligible effect for low Knudsen numbers, but leads to improved efficiency for  $Kn \gtrsim 1$  and is essential for stability in the  $Kn \rightarrow \infty$  limit.

It is important to note that the above procedure inherently conserves mass, which

in the LVDSMC context implies a conservation of the total sign ( $\sum_{i \in \text{refl},k} s_i$ ) of all reflecting particles. Mass conservation for the remaining boundary condition term  $\alpha_k [\rho_{\text{B},k}^{\text{gen}} \phi^{\text{B},k} - f^0](\mathbf{c})$  therefore involves forcing the total mass flux of this term to be zero, by requiring

$$\rho_{\text{B},k}^{\text{gen}} = - \frac{\int_{\mathbf{c} \cdot \mathbf{n}_k > 0} d^3 \mathbf{c} (\mathbf{c} \cdot \mathbf{n}_k) f^0(\mathbf{c})}{\int_{\mathbf{c} \cdot \mathbf{n}_k < 0} d^3 \mathbf{c} (\mathbf{c} \cdot \mathbf{n}_k) \phi^{\text{B},k}(\mathbf{c})}. \quad (3.8)$$

This expression is easily evaluated to yield

$$\rho_{\text{B},k}^{\text{gen}} = \rho_0 c_0 / c_{\text{B},k}. \quad (3.9)$$

### 3.2.1 Particle generation at the boundaries

With  $\rho_{\text{B},k}^{\text{gen}}$  evaluated, implementation of the final term in Equation (3.6) consists of sampling particles from the fluxal form of this distribution [11], which represents the flux of deviational particles being emitted from the boundary

$$\mathcal{F}_{\text{B},k} = \alpha_k (\mathbf{c} \cdot \mathbf{n}_k) [\rho_{\text{B},k}^{\text{gen}} \phi^{\text{B},k} - f^0](\mathbf{c}). \quad (3.10)$$

By multiplying the above expression by the boundary element area  $\Delta A_k$ , an infinitesimal volume in velocity space  $d^3 \mathbf{c}$ , and a time step for advection  $\Delta t_{\text{adv}}$ , the total rate of emission of deviational particles from a surface element with velocities in  $d^3 \mathbf{c}$  is given by

$$\mathcal{F}_{\text{B},k} \Delta A_k \Delta t_{\text{adv}} d^3 \mathbf{c} = \alpha_k (\mathbf{c} \cdot \mathbf{n}_k) [\rho_{\text{B},k}^{\text{gen}} \phi^{\text{B},k} - f^0](\mathbf{c}) \Delta A_k \Delta t_{\text{adv}} d^3 \mathbf{c}. \quad (3.11)$$

In previous implementations [11, 29], this distribution was sampled using an acceptance-rejection approach (see Section A.2 of the Appendix). We have developed a new approach [52, 54, 53] which uses the ratio-of-uniforms sampling method [62], which results in a higher computational efficiency, in particular for high  $Kn$  problems where it can be  $\sim 3$  times more efficient; this approach is described here.

While many of the key concepts of the ratio-of-uniforms method are introduced in this section, a fuller discussion is presented in Section A.3.

For convenience, a dimensionless velocity  $\boldsymbol{\xi} = (\mathbf{c} - \overline{\mathbf{u}_{B,k}})/\overline{c_{B,k}}$ , and average properties are introduced using the definitions

$$\overline{\rho_{B,k}} = \frac{1}{2} (\rho_{B,k} + \rho_0) \quad (3.12)$$

$$\overline{\mathbf{u}_{B,k}} = \frac{1}{2} (\mathbf{u}_{B,k} + \mathbf{u}_0) \quad (3.13)$$

$$\overline{c_{B,k}} = \frac{1}{2} (c_{B,k} + c_0). \quad (3.14)$$

Equation (3.11) now becomes

$$\mathcal{F}_{B,k} \Delta A_k \Delta t_{\text{adv}} d^3 \mathbf{c} = \alpha_k \overline{\rho_{B,k}} \overline{c_{B,k}} F^{\text{B},k}(\mathbf{c}) \Delta A_k \Delta t_{\text{adv}} d^3 \boldsymbol{\xi}, \quad (3.15)$$

where

$$F^{\text{B},k}(\mathbf{c}) = \frac{\overline{c_{B,k}}^2}{\rho_{B,k}} c_{n_k} [\rho_{B,k}^{\text{gen}} \phi^{\text{B},k} - f^0](\mathbf{c}). \quad (3.16)$$

Without loss of generality, we consider a surface with a surface normal  $\mathbf{n}_k$  in the  $+x$  direction; all the remaining boundary surfaces can be handled by the appropriate vector transformations. The key step in the ratio-of-uniforms method is the variable transformation [62, 52]:

$$\boldsymbol{\xi} = \boldsymbol{\eta}/\sqrt{H} \quad (3.17)$$

$$|F_{B,k}| = H^{5/2}. \quad (3.18)$$

For the ratio-of-uniforms method, the transformed variables are bounded by

$$0 \leq H \leq a^{\text{B},k} \quad (3.19)$$

$$0 \leq \eta_x \leq b_x^{\text{B},k} \quad (3.20)$$

$$-b_y^{\text{B},k} \leq \eta_y \leq b_y^{\text{B},k} \quad (3.21)$$

$$-b_z^{\text{B},k} \leq \eta_z \leq b_z^{\text{B},k}, \quad (3.22)$$

where the bounds can be evaluated from (see Reference [62] and Section A.3.1)

$$a^{\text{B},k} = \sup_{\xi \in \mathcal{R}^3} |F^{\text{B},k}(\mathbf{c})|^{2/5} \quad (3.23)$$

$$b_x^{\text{B},k} = \sup_{\xi \in \mathcal{R}^3} |\xi_x| |F^{\text{B},k}(\mathbf{c})|^{1/5} \quad (3.24)$$

$$b_y^{\text{B},k} = \sup_{\xi \in \mathcal{R}^3} |\xi_y| |F^{\text{B},k}(\mathbf{c})|^{1/5} \quad (3.25)$$

$$b_z^{\text{B},k} = \sup_{\xi \in \mathcal{R}^3} |\xi_z| |F^{\text{B},k}(\mathbf{c})|^{1/5}. \quad (3.26)$$

In order to determine estimates for these bounds the function  $F_{\text{B},k}$  is expanded to first order in terms of the density, velocity, and most probable velocity differences

$$\begin{aligned} F^{\text{B},k}(\mathbf{c}) &\approx F^{\text{B}0,k}(\mathbf{c}) \\ &= \xi_n \left[ \frac{\rho_{\text{B},k} - \rho_0}{\rho_{\text{B},k}} - 3 \frac{c_{\text{B},k} - c_0}{c_{\text{B},k}} + 2 \frac{\mathbf{u}_{\text{B},k} - \mathbf{u}_0}{c_{\text{B},k}} \cdot \boldsymbol{\xi} + 2 \frac{c_{\text{B},k} - c_0}{c_{\text{B},k}} \xi^2 \right] \frac{e^{-\xi^2}}{\pi^{3/2}}. \end{aligned} \quad (3.27)$$

In the limit of small departure from equilibrium, this expression is sufficient. It is straightforward to show (Section A.3.1) that the bounds for this function (which is a sum of simpler functions for which the bounds are known), can be obtained from the known bounds of the constituent functions. For example, if  $F = \sum_{i=1}^n p_i F^i$  and the bounds for sampling each  $F_i$  are known (i.e.  $a^i = \sup_{\xi \in \mathcal{R}^3} |F^i|^{2/5}$ ,  $b_x^i = \sup_{\xi \in \mathcal{R}^3} |\xi_x| |F^i|^{1/5}$ , etc.), then the following overall bounds hold for the transformed variables:

$$a = \left[ \sum_{i=1}^n |p_i| (a^i)^{5/2} \right]^{2/5} \quad (3.28)$$

$$b_x = \left[ \sum_{i=1}^n |p_i| (b_x^i)^5 \right]^{1/5} \quad (3.29)$$

$$b_y = \left[ \sum_{i=1}^n |p_i| (b_y^i)^5 \right]^{1/5} \quad (3.30)$$

$$b_z = \left[ \sum_{i=1}^n |p_i| (b_z^i)^5 \right]^{1/5} \quad (3.31)$$

Using the above approach, approximate bounds for sampling particles at the boundaries are

$$\begin{bmatrix} (a^{B0,k})^{5/2} \\ (b_x^{B0,k})^5 \\ (b_y^{B0,k})^5 \\ (b_z^{B0,k})^5 \end{bmatrix} = \mathbf{M}_B \cdot \begin{bmatrix} \left| \frac{\rho_{B,k} - \rho_0}{\rho_{B,k}} - 3 \frac{c_{B,k} - c_0}{c_{B,k}} \right| \\ 2 \frac{|u_{B,k,x} - u_{0,x}|}{c_{B,k}} \\ 2 \frac{|u_{B,k,y} - u_{0,y}|}{c_{B,k}} \\ 2 \frac{|u_{B,k,z} - u_{0,z}|}{c_{B,k}} \\ 2 \frac{|c_{B,k} - c_0|}{c_{B,k}} \end{bmatrix}, \quad (3.32)$$

where  $\mathbf{M}_B$  is a constant matrix given by

$$\mathbf{M}_B = \frac{1}{\pi^{3/2}} \begin{bmatrix} 1/\sqrt{2e} & 1/e & 1/(2e) & 1/(2e) & [3/(2e)]^{3/2} \\ (3/e)^3 & [7/(2e)]^{7/2} & 27e^{-7/2}/\sqrt{2} & 27e^{-7/2}/\sqrt{2} & (4/e)^4 \\ 5^{5/2}/(2e)^3 & (5/2)^{5/2}e^{-7/2} & 27e^{-7/2}/\sqrt{2} & 5^{5/2}/(2e)^{7/2} & 20^{5/2}/(27e^4) \\ 5^{5/2}/(2e)^3 & (5/2)^{5/2}e^{-7/2} & 5^{5/2}/(2e)^{7/2} & 27e^{-7/2}/\sqrt{2} & 20^{5/2}/(27e^4) \end{bmatrix}. \quad (3.33)$$

with elements taken from the tabulated values in Section A.3.1.

While these bounds are adequate for small departures from equilibrium, for more general conditions, they can be extended by introducing numerical factors ( $Y$ ),

$$a^{B,k} = Y_a^B a^{B0,k} \quad (3.34)$$

$$b_x^{B,k} = Y_{b,x}^B b_x^{B0,k} \quad (3.35)$$

$$b_y^{B,k} = Y_{b,y}^B b_y^{B0,k} \quad (3.36)$$

$$b_z^{B,k} = Y_{b,z}^B b_z^{B0,k} \quad (3.37)$$

which are dynamically updated during the simulation. The update step for the  $Y$  factors is discussed in this section, after the remainder of the boundary particle generation algorithm is discussed.

The appropriate number of trial particle generation steps for surface element  $k$  per time step  $N_{B,k}^{\text{trial}}$  can be obtained using the ratio-of-uniforms bounds (3.34–3.37) in order to find an upper bound on the absolute integral of Equation (3.15).

$$\begin{aligned} & \frac{1}{mW_{\text{eff}}} \int_{c_{n_k} > 0} d^3 \mathbf{c} \left| \left[ \frac{\partial f(\mathbf{c})}{\partial t} \right]_{B,k} \Delta A_k \Delta t_{\text{adv}} \right| \\ &= \frac{\alpha_k \overline{\rho_{B,k}} \overline{c_{B,k}} \Delta A_k \Delta t_{\text{adv}}}{mW_{\text{eff}}} \int_{\xi_n > 0} d^3 \xi |F^{B,k}(\mathbf{c})| \\ &= \frac{\alpha_k \overline{\rho_{B,k}} \overline{c_{B,k}} \Delta A_k \Delta t_{\text{adv}}}{mW_{\text{eff}}} \int_{\eta_n > 0} d^3 \eta \left| \frac{\partial (|F^{B,k}(\mathbf{c})|, \xi)}{\partial (H, \eta)} \right| H(\eta) \\ &< \frac{\alpha_k \overline{\rho_{B,k}} \overline{c_{B,k}} \Delta A_k \Delta t_{\text{adv}}}{mW_{\text{eff}}} \int_0^{b_x^{B,k}} d\eta_x \int_{-b_y^{B,k}}^{b_y^{B,k}} d\eta_y \int_{-b_z^{B,k}}^{b_z^{B,k}} d\eta_z \frac{5}{2} a^{B,k} \\ &= 10 \frac{\alpha_k \overline{\rho_{B,k}} \overline{c_{B,k}} \Delta A_k \Delta t_{\text{adv}}}{mW_{\text{eff}}} a^{B,k} b_x^{B,k} b_y^{B,k} b_z^{B,k} = N_{B,k}^{\text{trial}} \quad (3.38) \end{aligned}$$

In the expression above,  $mW_{\text{eff}}$  appears in order to relate the number of trial particles to the sampled distribution function (see Equation (3.2)). Note, that  $N_{B,k}^{\text{trial}}$  is generally not integer valued. Thus, for each time step and surface element,  $\lfloor N_{B,k}^{\text{trial}} \rfloor + 1$  trial steps are performed with probability  $N_{B,k}^{\text{trial}} - \lfloor N_{B,k}^{\text{trial}} \rfloor$ ; otherwise  $\lfloor N_{B,k}^{\text{trial}} \rfloor$  trial steps are performed. This convention is used for all particle generation steps (involving a non-integer number of trial samples) in the remainder of this thesis.

For each trial step, a sample  $(H, \boldsymbol{\eta})$  is generated (uniformly) utilizing bounds (3.34–3.37), and the corresponding trial particle velocity is determined via  $\mathbf{c} = \overline{\mathbf{u}_{B,k}} + \overline{c_{B,k}}\boldsymbol{\eta}/\sqrt{H}$ . The function  $F^{B,k}(\mathbf{c})$  is evaluated, and particles are accepted when  $H < |F^{B,k}(\mathbf{c})|^{2/5}$ . Accepted particles are advected a random fraction of the advective time step (performing ordinary DSMC reflection procedures for any subsequent boundary interactions) from a uniformly distributed random position on the boundary surface element  $\Delta A_k$  and added to the simulation with sign  $\text{sgn}[F^{B,k}(\mathbf{c})]$ .

The ratio-of-uniforms sampling bounds (3.34–3.37) are dynamically updated using the following procedure. At the start of the advection step, the bounds are fixed based on current values. During the advection step, when accepted particles are added with  $H$  or  $\boldsymbol{\eta}$  values very close to one of the sampling bounds, the appropriate  $Y$  factor is increased for the next advection step. For example, when a particle is accepted with  $H > (1 - \chi)a^{B,k}$ , the  $Y$  factor is updated to

$$Y_a^B = \max \left\{ \frac{H}{(1 - \chi)a^{B0,k}}, Y_a^B \right\}. \quad (3.39)$$

Here, the sampling margin  $\chi$  is a small, positive numerical parameter which controls the responsiveness of the dynamic update; typically  $\chi$  is chosen to be about one percent. The updated  $Y_a^B$  value does not take effect until subsequent time steps, when sampling bounds are reevaluated via Equation (3.34), and the identical procedure is followed for dynamically updating the remaining bounds. For typical simulations, the bounds are well-characterized by their approximate values (3.32, 3.33), and the numerical factors represent only small corrections.

### 3.2.2 Mass conservation enforcement

Unlike particle reflections, particle generation at the boundary only conserves mass on average. However, it is relatively straightforward to amend the above procedure to strictly conserve mass using a stratified sampling approach [7]. Because  $\int_{c_{n_k}} d^3\mathbf{c} F^{B,k}(\mathbf{c}) = 0$ , we know that on average the particle generation step must sample the same number of particles with positive and negative signs. The mass-

conserving approach involves first sampling  $\frac{1}{2}N_{B,k}^{\text{trial}}$  samples, keeping track of the number of positive and negative particles  $N_{B,k}^{\pm}$  which are accepted and added to the simulation. Finally, particle generation steps are repeated until precisely  $N_{B,k}^-$  positive and  $N_{B,k}^+$  negative particles are added to the simulation, rejecting all accepted particles of unneeded sign.

### 3.3 Effective body force

An important feature of the LVDSMC approach is that it enables simulations of small pressure and temperature gradients in ducts, without the added expense of simulating the streamwise direction. Although the effect of streamwise pressure gradients can be included into DSMC calculations by using the equivalence of a pressure gradient and gravitational body force, this approach cannot be used to introduce temperature gradients.

The technique of introducing streamwise gradients as an effective “body force” term was pioneered by Cercignani [19] as a mathematical formulation of pressure-driven flow in small capillaries; using this formulation, he was the first to theoretically verify the existence of a Knudsen minimum in the scaled flow rate as a function of non-dimensional channel height (see also Figure 6-5) originally observed experimentally by Knudsen [36]. This approach has been used to numerically solve pressure and temperature driven flows in standard configurations [40, 41, 24], and more recently, introduced into LVDSMC simulations [5, 52, 53].

Assuming flow in the  $z$  direction, the scaled pressure and temperature gradients are defined as:

$$\kappa_p = -\frac{1}{P} \frac{dP}{dz} \quad (3.40)$$

$$\kappa_T = \frac{1}{T} \frac{dT}{dz}. \quad (3.41)$$

As in Cercignani’s formulation, pressure and temperature gradient effects can be

included into LVDSMC simulations by assuming that the streamwise dependence is carried by the underlying equilibrium state. This leads to an additional term

$$\left[ \frac{\partial f^d(\mathbf{c})}{\partial t} \right]_{\text{body}} = - \left[ c_z \frac{\partial f^{\text{eq}}(\mathbf{c})}{\partial z} \right]_{\text{body}} = c_z \left[ \kappa_P + \left( \frac{5}{2} - \frac{\|\mathbf{c} - \mathbf{u}_0\|^2}{c_0^2} \right) \kappa_T \right] f^0(\mathbf{c}), \quad (3.42)$$

in the advection operator (see Equation (3.3)), which is introduced into the simulation via a separate step.

Multiplying the above expression by the total simulation volume  $V$ , time step  $\Delta t_{\text{body}}$ , and differential element in velocity space  $d^3\mathbf{c}$  gives the total change in deviational particles due to this body force for velocities within  $d^3\mathbf{c}$  per time step.

$$\left[ \frac{\partial f^d(\mathbf{c})}{\partial t} \right]_{\text{body}} V \Delta t_{\text{body}} d^3\mathbf{c} = c_z \left[ \kappa_P + \left( \frac{5}{2} - \frac{\|\mathbf{c} - \mathbf{u}_0\|^2}{c_0^2} \right) \kappa_T \right] f^0(\mathbf{c}) V \Delta t_{\text{body}} d^3\mathbf{c} \quad (3.43)$$

As with the boundary generation term, a dimensionless velocity  $\boldsymbol{\xi} = \mathbf{c}/c_0$  and dimensionless sampling function  $F^F$  are introduced. For simplicity,  $\mathbf{u}_0 = \mathbf{0}$  has been assumed, and we have normalized the above quantities around the equilibrium state properties (rather than average properties, as used in the advection step), since the effective “body force” approach is only appropriate for small departures from equilibrium. With these assumptions,

$$\left[ \frac{\partial f^d(\mathbf{c})}{\partial t} \right]_{\text{body}} V \Delta t_{\text{body}} d^3\mathbf{c} = \frac{\rho_0 c_0}{L} F^F(\mathbf{c}) V \Delta t_{\text{body}} d^3\boldsymbol{\xi} \quad (3.44)$$

$$F^F(\mathbf{c}) = \frac{c_0^2 L}{\rho_0} c_z \left[ \kappa_P + \left( \frac{5}{2} - \xi^2 \right) \kappa_T \right] f^0(\mathbf{c}). \quad (3.45)$$

Here, a physical length scale  $L$  was introduced in order to make distribution  $F^F$  dimensionless.

Similar to the advection routine (Section 3.2), the ratio-of-uniforms variable transformation is applied:  $|F^F| = H^{5/2}$  and  $\boldsymbol{\xi} = \boldsymbol{\eta}/\sqrt{H}$ , where, the bounds are defined

by

$$0 \leq H \leq a^F \quad (3.46)$$

$$-b_x^F \leq \eta_x \leq b_x^F \quad (3.47)$$

$$-b_y^F \leq \eta_y \leq b_y^F \quad (3.48)$$

$$-b_z^F \leq \eta_z \leq b_z^F. \quad (3.49)$$

Using the results from Section A.3.1, the proper sampling bounds are determined to be

$$\begin{bmatrix} (a^F)^{5/2} \\ (b_x^F)^5 \\ (b_y^F)^5 \\ (b_z^F)^5 \end{bmatrix} = \frac{1}{\pi^{3/2}} \begin{bmatrix} 1/\sqrt{2e} & [3/(2e)]^{3/2} \\ 5^{5/2}/(2e)^3 & 20^{5/2}/(27e^4) \\ 5^{5/2}/(2e)^3 & 20^{5/2}/(27e^4) \\ (3/e)^3 & (4/e)^4 \end{bmatrix} \cdot \begin{bmatrix} |\kappa_P + \frac{5}{2}\kappa_T| \\ |\kappa_T| \end{bmatrix} L. \quad (3.50)$$

As before, the number of trial steps is determined from the ratio-of-uniforms bounds (3.46–3.49) via an upper bound on the absolute integral of Equation (3.44).

$$\begin{aligned} & \frac{1}{mW_{\text{eff}}} \int_{\mathcal{R}^3} d^3\mathbf{c} \left| \left[ \frac{\partial f(\mathbf{c})}{\partial t} \right]_{\text{B},k} V \Delta t_{\text{body}} \right| \\ &= \frac{\rho_0 c_0 V \Delta t_{\text{body}}}{mW_{\text{eff}} L} \int_{\mathcal{R}^3} d^3\xi |F^F(\mathbf{c})| \\ &= \frac{\rho_0 c_0 V \Delta t_{\text{body}}}{mW_{\text{eff}} L} \int_{\mathcal{R}^3} d^3\eta \left| \frac{\partial (|F^B(\mathbf{c})|, \xi)}{\partial (H, \boldsymbol{\eta})} \right| H(\boldsymbol{\eta}) \\ &< \frac{\rho_0 c_0 V \Delta t_{\text{body}}}{mW_{\text{eff}} L} \int_{-b_x^F}^{b_x^F} d\eta_x \int_{-b_y^F}^{b_y^F} d\eta_y \int_{-b_z^F}^{b_z^F} d\eta_z \frac{5}{2} a^F \\ &= 20 \frac{\rho_0 c_0 V \Delta t_{\text{body}}}{mW_{\text{eff}} L} a^F b_x^F b_y^F b_z^F = N_{\text{F}}^{\text{trial}} \end{aligned} \quad (3.51)$$

A sample  $(H, \boldsymbol{\eta})$  is generated (uniformly) utilizing bounds (3.46–3.49) for each trial step. Using  $\mathbf{c} = c_0 \boldsymbol{\eta} / \sqrt{H}$ ,  $F^F$  is evaluated from Eqn. (3.44), and the trial particle generation is accepted if  $H < |F^F(\mathbf{c})|^{2/5}$ . Accepted particles are added to the

simulation with sign  $\text{sgn}[F^{\mathbb{F}}(\mathbf{c})]$  and with a position  $\mathbf{x}$  sampled uniformly from  $\mathcal{D}$ .

### 3.3.1 Mass conservation

Mass conservation is enforced by the stratified sampling approach used for the boundary particle generation routine (see Section 3.2). Initially,  $N_{\mathbb{F}}^{\text{trial}}/2$  trial generation steps are performed, which adds  $N_{\mathbb{F}}^{\pm}$  positive and negative particles to the simulation, and additional particle generation steps are performed to produce  $N_{\mathbb{F}}^{\mathbb{F}}$  additional positive and negative particles.

## 3.4 Property evaluation

Hydrodynamic properties are evaluated by simple extensions [31, 53] to the rules developed for evaluating cell-based properties for DSMC properties (1.19–1.23), where moments of the deviational particles now correspond to the difference between the hydrodynamic properties and their equilibrium values. Specifically

$$\rho_j = \rho_0 + \frac{mW}{\Delta V_j} \sum_{i \in \mathcal{N}_j} s_i \quad (3.52)$$

$$\rho_j \mathbf{u}_j = \rho_0 \mathbf{u}_0 + \frac{mW}{\Delta V_j} \sum_{i \in \mathcal{N}_j} s_i \mathbf{c}_i \quad (3.53)$$

$$\mathbf{P}_j + \rho_j \mathbf{u}_j \mathbf{u}_j = \mathbf{P}_0 + \rho_0 \mathbf{u}_0 \mathbf{u}_0 + \frac{mW}{\Delta V_j} \sum_{i \in \mathcal{N}_j} s_i \mathbf{c}_i \mathbf{c}_i \quad (3.54)$$

$$\rho_j (3RT_j + u_j^2) = \rho_0 (3RT_0 + u_0^2) + \frac{mW}{\Delta V_j} \sum_{i \in \mathcal{N}_j} s_i c_i^2 \quad (3.55)$$

$$2(\mathbf{q}_j + \mathbf{P}_j \cdot \mathbf{u}_j) + \rho_j (3RT_j + u_j^2) \mathbf{u}_j = 2\mathbf{P}_0 \cdot \mathbf{u}_0 + \rho_0 (3RT_0 + u_0^2) \mathbf{u}_0 + \frac{mW}{\Delta V_j} \sum_{i \in \mathcal{N}_j} s_i \mathbf{c}_i c_i^2. \quad (3.56)$$

In Equation (3.54) above, the equilibrium pressure tensor is given by  $\mathbf{P}_0 = \rho_0 RT_0 \mathbf{I} = p_0 \mathbf{I}$  where  $\mathbf{I}$  is the identity tensor.

## 3.5 Time integration

The advection and collision step has no intrinsic time step error, while the collision routine may or may not, depending on the implementation. However, as in the DSMC method, time step error is introduced by the the time splitting procedure. Here, we employ Strang’s splitting method [47], which has been demonstrated to offer second-order time convergence in the case of the DSMC method (see Section 1.2). A variant of this algorithm has been implemented in a previous LVDSMC method [52], also demonstrating second-order time convergence for the computationally simpler BGK collision operator. Further convergence studies are needed, but are left to future research efforts.

Strang’s method for LVDSMC for an overall time step  $\Delta t$  consists of the following algorithm:

**Algorithm 3.1.** Strang’s method for LVDSMC

1. Half advection ( $\Delta t_{\text{adv}} = \frac{1}{2}\Delta t$ )
2. Half body force ( $\Delta t_{\text{body}} = \frac{1}{2}\Delta t$ )
3. Full collision ( $\Delta t_{\text{coll}} = \Delta t$ )
4. Half body force ( $\Delta t_{\text{body}} = \frac{1}{2}\Delta t$ )
5. Half advection ( $\Delta t_{\text{adv}} = \frac{1}{2}\Delta t$ )
6. Sample properties

where collision routines with time step  $\Delta t_{\text{coll}}$  will be described in the following chapters.



# Chapter 4

## Simulation of the Variable Hard Sphere Gas

The collision algorithm for the more general of the two collision models discussed in this thesis is based on a method originally proposed by Wagner [61]. A key feature of this algorithm is the absence of intrinsic time step error, unlike previous LVDSMC methods [33, 52, 29]; this is achieved by simulating the collision process as a sequence of Markov particle creation and deletion events.

In this thesis, we present a LVDSMC particle method [54, 53] based on Wagner's VHS collision algorithm, which has been extended to feature mass conservation [53]. This mass-conservative method is capable of accurately simulating typical gas transport problems in the transition regime ( $0.1 \lesssim Kn \lesssim 10$ ) with approximately ten particles per cell, which is similar to the number of particles required for DSMC simulations [14].

### 4.1 Alternative form of the VHS collision operator

In keeping with the general framework presented in Chapter 3, we use Equation (1.2) in the collision step (3.4) to split the collision operator into linear  $\mathcal{L}[f^d]$  and nonlinear  $\mathcal{Q}[f^d, f^d]$  parts.

$$\begin{aligned}
\left[ \frac{\partial f^d(\mathbf{c})}{\partial t} \right]_{\text{coll}} &= \mathcal{Q}[f^0 + f^d, f^0 + f^d](\mathbf{c}) \\
&= C_\beta \int_{S^2} d^2\Omega \int_{\mathcal{R}^3} d^3\mathbf{c}_* \|\mathbf{c} - \mathbf{c}_*\|^\beta \\
&\quad \cdot [f^0(\mathbf{c}')f^d(\mathbf{c}'_*) + f^0(\mathbf{c}'_*)f^d(\mathbf{c}') - f^0(\mathbf{c})f^d(\mathbf{c}_*) - f^0(\mathbf{c}_*)f^d(\mathbf{c})] \\
&\quad + C_\beta \int_{S^2} d^2\Omega \int_{\mathcal{R}^3} d^3\mathbf{c}_* \|\mathbf{c} - \mathbf{c}_*\|^\beta \cdot [f^d(\mathbf{c}')f^d(\mathbf{c}'_*) - f^d(\mathbf{c})f^d(\mathbf{c}_*)] \\
&= \mathcal{L}[f^d](\mathbf{c}) + \mathcal{Q}[f^d, f^d](\mathbf{c}) \tag{4.1}
\end{aligned}$$

For small departures from equilibrium, the nonlinear part has a negligible effect, and so for the majority of applications of interest here (low speed flows, heat transfer due to small temperature perturbations, etc.), the linear part of the collision operator is dominant. In other words,

$$\left[ \frac{\partial f^d(\mathbf{c})}{\partial t} \right]_{\text{coll}} = \mathcal{L}[f^d](\mathbf{c}) \tag{4.2}$$

$$\begin{aligned}
\mathcal{L}[f^d](\mathbf{c}) &= C_\beta \int_{S^2} d^2\Omega \int_{\mathcal{R}^3} d^3\mathbf{c}_* \|\mathbf{c} - \mathbf{c}_*\|^\beta \\
&\quad \cdot [2f^0(\mathbf{c}')f^d(\mathbf{c}'_*) - f^0(\mathbf{c})f^d(\mathbf{c}_*) - f^0(\mathbf{c}_*)f^d(\mathbf{c})]. \tag{4.3}
\end{aligned}$$

In fact, it is straightforward to include the nonlinear effects as a separate collision process; this is further discussed in [10, 31]. However, this is of limited utility, since in the non-linear regime signals are not small and DSMC approaches can be used. However, we will note here, that this approach was implemented in a preliminary study [54], which showed agreement with the DSMC method for moderate departures from equilibrium (for large departure from equilibrium, this term causes the production of a large number of particles which interferes with the stabilizing effect of the linear part). In the original hard sphere LVDSMC method [31], which used a spatially-variable equilibrium distribution, stable accurate results were obtained for  $Ma \lesssim 1$ ; however for  $Ma \sim 1$ , DSMC is already more efficient than LVDSMC.

For hard sphere collisions, a special version of the collision operator was derived by Hilbert [17], in which the angular integration (see Equation (1.2) with  $\beta = 1$ ) was performed analytically, yielding a convenient representation in terms of the following kernel functions  $K_1^{(1)}$ ,  $K_1^{(2)}$  and collision rate function  $\nu_1$

$$\mathcal{L}[f^d](\mathbf{c}) = \int_{\mathcal{R}^3} d^3\mathbf{c}_* \left[ 2K_1^{(1)} - K_1^{(2)} \right] (\mathbf{c}, \mathbf{c}_*) f^d(\mathbf{c}_*) - \nu_1(\mathbf{c}) f^d(\mathbf{c}) \quad (4.4)$$

$$K_1^{(1)}(\mathbf{c}, \mathbf{c}_*) = \frac{4C_1\rho_0}{\sqrt{\pi}c_0\|\mathbf{c} - \mathbf{c}_*\|} \exp\left(-\frac{[(\mathbf{c} - \mathbf{u}_0) \cdot (\mathbf{c} - \mathbf{c}_*)]^2}{c_0^2\|\mathbf{c} - \mathbf{c}_*\|^2}\right) \quad (4.5)$$

$$K_1^{(2)}(\mathbf{c}, \mathbf{c}_*) = 4\pi C_1\|\mathbf{c} - \mathbf{c}_*\| f^0(\mathbf{c}) \quad (4.6)$$

$$\nu_1(\mathbf{c}) = 4\pi C_1\rho_0c_0\psi(\xi). \quad (4.7)$$

Here,  $\boldsymbol{\xi} = (\mathbf{c} - \mathbf{u}_0)/c_0$ , while  $\xi = \|\boldsymbol{\xi}\|$ , and  $\psi(\xi)$  is a pure numerical function given by

$$\psi(\xi) = \frac{e^{-\xi^2}}{\sqrt{\pi}} + \left( \xi + \frac{1}{2\xi} \right) \text{erf}(\xi). \quad (4.8)$$

This served as the mathematical framework for the original hard sphere LVDSMC method [32, 33, 31], in which the  $-\nu_1(\mathbf{c})f^d(\mathbf{c})$  term provides a mechanism for removing particles, while sampling particles directly from the  $\left[ 2K_1^{(1)} - K_1^{(2)} \right]$  term (rather than from each term separately) prevents the generation of extraneous particles; both of these features counter unbounded increases in the number of particles in the simulation, leading to a stable collision algorithm.

The VHS operator can be expressed in the same form as Equation (4.4); however, an analytical form for the first kernel function  $K_\beta^{(1)}$  is not available [16, 17, 18], but is instead expressed as a integration over the collision angle  $\Omega$ . More recently, Wagner [61] has expressed this in alternative form, which is expressed as an integral over an auxiliary velocity  $\boldsymbol{\zeta}$ .

$$\mathcal{L}[f^d](\mathbf{c}) = \int_{\mathcal{R}^3} d^3\mathbf{c}_* \left[ 2K_\beta^{(1)} - K_\beta^{(2)} \right] (\mathbf{c}, \mathbf{c}_*) f^d(\mathbf{c}_*) - \nu_\beta(\mathbf{c}) f^d(\mathbf{c}) \quad (4.9)$$

$$K_{\beta}^{(1)}(\mathbf{c}, \mathbf{c}_{*}) = \frac{4C_{\beta}}{\|\mathbf{c} - \mathbf{c}_{*}\|} \int_{\Gamma_{\perp}(\mathbf{c} - \mathbf{c}_{*})} d^3\zeta \frac{f^0(\mathbf{c} + \zeta)}{\|\mathbf{c} - \mathbf{c}_{*} - \zeta\|^{1-\beta}} \quad (4.10)$$

$$K_{\beta}^{(2)}(\mathbf{c}, \mathbf{c}_{*}) = 4\pi C_{\beta} \|\mathbf{c} - \mathbf{c}_{*}\|^{\beta} f^0(\mathbf{c}) \quad (4.11)$$

$$\nu_{\beta}(\mathbf{c}) = 4\pi C_{\beta} \int_{\mathcal{R}^3} d^3\mathbf{c}_{*} \|\mathbf{c} - \mathbf{c}_{*}\|^{\beta} f^0(\mathbf{c}_{*}) \quad (4.12)$$

In the above,  $\Gamma_{\perp}(\mathbf{c})$  is the plane perpendicular to  $\mathbf{c}$  passing through the origin. An additional relation, which is important for the derivations to follow, relates integrals of the kernel functions to the collision rate function.

$$\nu_{\beta}(\mathbf{c}_{*}) = \int_{\mathcal{R}^3} d^3\mathbf{c} K_{\beta}^{(1)}(\mathbf{c}, \mathbf{c}_{*}) = \int_{\mathcal{R}^3} d^3\mathbf{c} K_{\beta}^{(2)}(\mathbf{c}, \mathbf{c}_{*}) \quad (4.13)$$

The collision rate function (4.12) is also not analytically available. However, a tight upper bound can be formed by using the following inequality, which is valid for  $0 \leq \beta \leq 1$ .

$$\left( \frac{\|\mathbf{c} - \mathbf{c}_{*}\|}{c_0} \right)^{\beta} \leq \beta \frac{\|\mathbf{c} - \mathbf{c}_{*}\|}{c_0} + (1 - \beta), \quad \forall \mathbf{c}, \mathbf{c}_{*} \in \mathcal{R}^3 \quad (4.14)$$

Using the above inequality to replace  $\|\mathbf{c} - \mathbf{c}_{*}\|^{\beta}$  in Equation (4.12), the desired bound on the collision rate function is obtained

$$\begin{aligned} \nu_{\beta}(\mathbf{c}) &\leq \nu_{\beta, \max}(\mathbf{c}) = 4\pi C_{\beta} c_0^{\beta} \int_{\mathcal{R}^3} d^3\mathbf{c}_{*} \left[ \beta \frac{\|\mathbf{c} - \mathbf{c}_{*}\|}{c_0} + (1 - \beta) \right] f^0(\mathbf{c}_{*}) \\ &= 4\pi C_{\beta} \rho_0 c_0^{\beta} [\beta \psi(\xi) + (1 - \beta)], \quad \forall \mathbf{c} \in \mathcal{R}^3. \end{aligned} \quad (4.15)$$

The integral above can be obtained from a relation derived in Reference [61], or by comparison with the hard sphere expression (4.7). Equality for Equations (4.14, 4.15) is recovered for both the hard-sphere ( $\beta = 1$ ) and Maxwell-molecule ( $\beta = 0$ ) limits. In the same manner, bounds on the collision kernels are obtained via Equations (4.10), (4.11), and (4.14).

$$K_{\beta}^{(1)}(\mathbf{c}, \mathbf{c}_{\star}) \leq K_{\beta, \max}^{(1)}(\mathbf{c}, \mathbf{c}_{\star}) = \frac{4C_{\beta}c_0^{\beta}}{\|\mathbf{c} - \mathbf{c}_{\star}\|} \int_{\Gamma_{\perp}(\mathbf{c} - \mathbf{c}_{\star})} d^3\zeta \left[ \frac{\beta}{c_0} + \frac{1 - \beta}{\|\mathbf{c} - \mathbf{c}_{\star} - \zeta\|} \right] f^0(\mathbf{c} + \zeta) \quad (4.16)$$

$$K_{\beta}^{(2)}(\mathbf{c}, \mathbf{c}_{\star}) \leq K_{\beta, \max}^{(2)}(\mathbf{c}, \mathbf{c}_{\star}) = 4\pi C_{\beta}c_0^{\beta} \left[ \frac{\|\mathbf{c} - \mathbf{c}_{\star}\|}{c_0} + (1 - \beta) \right] f^0(\mathbf{c}) \quad (4.17)$$

## 4.2 Stochastic collision time steps

In the particle generation routine for boundaries described in Section 3.2, the emission of a deviational particles from the boundary has no effect on the generation of subsequent particles. For this reason, the total number of trial generation steps could be determined a priori and processed without any need to continuously update the state of the simulation in the intermediate steps. However, the collision processes governed by Equation (4.9) depends on the instantaneous state of the particles through  $f^d$ . Thus, in order to simulate the collision process without introducing an additional time step error, the instantaneous state of the simulation must be taken into account between particle collision events.

The approach used here, and introduced in Reference [61], models the collision process as Markov creation and deletion events, each advancing the state of the simulation in time by an exponentially distributed stochastic time step with parameter  $\Lambda$ , such that

$$p_{\Lambda}(\delta t) = \Lambda e^{-\Lambda \delta t}, \quad \delta t \in (0, \infty). \quad (4.18)$$

The time step parameter represents the rate at which trial particle creation and deletion events are performed, and therefore must bound the absolute integral of the overall collision process (4.2)

$$\int_{\mathcal{D}} d^3\mathbf{x} \int_{\mathcal{R}^3} d^3\mathbf{c} \left| \left[ \frac{\partial f^d(\mathbf{c})}{\partial t} \right]_{\text{coll}} \right| < mW_{\text{eff}}\Lambda, \quad (4.19)$$

where  $mW_{\text{eff}}$  appears in order to relate the time rate of change of  $f^d$  directly to

deviational particles via Equation (3.2).

To derive a value for  $\Lambda$ , a bound for the overall collision process (4.2) is formed from the absolute value of each particle generation and deletion process.

$$\begin{aligned}
& \frac{1}{mW_{\text{eff}}} \int_{\mathcal{D}} d^3\mathbf{x} \int_{\mathcal{R}^3} d^3\mathbf{c} \left| \left[ \frac{\partial f^d(\mathbf{c})}{\partial t} \right]_{\text{coll}} \right| \\
&= \frac{1}{mW_{\text{eff}}} \int_{\mathcal{D}} d^3\mathbf{x} \int_{\mathcal{R}^3} d^3\mathbf{c} \left| \int_{\mathcal{R}^3} d^3\mathbf{c}_* \left[ 2K_{\beta}^{(1)} - K_{\beta}^{(2)} \right] (\mathbf{c}, \mathbf{c}_*) f^d(\mathbf{c}_*) - \nu_{\beta}(\mathbf{c}) f^d(\mathbf{c}) \right| \\
&< \frac{1}{mW_{\text{eff}}} \int_{\mathcal{D}} d^3\mathbf{x} \int_{\mathcal{R}^3} d^3\mathbf{c} \left\{ \int_{\mathcal{R}^3} d^3\mathbf{c}_* \left[ 2K_{\beta}^{(1)} + K_{\beta}^{(2)} \right] (\mathbf{c}, \mathbf{c}_*) f^d(\mathbf{c}_*) + \nu_{\beta}(\mathbf{c}) f^d(\mathbf{c}) \right\}
\end{aligned} \tag{4.20}$$

Next, using the relation (4.13), and the bound on the collision rate function (4.15), an expression for the time step parameter is obtained.

$$\begin{aligned}
& \frac{1}{mW_{\text{eff}}} \int_{\mathcal{D}} d^3\mathbf{x} \int_{\mathcal{R}^3} d^3\mathbf{c} \left| \left[ \frac{\partial f^d(\mathbf{c})}{\partial t} \right]_{\text{coll}} \right| \\
&< \frac{1}{mW_{\text{eff}}} \int_{\mathcal{D}} d^3\mathbf{x} \int_{\mathcal{R}^3} d^3\mathbf{c} \left\{ \int_{\mathcal{R}^3} d^3\mathbf{c}_* \left[ 2K_{\beta}^{(1)} + K_{\beta}^{(2)} \right] (\mathbf{c}, \mathbf{c}_*) f^d(\mathbf{c}_*) + \nu_{\beta}(\mathbf{c}) f^d(\mathbf{c}) \right\} \\
&= \frac{4}{mW_{\text{eff}}} \int_{\mathcal{D}} d^3\mathbf{x} \int_{\mathcal{R}^3} d^3\mathbf{c} \nu_{\beta}(\mathbf{c}) f^d(\mathbf{c}) \\
&\leq \frac{4}{mW_{\text{eff}}} \int_{\mathcal{D}} d^3\mathbf{x} \int_{\mathcal{R}^3} d^3\mathbf{c} \nu_{\beta, \text{max}}(\mathbf{c}) f^d(\mathbf{c}) = 4 \sum_{i=1}^N \nu_{\beta, \text{max}}(\mathbf{c}_i) = \Lambda
\end{aligned} \tag{4.21}$$

In the above derivation, each of the three (two repeated instances of  $K_{\beta}^{(1)}$  and one instance of  $K_{\beta}^{(2)}$ ) collision terms, as well as the deletion term, contribute equally to the overall rate  $\Lambda$ . Collision events are sampled by first selecting an existing particle in the simulation according to the probability

$$P_i^{\text{part}} = \frac{4\nu_{\beta, \text{max}}(\mathbf{c}_i)}{\Lambda}, \tag{4.22}$$

and sampling from the appropriate particle creation or deletion term, as described below.

Distribution (4.18) is sampled directly (see Section A.1.1), and the state of the simulation is advanced by the sampled time step  $\delta t$ , until the simulation time exceeds  $t + \Delta t_{\text{coll}}$ ; at this point, the collision step finishes, and control is passed back to the overall time integration algorithm (Section 3.1). For each time step, a trial particle generation or deletion step is performed, which is accepted or rejected according to the proper probabilities. Following each stochastic time,  $\Lambda$  is updated via Equation (4.21) prior to sampling the subsequent time step.

In the original LVDSMC VHS collision algorithm [61], particle creation and deletion events were processed as a part of a single combined algorithm. However, in the most recent implementation [53], the two processes were split into separate algorithms in order to facilitate mass conservation procedures; this later approach is followed here. As previously noted, each of the three particle creation terms and the particle deletion terms contribute equally to the time step parameter. Thus, for every time step, a trial particle creation step is performed with probability 3/4 and a trial deletion step with the remaining probability, as described in the following sections. Finally, the mass conservation procedure, which makes use of the creation procedure, is discussed.

### 4.3 Particle creation

The particle creation process is formally represented as

$$\left[ \frac{\partial f^d(\mathbf{c})}{\partial t} \right]_{\text{gen}} = \int_{\mathcal{R}^3} d^3 \mathbf{c}_* \left[ 2K_\beta^{(1)} - K_\beta^{(2)} \right] (\mathbf{c}, \mathbf{c}_*) f^d(\mathbf{c}_*). \quad (4.23)$$

The procedure of Wagner [61] is followed here, where an additional function relating to  $K_\beta^{(1)}$  is defined, namely

$$J_\beta^{(1)}(\mathbf{c}, \mathbf{c}_*, \boldsymbol{\zeta}) = \frac{4C_\beta}{\|\mathbf{c} - \mathbf{c}_*\| \|\mathbf{c} - \mathbf{c}_* - \boldsymbol{\zeta}\|^{1-\beta}} \int_{\Gamma_\perp(\mathbf{c}-\mathbf{c}_*)} d^3 \boldsymbol{\zeta}_* f^0(\mathbf{c} + \boldsymbol{\zeta}_*)$$

$$= \frac{4C_\beta \rho_0}{\sqrt{\pi} c_0 \|\mathbf{c} - \mathbf{c}_*\| \|\mathbf{c} - \mathbf{c}_* - \boldsymbol{\zeta}\|^{1-\beta}} \exp\left(-\frac{[(\mathbf{c} - \mathbf{u}_0) \cdot (\mathbf{c} - \mathbf{c}_*)]^2}{c_0^2 \|\mathbf{c} - \mathbf{c}_*\|^2}\right). \quad (4.24)$$

It is proved in Reference [61], that the collision kernel  $K_\beta^{(1)}$  can be represented in terms of an integral of  $J_\beta^{(1)}(\mathbf{c}, \mathbf{c}_*, \boldsymbol{\zeta})$

$$K_\beta^{(1)}(\mathbf{c}, \mathbf{c}_*) = \int_{\mathcal{R}^3} d^3\boldsymbol{\zeta} J_\beta^{(1)}(\mathbf{c}, \mathbf{c}_*, \pi_{\mathbf{c}-\mathbf{c}_*}(\boldsymbol{\zeta})) \frac{f^0(\mathbf{c} + \boldsymbol{\zeta})}{\rho_0}, \quad (4.25)$$

where, the notation  $\pi_{\mathbf{c}}(\boldsymbol{\zeta})$  refers to the vector projection of  $\boldsymbol{\zeta}$  onto the plane passing through the origin and normal to  $\mathbf{c}$ , namely

$$\pi_{\mathbf{c}}(\boldsymbol{\zeta}) = \boldsymbol{\zeta} - \frac{\mathbf{c} \cdot \boldsymbol{\zeta}}{c^2} \mathbf{c}. \quad (4.26)$$

Using Equation (4.14), the following bound on  $J_\beta^{(1)}(\mathbf{c}, \mathbf{c}_*, \boldsymbol{\zeta})$  can be obtained.

$$\begin{aligned} J_\beta^{(1)}(\mathbf{c}, \mathbf{c}_*, \boldsymbol{\zeta}) &\leq J_{\beta, \max}^{(1)}(\mathbf{c}, \mathbf{c}_*, \boldsymbol{\zeta}) \\ &= \frac{4C_\beta \rho_0 c_0^\beta}{\sqrt{\pi} c_0 \|\mathbf{c} - \mathbf{c}_*\|} \left[ \frac{\beta}{c_0} + \frac{1-\beta}{\|\mathbf{c} - \mathbf{c}_* - \boldsymbol{\zeta}\|} \right] \exp\left(-\frac{[(\mathbf{c} - \mathbf{u}_0) \cdot (\mathbf{c} - \mathbf{c}_*)]^2}{c_0^2 \|\mathbf{c} - \mathbf{c}_*\|^2}\right) \end{aligned} \quad (4.27)$$

$$K_{\beta, \max}^{(1)}(\mathbf{c}, \mathbf{c}_*) = \int_{\mathcal{R}^3} d^3\boldsymbol{\zeta} J_{\beta, \max}^{(1)}(\mathbf{c}, \mathbf{c}_*, \pi_{\mathbf{c}-\mathbf{c}_*}(\boldsymbol{\zeta})) \frac{f^0(\mathbf{c} + \boldsymbol{\zeta})}{\rho_0} \quad (4.28)$$

Using the terminology developed above, the creation process (4.23) can be represented as

$$\begin{aligned} \left[ \frac{\partial f^d(\mathbf{c})}{\partial t} \right]_{\text{gen}} &= \int_{\mathcal{R}^3} d^3\mathbf{c}_* \left[ 2 \int_{\mathcal{R}^3} d^3\boldsymbol{\zeta} J_\beta^{(1)}(\mathbf{c}, \mathbf{c}_*, \pi_{\mathbf{c}-\mathbf{c}_*}(\boldsymbol{\zeta})) \frac{f^0(\mathbf{c} + \boldsymbol{\zeta})}{\rho_0} - K_\beta^{(2)}(\mathbf{c}, \mathbf{c}_*) \right] f^d(\mathbf{c}_*) \\ &= \int_{\mathcal{R}^3} d^3\mathbf{c}_* \int_{\mathcal{R}^3} d^3\boldsymbol{\zeta} \left[ 2J_\beta^{(1)}(\mathbf{c}, \mathbf{c}_*, \pi_{\mathbf{c}-\mathbf{c}_*}(\boldsymbol{\zeta})) - K_\beta^{(2)}(\mathbf{c}, \mathbf{c}_*) \right] \frac{f^0(\mathbf{c} + \boldsymbol{\zeta})}{\rho_0} f^d(\mathbf{c}_*). \end{aligned} \quad (4.29)$$

The particle creation process proceeds by selecting a particle  $i$  from the particle index

distribution (4.22), and determining the cell  $j$  in which the particle resides. Next, the integral over  $\mathbf{c}_*$  can be evaluated in terms of the deviational particles in cell  $j$ .

$$\begin{aligned}
\int_{\mathcal{D}_j} d^3\mathbf{x} \left[ \frac{\partial f^d(\mathbf{c})}{\partial t} \right]_{\text{gen}} &= \int_{\mathcal{D}_j} d^3\mathbf{x} \int_{\mathcal{R}^3} d^3\mathbf{c}_* \int_{\mathcal{R}^3} d^3\zeta \\
&\quad \left[ 2J_{\beta}^{(1)}(\mathbf{c}, \mathbf{c}_*, \pi_{\mathbf{c}-\mathbf{c}_*}(\zeta)) - K_{\beta}^{(2)}(\mathbf{c}, \mathbf{c}_*) \right] \frac{f^0(\mathbf{c} + \zeta)}{\rho_0} f^d(\mathbf{c}_*) \\
&= mW_{\text{eff}} \sum_{\ell \in \mathcal{N}_j} s_{\ell} \int_{\mathcal{R}^3} d^3\zeta \left[ 2J_{\beta}^{(1)}(\mathbf{c}, \mathbf{c}_{\ell}, \pi_{\mathbf{c}-\mathbf{c}_{\ell}}(\zeta)) - K_{\beta}^{(2)}(\mathbf{c}, \mathbf{c}_{\ell}) \right] \frac{f^0(\mathbf{c} + \zeta)}{\rho_0} \\
&= mW_{\text{eff}} \int_{\mathcal{R}^3} d^3\zeta \frac{\sum_{\ell \in \mathcal{N}_j} s_{\ell} \left[ 2J_{\beta}^{(1)}(\mathbf{c}, \mathbf{c}_{\ell}, \pi_{\mathbf{c}-\mathbf{c}_{\ell}}(\zeta)) - K_{\beta}^{(2)}(\mathbf{c}, \mathbf{c}_{\ell}) \right]}{\sum_{\ell \in \mathcal{N}_j} \left[ 2J_{\beta, \text{max}}^{(1)}(\mathbf{c}, \mathbf{c}_{\ell}, \pi_{\mathbf{c}-\mathbf{c}_{\ell}}(\zeta)) + K_{\beta, \text{max}}^{(2)}(\mathbf{c}, \mathbf{c}_{\ell}) \right]} \\
&\quad \cdot \sum_{\ell \in \mathcal{N}_j} \nu_{\beta, \text{max}}(\mathbf{c}_{\ell}) \left[ 2 \frac{J_{\beta, \text{max}}^{(1)}(\mathbf{c}, \mathbf{c}_{\ell}, \pi_{\mathbf{c}-\mathbf{c}_{\ell}}(\zeta))}{K_{\beta, \text{max}}^{(1)}(\mathbf{c}, \mathbf{c}_{\ell})} \frac{f^0(\mathbf{c} + \zeta)}{\rho_0} \frac{K_{\beta, \text{max}}^{(1)}(\mathbf{c}, \mathbf{c}_{\ell})}{\nu_{\beta, \text{max}}(\mathbf{c}_{\ell})} \right. \\
&\quad \quad \quad \left. + \frac{f^0(\mathbf{c} + \zeta)}{\rho_0} \frac{K_{\beta, \text{max}}^{(2)}(\mathbf{c}, \mathbf{c}_{\ell})}{\nu_{\beta, \text{max}}(\mathbf{c}_{\ell})} \right] \\
&= mW_{\text{eff}} \int_{\mathcal{R}^3} d^3\zeta s_{\mathbf{c}, \zeta}^{\text{gen}} \mathbb{P}_{\mathbf{c}, \zeta}^{\text{gen}} \sum_{\ell \in \mathcal{N}_j} \nu_{\beta, \text{max}}(\mathbf{c}_{\ell}) \left[ 2r_{\ell, \mathbf{c}}^{(1)}(\zeta) p_{\ell}^{(1)}(\mathbf{c}) + r_{\ell, \mathbf{c}}^{(2)}(\zeta) p_{\ell}^{(2)}(\mathbf{c}) \right]
\end{aligned} \tag{4.30}$$

In the above expression, notations were introduced for the probability densities:  $r_{i, \mathbf{c}}^{(1)}$ ,  $r_{i, \mathbf{c}}^{(2)}$ ,  $p_i^{(1)}$ , and,  $p_i^{(2)}$ ; overall acceptance probability  $\mathbb{P}_{\mathbf{c}, \zeta}^{\text{gen}}$ , and accepted particle sign  $s_{\mathbf{c}, \zeta}^{\text{gen}}$ .

$$r_{i, \mathbf{c}}^{(1)}(\zeta) = \frac{J_{\beta, \text{max}}^{(1)}(\mathbf{c}, \mathbf{c}_i, \pi_{\mathbf{c}-\mathbf{c}_i}(\zeta))}{K_{\beta, \text{max}}^{(1)}(\mathbf{c}, \mathbf{c}_i)} \frac{f^0(\mathbf{c} + \zeta)}{\rho_0} \tag{4.31}$$

$$r_{i, \mathbf{c}}^{(2)}(\zeta) = \frac{f^0(\mathbf{c} + \zeta)}{\rho_0} \tag{4.32}$$

$$p_i^{(1)}(\mathbf{c}) = \frac{K_{\beta, \text{max}}^{(1)}(\mathbf{c}, \mathbf{c}_i)}{\nu_{\beta, \text{max}}(\mathbf{c}_i)} \tag{4.33}$$

$$p_i^{(2)}(\mathbf{c}) = \frac{K_{\beta, \text{max}}^{(2)}(\mathbf{c}, \mathbf{c}_i)}{\nu_{\beta, \text{max}}(\mathbf{c}_i)} \tag{4.34}$$

$$\mathbb{P}_{\mathbf{c}, \boldsymbol{\zeta}}^{\text{gen}} = \frac{\left| \sum_{\ell \in \mathcal{N}_j} s_\ell \left[ 2J_\beta^{(1)}(\mathbf{c}, \mathbf{c}_\ell, \pi_{\mathbf{c}-\mathbf{c}_\ell}(\boldsymbol{\zeta})) - K_\beta^{(2)}(\mathbf{c}, \mathbf{c}_\ell) \right] \right|}{\sum_{\ell \in \mathcal{N}_j} \left[ 2J_{\beta, \text{max}}^{(1)}(\mathbf{c}, \mathbf{c}_\ell, \pi_{\mathbf{c}-\mathbf{c}_\ell}(\boldsymbol{\zeta})) + K_{\beta, \text{max}}^{(2)}(\mathbf{c}, \mathbf{c}_\ell) \right]} \quad (4.35)$$

$$s_{\mathbf{c}, \boldsymbol{\zeta}}^{\text{gen}} = \text{sgn} \left( \sum_{\ell \in \mathcal{N}_j} s_\ell \left[ 2J_\beta^{(1)}(\mathbf{c}, \mathbf{c}_\ell, \pi_{\mathbf{c}-\mathbf{c}_\ell}(\boldsymbol{\zeta})) - K_\beta^{(2)}(\mathbf{c}, \mathbf{c}_\ell) \right] \right) \quad (4.36)$$

Particle creation events can be sampled according to representation (4.30) above by a Monte Carlo sampling approach. First, it is noted that the prefactor within the summation  $\nu_{\beta, \text{max}}(\mathbf{c}_\ell)$  is consistent with the rate at which particle  $i$  is sampled (see Equations (4.21, 4.22)), which implies that we can use  $\mathbf{c}_\ell = \mathbf{c}_i$  in order to produce a trial creation event. Then, a sample  $(\mathbf{c}, \boldsymbol{\zeta})$  is constructed from the  $K_{\beta, \text{max}}^{(1)}$  term with probability 2/3, and from  $K_{\beta, \text{max}}^{(2)}$  term with the remaining probability. Individual procedures for sampling from the relevant distributions are developed in the Sections 4.3.1 and 4.3.2 below. The trial creation event is accepted with probability  $\mathbb{P}_{\mathbf{c}, \boldsymbol{\zeta}}^{\text{gen}}$  by adding a particle with velocity  $\mathbf{c}$ , sign  $s_{\mathbf{c}, \boldsymbol{\zeta}}^{\text{gen}}$ , and a random position  $\mathbf{x} \in \mathcal{D}_j$  sampled uniformly from cell  $j$ ; otherwise, the trial sample is rejected, and the simulation remains unchanged.

The expression (4.35) for the overall acceptance probability implies that the cost of the collision algorithm scales as  $N^2$ , in contrast to DSMC whose cost scales as  $N$ . This unfavorable scaling is addressed in two ways. First, as we shall show in the results section, typical simulations using the mass conservative version of this algorithm only require  $\sim 10$  particles per cell to achieve surprisingly well-resolved output: this is the strategy employed for the majority of simulations reported in this thesis. Secondly, even when simulations are performed with significantly more particles per cell in simulation, an upper bound on the number of particles per cell to be used for evaluating  $\mathbb{P}_{\mathbf{c}, \boldsymbol{\zeta}}^{\text{gen}}$ . For this purpose, we define a subset  $\mathcal{M}_i \subseteq \mathcal{N}_j$  of the total number of particles in cell  $j$ , which contains  $\max(N_{\mathbf{C}, j}, N_{\text{sum}})$ , where  $N_{\mathbf{C}, j}$  is the number of particles in cell  $j$  and  $N_{\text{sum}}$  is a chosen parameter. Subset  $\mathcal{M}_i$  consists of particle  $i$  and the remainder chosen randomly with a uniform probability. Thus, when there are fewer than  $N_{\text{sum}}$  particles in a cell, the summation is performed over the entire set  $\mathcal{N}_j$ ; otherwise, over the subset  $\mathcal{M}_i$ . This results in a simple modification

to the acceptance probability

$$\mathbb{P}_{\mathbf{c}, \zeta}^{\text{gen}} = \frac{\left| \sum_{\ell \in \mathcal{M}_i} s_\ell \left[ 2J_\beta^{(1)}(\mathbf{c}, \mathbf{c}_\ell, \pi_{\mathbf{c}-\mathbf{c}_\ell}(\zeta)) - K_\beta^{(2)}(\mathbf{c}, \mathbf{c}_\ell) \right] \right|}{\sum_{\ell \in \mathcal{M}_i} \left[ 2J_{\beta, \max}^{(1)}(\mathbf{c}, \mathbf{c}_\ell, \pi_{\mathbf{c}-\mathbf{c}_\ell}(\zeta)) + K_{\beta, \max}^{(2)}(\mathbf{c}, \mathbf{c}_\ell) \right]}, \quad (4.37)$$

and has the effect of limiting the  $N^2$  dependence to only the cells with a small number of particles.

Further generalizations of this procedure are discussed in Reference [61], in which the particle subsets  $\mathcal{M}_i$  are chosen differently, for example, as clusters of particles with similar velocities. This procedure was not explored in this work, but merits future investigation.

### 4.3.1 Sampling particle trial particle velocities from the $K_{\beta, \max}^{(2)}$ term

For 1/3 of trial particle generation events, the trial velocity is sampled from distribution (4.34) which, using Equation (4.17), can be represented in the form

$$p_i^{(2)}(\mathbf{c}) = \frac{4\pi C_\beta c_0^\beta}{\nu_{\beta, \max}(\mathbf{c}_i)} \left[ \frac{\|\mathbf{c} - \mathbf{c}_i\|}{c_0} + (1 - \beta) \right] f^0(\mathbf{c}). \quad (4.38)$$

This distribution can be effectively sampled using the following algorithm [61]:

**Algorithm 4.1.** Algorithm for sampling  $p_i^{(2)}(\mathbf{c})$

1. With probability

$$\frac{1 - \beta}{\beta\phi(\xi_i) + (1 - \beta)},$$

produce a sample  $\mathbf{c}$  from  $f^0(\mathbf{c})$  (see Section A.1.2) and exit.

2. With probability

$$\frac{2c_0}{2c_0 + \sqrt{\pi}\|\mathbf{c}_i - \mathbf{u}_0\|}$$

go to step 2.2.

- 2.1 Generate a trial sample  $\mathbf{c}$  from distribution  $f^0(\mathbf{c})$  and go to step 3.

2.2 Generate a trial sample  $\mathbf{c}$  from  $\|\mathbf{c} - \mathbf{u}_0\|f^0(\mathbf{c})$ .

3. With probability

$$\frac{\|\mathbf{c} - \mathbf{c}_i\|}{\|\mathbf{c} - \mathbf{c}_i\| + \|\mathbf{c} - \mathbf{u}_0\|},$$

exit the routine.

4. Go back to step 2.

Samples from the the distribution  $\|\mathbf{c} - \mathbf{u}_0\|f^0(\mathbf{c})$  can sampled by exploiting the spherical symmetry, resulting in

$$\frac{\mathbf{c} - \mathbf{u}_0}{c_0} = \xi\Omega, \quad (4.39)$$

where  $\xi \in [0, \infty)$  is sampled from  $2\xi^3 e^{-\xi^2}$  (algorithm A.1) and  $\Omega$  is sampled from the unit sphere (Section A.1.4).

Next, based on  $\mathbf{c}$ , a sample of the auxiliary variable  $\zeta$  is produced from (4.32), which is obtained simply  $\zeta = \mathbf{c}_* - \mathbf{c}$ , where  $\mathbf{c}_*$  is sampled from  $f^0(\mathbf{c}_*)$ , which allows the evaluation of the overall acceptance probability (4.35).

### 4.3.2 Sampling particle trial particle velocities from the $K_{\beta, \max}^{(1)}$ term

For the other 2/3 of the trial particle generation events, trial velocities are sampled from distribution (4.33), which is significantly more complex. The sampling procedure developed by Wagner [61] uses algorithm 4.1 to produce a sample  $\mathbf{c}$ , which is then replaced by one of its post collision values  $\mathbf{c} \rightarrow \mathbf{c}'$ , where  $\mathbf{c}' = \frac{1}{2}(\mathbf{c} + \mathbf{c}_i + \|\mathbf{c} + \mathbf{c}_i\|\Omega)$  and  $\Omega$  is again sampled from the unit sphere.

Next, based on  $\mathbf{c}$ , a sample of the auxiliary variable  $\zeta$  is produced from (4.31), which is obtained by a simple modification to algorithm 4.1 [61], which again allows the evaluation of the overall acceptance probability (4.35).

**Algorithm 4.2.** Algorithm for sampling  $r_{i, \mathbf{c}}^{(1)}(\zeta)$

1. Produce a sample  $\zeta$  from distribution (4.31) using algorithm 4.1.
2. With probability

$$\frac{\beta/c_0 + (1 - \beta)\|\mathbf{c} - \mathbf{c}_i - \pi_{\mathbf{c}-\mathbf{c}_i}(\zeta)\|^{-1}}{\beta/c_0 + (1 - \beta)\|\mathbf{c} - \mathbf{c}_i\|^{-1}}$$

exit the routine.

3. Go to step 1.

## 4.4 Particle deletion

Recall that for each stochastic time step (4.18), a trial deletion step is performed with probability  $1/4$ . For a particle with index  $i$ , chosen randomly according to the particle index distribution (4.22), the deletion process is formally represented as

$$\left[ \frac{\partial f^d(\mathbf{c}_i)}{\partial t} \right]_{\text{del}} = -\nu_\beta(\mathbf{c}_i) f^d(\mathbf{c}_i). \quad (4.40)$$

By introducing Equation (4.12) and rearranging, the following expression is obtained:

$$\begin{aligned} \left[ \frac{\partial f^d(\mathbf{c}_i)}{\partial t} \right]_{\text{del}} &= -4\pi C_\beta \int_{\mathcal{R}^3} d^3\zeta \|\mathbf{c}_i - \zeta\|^\beta f^0(\zeta) f^d(\mathbf{c}_i) \\ &= -\nu_{\beta, \max}(\mathbf{c}_i) \int_{\mathcal{R}^3} d^3\zeta \frac{4\pi C_\beta c_0^\beta}{\nu_{\beta, \max}(\mathbf{c}_i)} \left[ \beta \frac{\|\mathbf{c}_i - \zeta\|}{c_0} + (1 - \beta) \right] f^0(\zeta) \\ &\quad \cdot \frac{(\|\mathbf{c}_i - \zeta\|/c_0)^\beta}{\beta \|\mathbf{c}_i - \zeta\|/c_0 + (1 - \beta)} f^d(\mathbf{c}_i) \\ &= -\nu_{\beta, \max}(\mathbf{c}_i) \int_{\mathcal{R}^3} d^3\zeta p_i^{(2)}(\zeta) \mathbb{P}_{i, \zeta}^{\text{del}} f^d(\mathbf{c}_i). \end{aligned} \quad (4.41)$$

The deletion algorithm is obtained from the above representation. First, it is noted that the prefactor  $\nu_{\beta, \max}(\mathbf{c}_i)$  is consistent with the rate at which particle  $i$  is sampled (see Equations (4.21, 4.22)). For the trial deletion step, the deletion probability is

evaluated by sampling a velocity  $\zeta$  is from the probability density function  $p_i^{(2)}(\zeta)$ . With probability

$$\mathbb{P}_{i,\zeta}^{\text{del}} = \frac{(\|\mathbf{c}_i - \zeta\|/c_0)^\beta}{\beta\|\mathbf{c}_i - \zeta\|/c_0 + (1 - \beta)}, \quad (4.42)$$

the particle  $i$  is removed from the simulation. Otherwise, the trial deletion step finishes without affecting the particle population.

## 4.5 Mass conservation

The LVDSMC collision algorithm conserves mass, momentum, and energy only on average; this is a weaker sense of conservation compared to DSMC, which conserves these quantities for individual collision events (c.f. Section 1.2). The approach outlined here enforces mass conservation for each collision time step  $\Delta t_{\text{coll}}$  by appropriate stochastic particle generation and deletion events. Before a full discussion of mass conservation procedures can ensue, a few quantities must be defined.

In the mass conservation approach, a list of particles generated from the particle creation routine must be continuously maintained during the entire collision routine. At the beginning of the collision step, this list will be empty, but during the collision step, each particle generated by the creation routine (Section 4.3) is added to the list and stored unless it is subsequently removed from simulation by a deletion step. This list of particles will be designated  $\mathcal{G}$ , which contains  $N_{\mathcal{G}}$  particles, and is partitioned  $\mathcal{G} = \mathcal{G}^+ \cup \mathcal{G}^-$  into a set  $\mathcal{G}^+$  of  $N_{\mathcal{G}}^+$  positive, and a set  $\mathcal{G}^-$  of  $N_{\mathcal{G}}^-$  negative particles at the current state. Also defined is a total mass residual for collisions,  $\Delta S$ , which is continually tracked throughout the entire simulation. First, it is initialized to be zero, unless it is available from a restart file, and then, it is updated for each particle creation event with sign  $s$  via  $\Delta S \rightarrow \Delta S + s$  and for each particle deletion step with sign  $s$  via  $\Delta S \rightarrow \Delta S - s$ . At the end of each collision step, new particles are generated from the creation (Section 4.3) routine and existing particles are deleted randomly (and uniformly) from  $\mathcal{G}$  in order to enforce the optimal level of mass conservation.

Typically, this optimum level of mass conservation results in  $\Delta S = 0$ , but when

this is not possible, the remaining  $\Delta S$  is carried over to be addressed in the subsequent collision step. The overall mass conservation procedure consists of particle resampling steps which consist of removing a single particle of an undesirable sign  $s$  from  $\mathcal{G}$  and generating a new particle ensuring that the result has the opposite sign  $-s$ . Clearly, this approach cannot achieve  $\Delta S = 0$  if  $N_{\mathcal{G}} = N_{\mathcal{G}}^+ + N_{\mathcal{G}}^-$  is an odd number; thus, the initial step in the mass conservation process is to correct the parity of mass residual. The parity correction step consists of repeating the particle generation routine until a single particle is accepted, with probability 1/2; or by deleting a random particle (uniformly) from  $\mathcal{G}$  (by removing it from the simulation), with probability 1/2. Clearly, this step can only be performed if  $N_{\mathcal{G}} > 0$ ; otherwise  $\Delta S$  cannot be changed in the current time step, and the parity correction step (as well as the resampling step, below) will be skipped entirely.

Based on set  $\mathcal{G}$ , the optimal mass residual  $\Delta S_{\text{opt}}$  is defined as the value of  $\Delta S$  with the lowest absolute value which can be attained by particle resampling events.

$$\Delta S_{\text{opt}} = \begin{cases} 0 & \text{if } N_{\mathcal{G}}^{\mp} \geq \frac{1}{2}|\Delta S| \text{ and } \Delta S \leq 0 \\ \Delta S \pm 2N_{\mathcal{G}}^{\mp} & \text{if } N_{\mathcal{G}}^{\mp} < \frac{1}{2}|\Delta S| \text{ and } \Delta S \leq 0. \end{cases} \quad (4.43)$$

For the trivial case,  $\Delta S = \Delta S_{\text{opt}} = 0$  and no resampling is needed.

The resampling procedure consists of performing the following two steps in random order: (i) delete a random particle (uniformly) from  $\mathcal{G}^{\text{sgn}(\Delta S)}$ , and (ii) generate a particle with sign  $-\text{sgn}(\Delta S)$ . In step (ii), we use the particle generation step used in the collision routine, repeating the routine automatically rejecting all particles with sign  $\text{sgn}(\Delta S)$  until a single particle is generated with the correct sign, which is added to the simulation. This procedure is repeated until  $\Delta S = \Delta S_{\text{opt}}$ , and control is passed back to the overall LVDSMC simulation (algorithm 3.1).



# Chapter 5

## Simulation of the Bhatnagar-Gross-Krook Gas

In this chapter, a collision algorithm for the Bhatnagar-Gross-Krook (BGK) collision operator is outlined. This algorithm is based on the formulation used in Chapter 4 (for the VHS model) and thus inherits the desirable properties of the former method, like the lack of inherent time step error as well as mass conservation. These features were not included in previous methods [52, 29]. As before, only the collision routine is described here, which is designed to work with the overall LVDSMC simulation method presented in Chapter 3.

Based on the global equilibrium distribution  $f^{\text{eq}} = f^0$ , the BGK collision operator in deviational form can be expressed as

$$\left[ \frac{\partial f^{\text{d}}(\mathbf{c})}{\partial t} \right]_{\text{coll}} = \frac{f^{\text{loc}}(\mathbf{c}) - f^0(\mathbf{c})}{\tau} - \frac{f^{\text{d}}(\mathbf{c})}{\tau}. \quad (5.1)$$

Note that the same essential structure appears here as it did in the linear part of the VHS operator (4.9): namely a source term  $\frac{1}{\tau}[f^{\text{loc}}(\mathbf{c}) - f^0(\mathbf{c})]$  from which fresh particles are generated, and a sink term  $-\frac{1}{\tau}f^{\text{d}}(\mathbf{c})$  which removes particles from the simulation, resulting in an inherently stable method. Compared to the VHS version, the BGK source term has a different structure, which is much simpler to generate samples from. A key difference is that the source term depends on  $f^{\text{d}}$  through the

local equilibrium properties  $\rho$ ,  $\mathbf{u}$ ,  $T$  appearing in the local equilibrium distribution (1.4), rather than appearing directly in the collision operator. However, it is relatively straightforward to keep continuously updated hydrodynamic properties by tracking the following moments in each cell:  $\sum_{i \in \mathcal{N}_j} s_i$ ,  $\sum_{i \in \mathcal{N}_j} s_i \mathbf{c}_i$ , and  $\sum_{i \in \mathcal{N}_j} s_i c_i^2$ . This is performed by first initializing each value at the start of the collision step, and adding (or subtracting) the appropriate value for each particle creation (or deletion) event. Then, before each stochastic time step, the properties are evaluated directly using Equations (3.52–3.55).

## 5.1 Stochastic collision time steps

Like the VHS collision algorithm, the BGK collision process is formulated in terms of Markov creation and deletion events occurring with exponentially distributed (4.18) stochastic time steps with parameter  $\Lambda$ , which is obtained from an upper bound on the absolute integral of Equation (5.1) over all physical and velocity space (c.f. Equation 4.21).

$$\begin{aligned}
& \frac{1}{mW_{\text{eff}}} \int_{\mathcal{D}} d^3\mathbf{x} \int_{\mathcal{R}^3} d^3\mathbf{c} \left| \left[ \frac{\partial f^d(\mathbf{c})}{\partial t} \right]_{\text{coll}} \right| \\
&= \frac{1}{mW_{\text{eff}}} \int_{\mathcal{D}} d^3\mathbf{x} \int_{\mathcal{R}^3} d^3\mathbf{c} \left| \frac{f^{\text{loc}}(\mathbf{c}) - f^0(\mathbf{c})}{\tau} - \frac{f^d(\mathbf{c})}{\tau} \right| \\
&< \frac{1}{mW_{\text{eff}}} \int_{\mathcal{D}} d^3\mathbf{x} \int_{\mathcal{R}^3} d^3\mathbf{c} \left[ \frac{|f^{\text{loc}}(\mathbf{c}) - f^0(\mathbf{c})|}{\tau} + \frac{|f^d(\mathbf{c})|}{\tau} \right] \\
&= \frac{1}{mW_{\text{eff}}} \sum_{j=1}^{N_{\Delta V}} \frac{1}{\tau_j} \int_{\mathcal{D}_j} d^3\mathbf{x} \int_{\mathcal{R}^3} d^3\mathbf{c} \left[ |f^{\text{loc}}(\mathbf{c}) - f^0(\mathbf{c})| + |f^d(\mathbf{c})| \right] \quad (5.2)
\end{aligned}$$

In the above,  $\tau_j$  is the relaxation time based on the local properties defined for cell  $j$  (see Section 1.1.2).

In order to proceed, an integral bound on the difference  $|f^{\text{loc}}(\mathbf{c}) - f^0(\mathbf{c})|$  is required. For cell  $j$ , the source term involves sampling from the following distribution

$$\int_{\mathcal{D}_j} d^3 \mathbf{x} [f^{\text{loc}}(\mathbf{c}) - f^0(\mathbf{c})] d^3 \mathbf{c} = \Delta V_j [f_j^{\text{loc}}(\mathbf{c}) - f^0(\mathbf{c})] d^3 \mathbf{c}$$

$$= \Delta V_j \overline{\rho_{\text{loc},j}} F^{\text{loc},j}(\mathbf{c}) d^3 \boldsymbol{\xi} \quad (5.3)$$

$$F^{\text{loc},j}(\mathbf{c}) = \frac{\overline{c_{\text{loc},j}}^3}{\overline{\rho_{\text{loc},j}}} [f_j^{\text{loc}}(\mathbf{c}) - f^0(\mathbf{c})]. \quad (5.4)$$

Here,  $f_j^{\text{loc}}$  is based on the local properties for cell  $j$ , the dimensionless velocity is  $\boldsymbol{\xi} = (\mathbf{c} - \overline{\mathbf{u}_{\text{loc},j}})/\overline{c_{\text{loc},j}}$ , and the average properties are

$$\overline{\rho_{\text{loc},j}} = \frac{1}{2} (\rho_{\text{loc},j} + \rho_0) \quad (5.5)$$

$$\overline{\mathbf{u}_{\text{loc},j}} = \frac{1}{2} (\mathbf{u}_{\text{loc},j} + \mathbf{u}_0) \quad (5.6)$$

$$\overline{c_{\text{loc},j}} = \frac{1}{2} (c_{\text{loc},j} + c_0). \quad (5.7)$$

Using the ratio-of-uniforms method (Section A.3.1) the variable transformation  $|F^{\text{loc},j}| = H^{5/2}$  and  $\boldsymbol{\xi} = \boldsymbol{\eta}/\sqrt{H}$  is applied. Using the bounds in the transformed variable space

$$0 \leq H \leq a^{\text{loc},j} \quad (5.8)$$

$$-b_x^{\text{loc},j} \leq \eta_x \leq b_x^{\text{loc},j} \quad (5.9)$$

$$-b_y^{\text{loc},j} \leq \eta_y \leq b_y^{\text{loc},j} \quad (5.10)$$

$$-b_z^{\text{loc},j} \leq \eta_z \leq b_z^{\text{loc},j}, \quad (5.11)$$

the following integral bound on  $|f_j^{\text{loc}} - f^0|$  is obtained.

$$\int_{\mathcal{D}_j} d^3 \mathbf{x} \int_{\mathcal{R}^3} d^3 \mathbf{c} |f^{\text{loc}}(\mathbf{c}) - f^0(\mathbf{c})| = \overline{\rho_{\text{loc},j}} \Delta V_j \int_{\mathcal{R}^3} d^3 \boldsymbol{\xi} |F^{\text{loc},j}(\mathbf{c})|$$

$$= \overline{\rho_{\text{loc},j}} \Delta V_j \int_{\mathcal{R}^3} d^3 \boldsymbol{\eta} \left| \frac{\partial (|F^{\text{loc},j}|, \boldsymbol{\xi})}{\partial (H, \boldsymbol{\eta})} \right| H(\boldsymbol{\eta})$$

$$\begin{aligned}
& < \overline{\rho_{\text{loc},j}} \Delta V_j \int_{-b_x^{\text{loc},j}}^{b_x^{\text{loc},j}} d^3 \eta_x \int_{-b_y^{\text{loc},j}}^{b_y^{\text{loc},j}} d^3 \eta_y \int_{-b_z^{\text{loc},j}}^{b_z^{\text{loc},j}} d^3 \eta_z \frac{5}{2} a^{\text{loc},j} \\
& = 20 \overline{\rho_{\text{loc},j}} \Delta V_j a^{\text{loc},j} b_x^{\text{loc},j} b_y^{\text{loc},j} b_z^{\text{loc},j}
\end{aligned} \tag{5.12}$$

With the above bound determined, the expression (5.2) is complete, resulting in the time step parameter

$$\begin{aligned}
& \frac{1}{mW_{\text{eff}}} \int_{\mathcal{D}} d^3 \mathbf{x} \int_{\mathcal{R}^3} d^3 \mathbf{c} \left| \left[ \frac{\partial f(\mathbf{c})}{\partial t} \right]_{\text{coll}} \right| \\
& = \frac{1}{mW_{\text{eff}}} \sum_{j=1}^{N_{\Delta V}} \frac{1}{\tau_j} \int_{\mathcal{D}_j} d^3 \mathbf{x} \int_{\mathcal{R}^3} d^3 \mathbf{c} [|f^{\text{loc}}(\mathbf{c}) - f^0(\mathbf{c})| + |f^{\text{d}}(\mathbf{c})|] \\
& < \sum_{j=1}^{N_{\Delta V}} \frac{1}{\tau_j} \left( 20 a^{\text{loc},j} b_x^{\text{loc},j} b_y^{\text{loc},j} b_z^{\text{loc},j} \frac{\overline{\rho_{\text{loc},j}} \Delta V_j}{mW_{\text{eff}}} + N_{\text{C},j} \right) \\
& = \sum_{j=1}^{N_{\Delta V}} \frac{1}{\tau_j} \left( 20 a^{\text{loc},j} b_x^{\text{loc},j} b_y^{\text{loc},j} b_z^{\text{loc},j} \frac{\overline{\rho_{\text{loc},j}} \Delta V_j}{mW_{\text{eff}}} + N_{\text{C},j} \right) \\
& = \sum_{j=1}^{N_{\Delta V}} \frac{1}{\tau_j} (B^{\text{loc},j} + N_{\text{C},j}) = \Lambda,
\end{aligned} \tag{5.13}$$

where

$$B^{\text{loc},j} = 20 a^{\text{loc},j} b_x^{\text{loc},j} b_y^{\text{loc},j} b_z^{\text{loc},j} \frac{\overline{\rho_{\text{loc},j}} \Delta V_j}{mW_{\text{eff}}}. \tag{5.14}$$

Using this value of  $\Lambda$ , stochastic time steps can be processed (see Equation 4.18, and surrounding text) as before. But unlike the VHS version, which selects a particle for which to produce trial creation and deletion events, the BGK version performs procedures based on a cell  $j$ , which is selected according to

$$P_j^{\text{cell}} = \frac{B^{\text{loc},j} + N_{\text{C},j}}{\Lambda \tau_j}. \tag{5.15}$$

For each stochastic time step occurring in cell  $j$ , trial particle creation steps are processed with probability  $B^{\text{loc},j} / (B^{\text{loc},j} + N_{\text{C},j})$ , and random particles are removed (uniformly) from cell  $j$  with the remaining probability. Mass conservation for the

BGK collision routine uses the same algorithm developed for the VHS collision operator (Section 4.5), which makes use of the BGK particle creation algorithm described below.

## 5.2 Particle creation

Estimates for the bounds used for particle creation follow a similar procedure to those for generating particles at the boundaries (see Section 3.2), namely, by expanding the function  $F^{\text{loc},j}$  to first order in the perturbations of the local equilibrium properties  $(\rho_{\text{loc}}, \mathbf{u}_{\text{loc}}, c_{\text{loc}})$  with respect to the global equilibrium properties

$$\begin{aligned}
 F^{\text{loc},j}(\mathbf{c}) &\approx F^{\text{loc0},j}(\mathbf{c}) \\
 &= \left[ \left( \frac{\rho_{\text{loc},j} - \rho_0}{\rho_{\text{loc},j}} - 3 \frac{c_{\text{loc},j} - c_0}{c_{\text{loc},j}} \right) + 2 \frac{\mathbf{u}_{\text{loc},j} - \mathbf{u}_0}{c_{\text{loc},j}} \cdot \boldsymbol{\xi} + 2 \frac{c_{\text{loc},j} - c_0}{c_{\text{loc},j}} \xi^2 \right] \frac{e^{-\xi^2}}{\pi^{3/2}}.
 \end{aligned} \tag{5.16}$$

Using the same ideas (Section A.3.1), the ratio-of-uniforms bounds for small departures from equilibrium is obtained as follows

$$\begin{bmatrix} (a^{\text{loc0},j})^{5/2} \\ (b_x^{\text{loc0},j})^5 \\ (b_y^{\text{loc0},j})^5 \\ (b_z^{\text{loc0},j})^5 \end{bmatrix} = \mathbf{M}_{\text{loc}} \cdot \begin{bmatrix} \left| \frac{\rho_{\text{loc},j} - \rho_0}{\rho_{\text{loc},j}} - 3 \frac{c_{\text{loc},j} - c_0}{c_{\text{loc},j}} \right| \\ 2 \frac{|u_{\text{loc},j,x} - u_{0,x}|}{c_{\text{loc},j}} \\ 2 \frac{|u_{\text{loc},j,y} - u_{0,y}|}{c_{\text{loc},j}} \\ 2 \frac{|u_{\text{loc},j,z} - u_{0,z}|}{c_{\text{loc},j}} \\ 2 \frac{|c_{\text{loc},j} - c_0|}{c_{\text{loc},j}} \end{bmatrix} \tag{5.17}$$

$$\mathbf{M}_{\text{loc}} = \frac{1}{\pi^{3/2}} \begin{bmatrix} 1 & 1/\sqrt{2e} & \sqrt{1/(2e)} & \sqrt{1/(2e)} & 1/e \\ [5/(2e)]^{5/2} & (3/e)^3 & 5^{5/2}/(2e)^3 & 5^{5/2}/(2e)^3 & [7/(2e)]^{7/2} \\ [5/(2e)]^{5/2} & 5^{5/2}/(2e)^3 & (3/e)^3 & 5^{5/2}/(2e)^3 & [7/(2e)]^{7/2} \\ [5/(2e)]^{5/2} & 5^{5/2}/(2e)^3 & 5^{5/2}/(2e)^3 & (3/e)^3 & [7/(2e)]^{7/2} \end{bmatrix}. \quad (5.18)$$

From these bounds developed for small departures from equilibrium, the actual bounds are formed using  $Y$  factors, which are updated using the process described in a previous chapter (Section 3.2).

$$a^{\text{loc},j} = Y_a^{\text{loc}} a^{\text{loc}0,j} \quad (5.19)$$

$$b_x^{\text{loc},j} = Y_{b,x}^{\text{loc}} b_x^{\text{loc}0,j} \quad (5.20)$$

$$b_y^{\text{loc},j} = Y_{b,y}^{\text{loc}} b_y^{\text{loc}0,j} \quad (5.21)$$

$$b_z^{\text{loc},j} = Y_{b,z}^{\text{loc}} b_z^{\text{loc}0,j} \quad (5.22)$$

For each trial creation step, a sample  $(H, \boldsymbol{\eta})$  is generated (uniformly) utilizing bounds (5.19–5.22). The trial particle velocity is determined via  $\mathbf{c} = \overline{\mathbf{u}}_{\text{loc},j} + \overline{c}_{\text{loc},j} \boldsymbol{\eta} / \sqrt{H}$ , and  $F^{\text{loc},j}(\mathbf{c})$  is evaluated; particles are accepted when  $H < |F^{\text{loc},j}(\mathbf{c})|^{2/5}$ . Accepted particles are advected a random fraction of the advective time step away (performing ordinary DSMC reflection procedures for any boundary interactions) from a uniformly distributed random position on the boundary surface element and added to the simulation with sign  $\text{sgn}[F^{\text{loc},j}(\mathbf{c})]$ .

# Chapter 6

## Validation and Performance

The computational procedures outlined in the previous chapters for simulating the VHS and BGK collision models were implemented in FORTRAN 95. A number of simulations were performed in order to verify that they correctly simulate the BTE for the VHS and BGK collision models, to show that the mass-conservative LVDSMC approach dramatically outperforms the DSMC method in near-equilibrium flow regimes, and to showcase the method's ability to produce exceptionally smooth results for a wide variety of physical problems. In addition, a select number of applications are presented in Chapter 7.

In all cases presented here, we simulate the deviation from a global equilibrium distribution (with  $\mathbf{u}_0 = 0$ ). The normalized characteristic deviation from equilibrium is quantified by  $\epsilon$ , which is typically related to the characteristic temperature difference ( $\epsilon = \Delta T/T_0$ ) or flow velocity (e.g.  $\epsilon = U/c_0$ , with characteristic velocity scale  $U$ ) of the problem. As previously observed [52, 29, 54], in contrast to DSMC, the cost of LVDSMC calculations for a fixed statistical uncertainty does not increase as  $\epsilon$  decreases, and for this reason, all results presented here are scaled by  $\epsilon$ .

### 6.1 Convergence

The accuracy of the LVDSMC method, like the DSMC method on which it is based, depends on the spatial cell size  $\Delta x$ , the overall time step  $\Delta t$  and the average number

of computational particles per cell  $\overline{N}_C$ . The LVDSMC simulation approach utilizes  $\Delta x$  and  $\Delta t$  in similar ways to DSMC; however, the average number of computational particles per cell  $\overline{N}_C$  has a dramatically different behavior in each method, and merits further discussion.

In the DSMC method, the number of simulation particles is well defined in terms of problem and discretization parameters. For example, the average number of particles per cell for a simulation with zero-mass-flux boundary conditions is given by

$$\overline{N}_C = \frac{\rho_0 \overline{\Delta V}}{m N_{\text{eff}}}, \quad (6.1)$$

where  $\overline{\Delta V} = V/N_{\Delta V}$  is the average cell volume; here, we have taken  $\rho_0$  to be the density of the initial state. However, for the LVDSMC method, the local number of particles depends on the local deviation from equilibrium, and as a result,  $\overline{N}_C$  depends on the “average” degree of deviation from equilibrium  $\epsilon$ , for which no established measure exists.

For a suitably defined  $\epsilon$ , and for a large number of simulation cases considered in the course of this research, it was observed that the number of particles per cell, at a nontrivial steady state, can be approximately scaled using

$$\Xi = \frac{\epsilon \rho_0 \overline{\Delta V}}{m W}, \quad (6.2)$$

in the sense that  $\overline{N}_C \sim \Xi$ . In other words, instead of using  $\overline{N}_C$  as a separate convergence parameter (as in DSMC), the parameter  $\Xi$  is used. This is illustrated in Figure 6-1 which shows the actual number of particles for various values of  $\Delta x$  and  $\Xi$  for heat transfer between parallel plates at  $Kn = 0.1$ ; the gas is argon ( $\omega = 0.81$ ) and the boundary conditions are diffusely-reflecting ( $\alpha = 1$ ) with temperatures  $T_B(0) = (1 + \epsilon)T_0$  and  $T_B(L) = (1 - \epsilon)T_0$ , where  $\epsilon \ll 1$ . The figure shows that for large  $\Xi$ , there is a direct relationship between  $\overline{N}_C$  and  $\Xi$ , while for small  $\Xi$ , the smaller number of particles makes the “particle cancellation effect” in Eq. (4.35) less effective (see Section 4.1 and discussion in Reference [61]) leading to a larger number of particles.

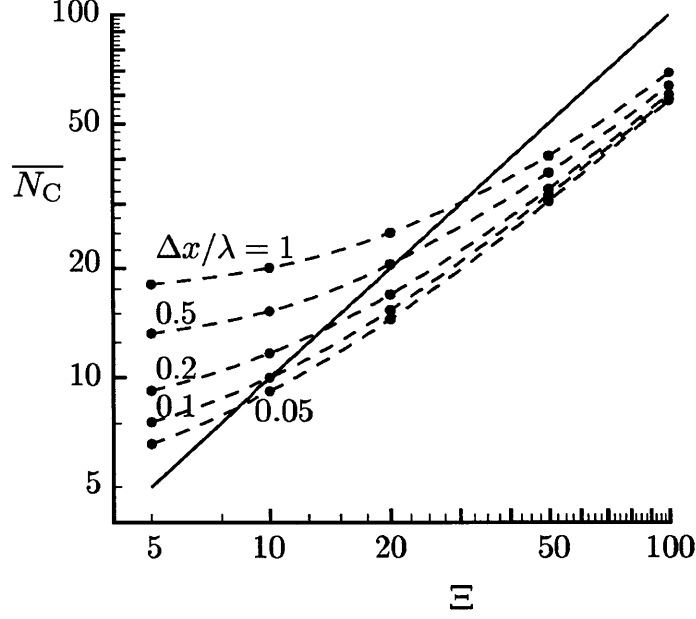


Figure 6-1: Average number of deviational particles per cell for heat transfer through a layer of argon gas confined between diffusely-reflecting parallel plates at  $Kn = 0.1$ . The data (symbols) are shown in terms of the convergence parameters ( $\Delta x$ ,  $\Xi$ ), while the line indicates  $\overline{N}_C = \Xi$ , for comparison.

For all simulation results presented in this chapter, excellent results were achieved using  $\Xi = 10$ . This is significant because it demonstrates that simulations with approximately 10 particles per cell are achievable in mass-conservative LVDSMC simulations *without apparent random walks in any non-negligible hydrodynamic variables*, a substantial improvement over the previous implementation [54]. This dramatic improvement enables efficient simulation in multiple spatial dimensions, as is shown in the results below.

Here, and in the remainder of the simulations reported in this thesis, the time step was chosen as  $\Delta t = \Delta x / c_0$ , where  $\Delta x$  is the smallest cell dimension, which effectively lumps the effect of  $\Delta x$  and  $\Delta t$  in a single discretization parameter ( $\Delta x$ ).

A preliminary convergence study was performed for the relative error in heat flux

$$E_{q_n} = \left| \frac{q_n - q_{n,\text{ref}}}{q_{n,\text{ref}}} \right| \quad (6.3)$$

for heat transfer through argon with  $Kn = 0.1$  for a range of  $\Xi$  and  $\Delta x$ . For this

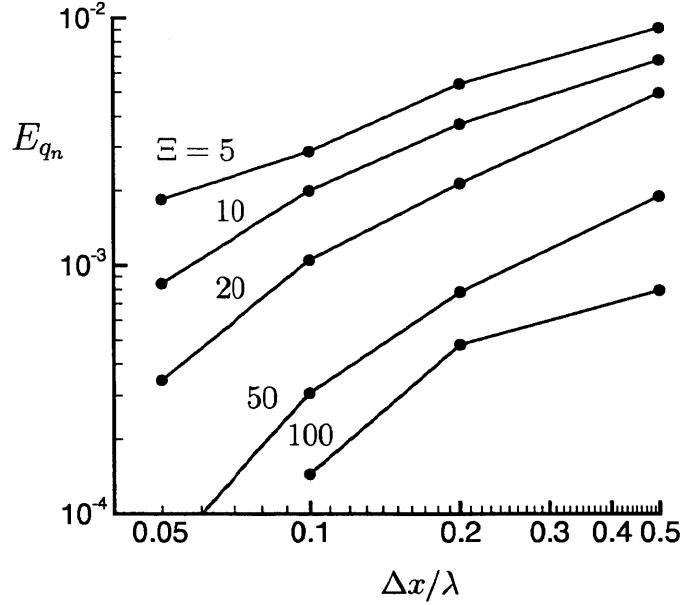


Figure 6-2: Absolute error in the steady state heat flux for argon gas confined between diffusely reflecting parallel plates at  $Kn = 0.1$  as a function of the parameter  $\Xi$  and spatial cell size  $\Delta x$ . As discussed in the text  $\Delta x$  also controls the time step size through  $\Delta t = \Delta x/c_0$

case, the reference heat flux  $q_{n,\text{ref}}$  was taken to be the computed value at  $\Xi = 100$  and  $\Delta x/\lambda = 0.05$ . The simulation results shown in Figure 6-2 demonstrate a decreased relative error with increased  $\Xi$  and decreased  $\Delta x$  as expected, although they are too noisy to establish the rate of convergence (as has been done for DSMC [51], for example). More rigorous convergence studies for the method are needed, but due to the significant computational resources required, these are left to future work.

## 6.2 Variance reduction

In this section, we discuss the degree of variance reduction achieved by the method outlined in this thesis for a simple problem. The variance was computed in the boundary cells of a steady heat transfer problem in argon gas for various Knudsen numbers. Recall from Section 1.2.4 that in non-variance reduced methods (e.g. DSMC) the relative statistical error in the hydrodynamic fields scales inversely to the departure from equilibrium (see Reference [28] and Equations (1.24) and (1.25)).

The form of Equation (1.25) suggests that the quantity  $N_C N_{\text{ens}} \sigma_T^2 / (\Delta T)^2$  is a good metric for the performance of the method for small departures from equilibrium, since for DSMC this is given by

$$\frac{N_{\text{ens}} N_C \sigma_T^2}{\Delta T^2} = \frac{k_B / c_V}{(\Delta T / T_0)^2} = \frac{k_B / c_V}{\epsilon^2}, \quad (6.4)$$

which is a strong function of the departure from equilibrium. In comparison, the LVDSMC results for this parameter do not depend on the departure from equilibrium as shown in Figure 6-3 which features simulation results for the average of two boundary cells. This illustrates a dramatic variance reduction compared to DSMC. Moreover, as  $N_{\text{ens}} N_C$  is directly related to the degree of computational effort, Figure 6-3 can be used as a measure of computational savings provided by the LVDSMC approach for problems with a small departure from equilibrium. A more direct measure needs to take into account the cost per sample for each method. Our experience indicates that, conservatively, LVDSMC computations are less than two times more expensive than DSMC for  $Kn \gtrsim 1$  and less than ten times more expensive for  $Kn = 0.1$ , for VHS simulations (assuming  $\Xi \approx 10$ ); this modest increase in computational expense is easily offset by the tremendous efficiency improvements indicated in Figure 6-3 for  $\epsilon \ll 1$ . We recall that the cost per time step of BGK-LVDSMC simulations is much smaller than comparable VHS-LVDSMC simulations.

### 6.3 Validation and demonstration cases

In this section, we present a variety of validation and demonstration cases treated using the LVDSMC method discussed in this thesis. For all simulations with  $Kn > 1$ , the boundary cancellation procedure (see discussion in Section 3.2) was used. While the simulations performed in this work (up to  $Kn = 10$ ) remained stable without boundary cancellation, the number of simulated particles per cell for  $Kn > 1$  tended to scale with  $\Xi Kn$  (rather than  $\Xi$ ) and the overall computational efficiency of the method was noticeably degraded. For  $Kn \leq 1$ , the boundary cancellation procedure is unnecessary, and was not used.

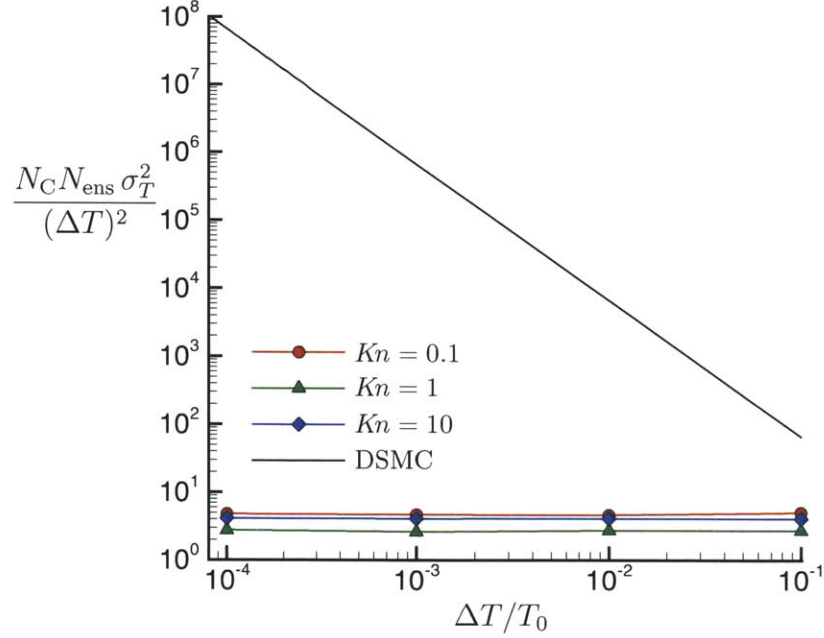


Figure 6-3: Variance in the cell-based temperature measurement for heat transfer between parallel plates, averaged between two cells adjacent to the wall. The LVDSMC results (symbols) are obtained from simulations, compared to the DSMC values (solid line) obtained from Equation (1.25).

### 6.3.1 Couette flow shear stress for the VHS collision model

In order to verify that the method correctly simulates the VHS collision operator, we simulated a steady state shear flow with boundary conditions  $u_{B,y}(0) = -U$  and  $u_{B,y}(L) = U$  with wall velocity  $U = 0.05c_0$ , and Knudsen number  $Kn = 0.05$  based on wall separation  $L$ . Simulations were performed for hard-sphere, helium, argon, and Maxwell molecules ( $\omega = 0.5, 0.66, 0.81, \text{ and } 1$ , respectively); excellent (better than 1%) agreement between LVDSMC and DSMC results for the shear stress is observed (see Figure 6-4).

### 6.3.2 Poiseuille and thermal creep flow in rectangular microchannels

Poiseuille (pressure driven) and thermal creep (surface temperature gradient driven) flows in microchannels are routinely analyzed in the context of Knudsen compressor

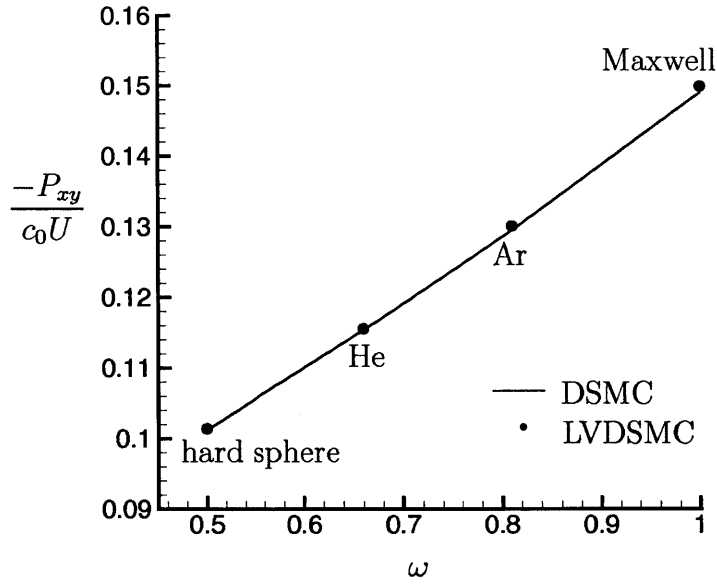


Figure 6-4: Validation of the LVDSMC VHS simulation method using a steady shear flow simulation at  $Kn = 0.05$ . Shear stress values for hard sphere, helium, argon, and Maxwell molecular gases are considered.

design, an important application of the present work which is discussed in more detail in Chapter 7. In this section, we use the high quality numerical results of Doi [24] for flow of a hard sphere gas through rectangular microchannels in order to validate the overall method in two-dimensional geometries, as well as to verify the correct implementation of the “effective body force” term (Section 3.3).

Here Poiseuille ( $\epsilon = \kappa_p L_x \ll 1$ ) and thermal creep ( $\epsilon = \kappa_T L_x \ll 1$ ) flows are simulated in the limit of small departure from equilibrium ( $\epsilon \ll 1$ ), where the Knudsen number  $Kn_x$  is based on the minimum channel dimension  $L_x$ . Due to two-fold symmetry, only a quarter of the channel cross-section was simulated. The results for the dimensionless flow rates are shown in Figures 6-5 and 6-6 for a wide range of Knudsen numbers and aspect ratios, where the overbar denotes a spatial average over the entire cross section. For most cases, a cell size of  $\Delta x/L_x = \Delta y/L_x = 0.02$  was used to obtain better than 1% agreement in the total mass flow rates compared to the results of Doi [24]. For some cases with  $Kn = 0.1$ , further refinement was required to obtain the same level of agreement; in those cases  $\Delta x/L_x = \Delta y/L_x = 0.01$  was

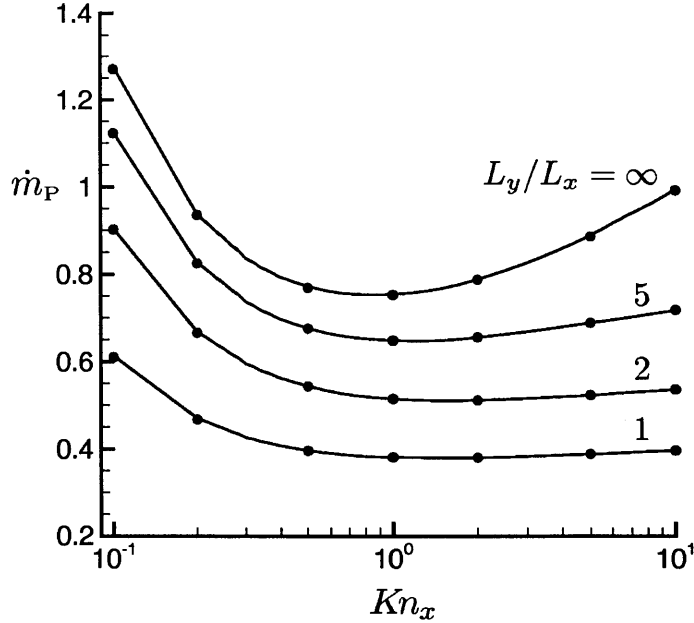


Figure 6-5: Flow rate for Poiseuille flow through a rectangular microchannel for various Knudsen numbers and aspect ratios. The LVDSMC results (symbols) are compared with data from Doi [24] (lines).

used.<sup>1</sup>

Also shown, in Figure 6-7, is the velocity field for Poiseuille flow through a square microchannel ( $L = L_x = L_y$ ) for  $Kn = 0.1$  using  $50 \times 50$  spatial cells. By performing steady-state averaging over  $10^6$  time steps ( $\Delta t = \Delta x/c_0$ ) after steady state was reached, this simulation resulted in a velocity field with a relative statistical uncertainty [28] of  $\sim 0.1\%$ . In order to obtain a  $0.1\%$  statistical uncertainty in  $\dot{m}_P$ ,  $5 \times 10^5$  time steps are required, using approximately 16 hours on a single core of an Intel 3.0 GHz Core 2 Quad processor. For square channels with  $Kn = 1$  and 10, with a  $25 \times 25$  cell mesh, 1.1 and 0.2 hours of computational time (respectively) were required, to achieve the same level of relative statistical uncertainty in  $\dot{m}_P$ . Given that even in variance-reduced guise, Monte Carlo approaches will always perform worse when *very* low noise is required, this performance is very encouraging for *highly resolved, two-dimensional* calculations.

<sup>1</sup>For thermal creep with  $Kn = 0.1$  and  $L_y/L_x = 2$ , Doi [24] reports a value of  $\dot{m}_T = 0.048$  compared to 0.0473 for the LVDSMC method. Due to the small number of digits in the reported value, it was not possible to determine if 1% agreement was attained for this specific case.

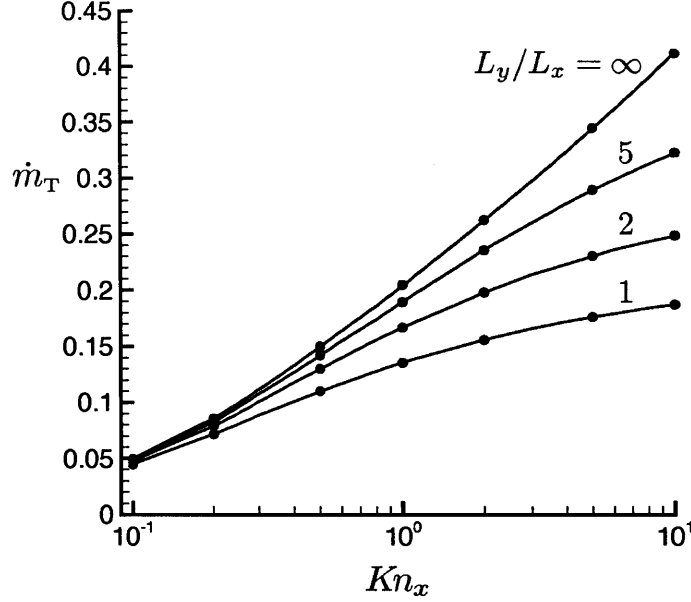


Figure 6-6: Flow rate for thermal creep flow through a rectangular microchannel for various Knudsen numbers and aspect ratios. The LVDSMC results (symbols) are compared with data from Doi [24] (lines).

As an indication of the relative efficiency compared to DSMC, the simulation time required to achieve 0.1% statistical uncertainty in the velocity field for Poiseuille flow through a square channel was determined. Assuming a Mach number of  $Ma \simeq 0.02$ , DSMC simulations would require approximately 500, 100, and 100 hours for  $Kn = 0.1, 1, 10$ , respectively, compared to 30, 4, and 2 hours for the LVDSMC simulations. For this problem (Poiseuille flow), DSMC simulates the pressure force as an equivalent gravitation force, which is a valid approach for small deviations from equilibrium (3.3). However, there is no obvious way to use DSMC to simulate thermal creep without resorting to very expensive three-dimensional simulations.

### 6.3.3 Lid-driven flow of argon gas

Next, simulations of two-dimensional lid-driven flow of argon ( $\omega = 0.81$ ) gas in a square enclosure with side length  $L$  are presented. The boundary conditions are diffusely reflecting walls, all of which are stationary except the top ( $y = L$ ) which is moving in the  $x$ -direction with velocity  $\epsilon c_0$ , where  $\epsilon \ll 1$ . Simulations were per-

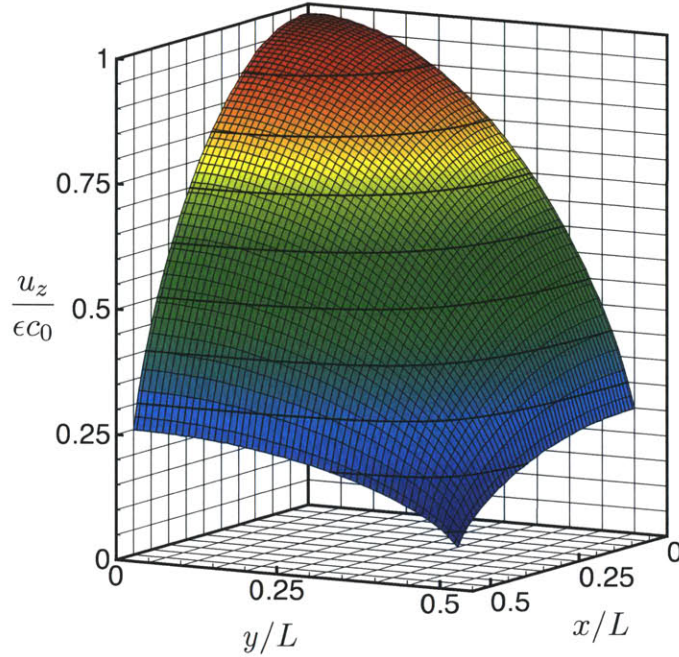


Figure 6-7: Streamwise velocity for Poiseuille flow through a square microchannel with  $Kn = 0.1$ .

formed for  $Kn = \lambda/L = 0.1, 1, \text{ and } 10$ ;  $100 \times 100$  cells were used for  $Kn = 0.1$ , while  $50 \times 50$  cells were used for  $Kn = 1, 10$ . Each simulation was repeated with a doubling of the number of cells in each coordinate direction (to  $200 \times 200$  and  $100 \times 100$ , respectively), which showed less than 1% difference in  $\rho$ ,  $u_x$ , and  $u_y$ ; this was taken as evidence of convergence. Shown in Figures 6-8–6-10 are the velocity and density fields corresponding to the finer-meshed solutions.

### 6.3.4 Response of a gas to a spatially-variable boundary temperature

The response of argon gas to a boundary temperature with a sinusoidal spatial variation was also simulated. Here, the lower boundary ( $y = 0$ ) is diffusely-reflecting with a temperature given by  $T_B = T_0(1 - \epsilon \cos 2\pi x/L)$ ; an identical boundary is located at  $y = L$ , and the Knudsen number based on the separation between the two boundaries ( $L$ ) is  $Kn = 1$ . Due to the underlying symmetries in the  $x$  and  $y$  directions, the

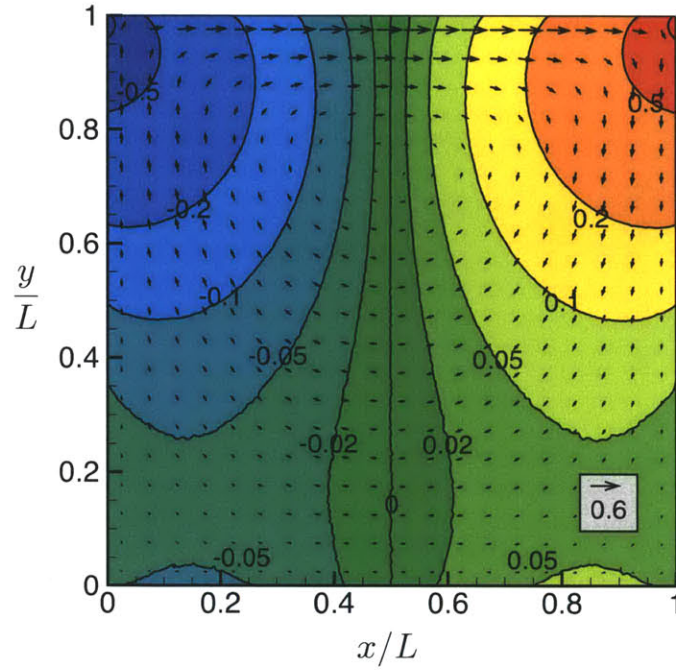


Figure 6-8: Lid-driven flow of argon gas at  $Kn = 0.1$ . The contour lines show the density  $\epsilon^{-1}(\rho/\rho_0 - 1)$ , while the velocity field  $\epsilon^{-1}\mathbf{u}/c_0$  is shown as a vector plot.

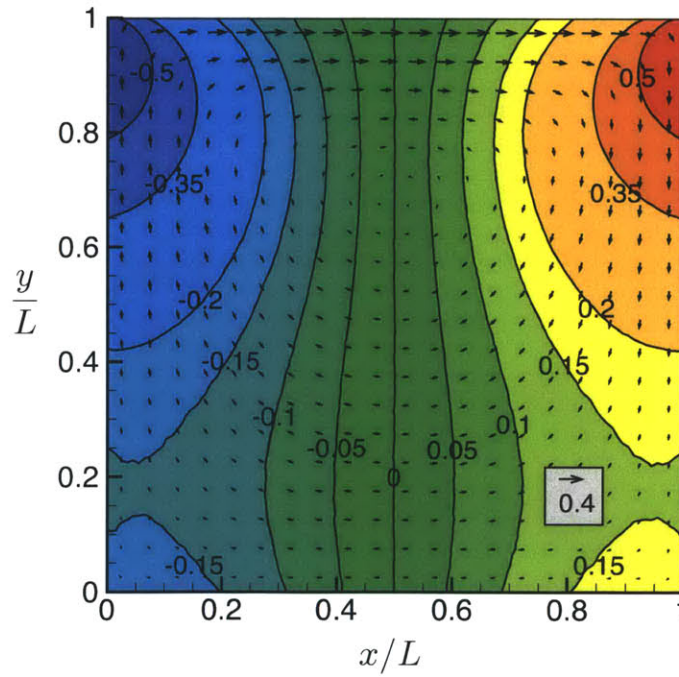


Figure 6-9: Lid-driven flow of argon gas at  $Kn = 1$ . The contour lines show the density  $\epsilon^{-1}(\rho/\rho_0 - 1)$ , while the velocity field  $\epsilon^{-1}\mathbf{u}/c_0$  is shown as a vector plot.

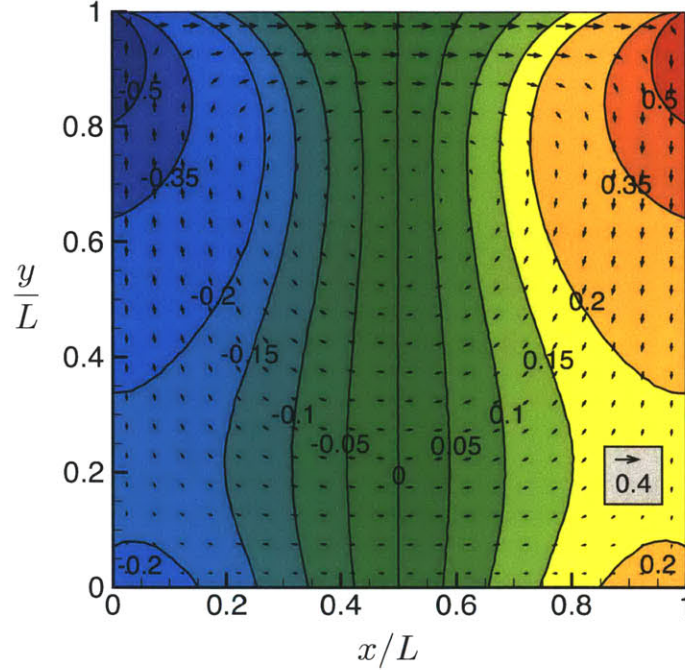


Figure 6-10: Lid-driven flow of argon gas at  $Kn = 10$ . The contour lines show the density  $\epsilon^{-1}(\rho/\rho_0 - 1)$ , while the velocity field  $\epsilon^{-1}\mathbf{u}/c_0$  is shown as a vector plot.

simulation domain was chosen as  $0 \leq x, y \leq L/2$ . Unlike the previous examples, here the results for several choices of  $\epsilon$  are shown. Figure 6-11 is a plot of the temperature and velocity fields for the limit of small departure from equilibrium  $\epsilon \ll 1$ . In Figures 6-12–6-13, the isotherms for the LVDSMC and DSMC methods are compared for  $\epsilon = 0.05$  and  $0.5$  respectively. For  $\epsilon = 0.05$ , there is no noticeable difference between the LVDSMC and DSMC temperature fields, even though the temperature field is noticeably perturbed from the  $\epsilon \rightarrow 0$  solution. The velocity field in the Figure 6-12 corresponds to the LVDSMC solution for  $\epsilon = 0.05$ ; the DSMC velocity field was considerably noisier. For  $\epsilon = 0.5$ , which is no longer a near-equilibrium case, there is only a slight discrepancy between the temperature fields obtained from LVDSMC and DSMC, likely due to the LVDSMC method being based on a linearized version of the collision operator (see Section 4.1).

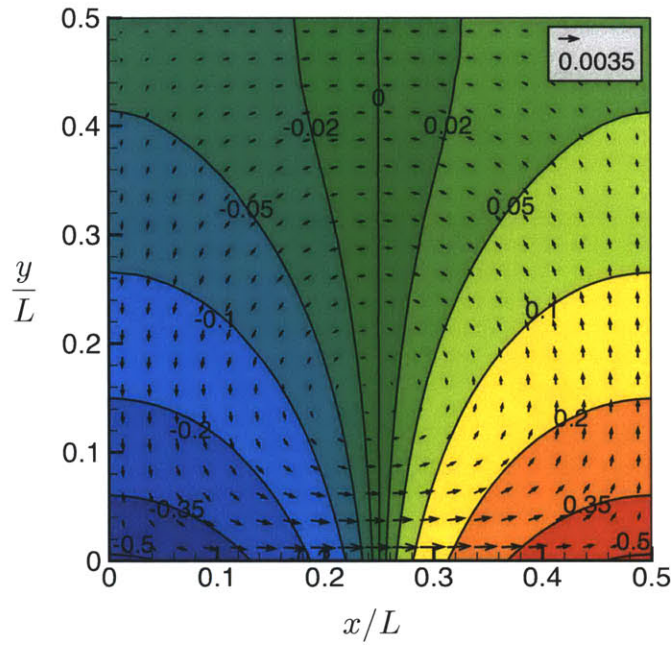


Figure 6-11: Response of argon gas to spatially-varying boundary temperature with  $Kn = 1$  and  $\epsilon \ll 1$ . The contour lines are isotherms (dimensionless temperature:  $\epsilon^{-1}(T/T_0 - 1)$ ), while the velocity field  $\epsilon^{-1}\mathbf{u}/c_0$  is shown as a vector plot.

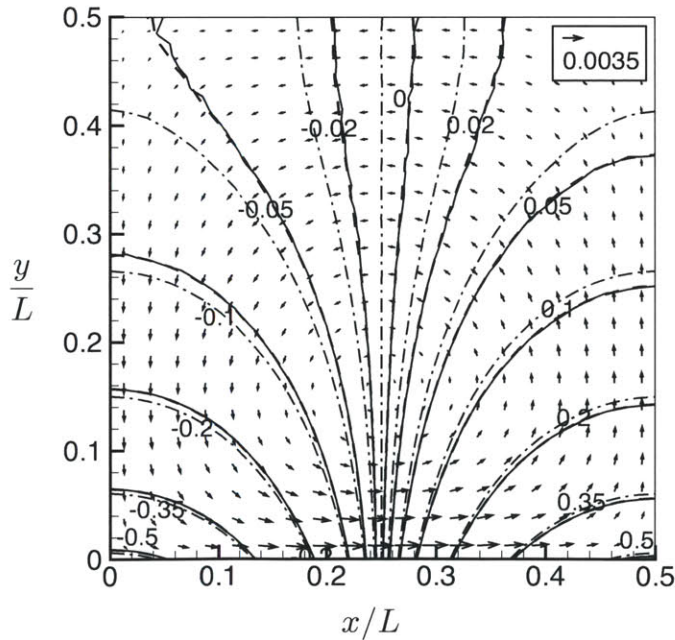


Figure 6-12: Response of argon gas to spatially-varying boundary temperature with  $Kn = 1$  and  $\epsilon = 0.05$ . Contour plot of the dimensionless temperature ( $\epsilon^{-1}(T/T_0 - 1)$ ) as obtained by LVDSMC (dashed) and DSMC (solid); the  $\epsilon \rightarrow 0$  limit (dash-dot) as obtained by LVDSMC is also shown for comparison. The velocity field  $\epsilon^{-1}\mathbf{u}/c_0$  is the LVDSMC solution for  $\epsilon = 0.05$ ; the DSMC velocity field was noticeably noisier.

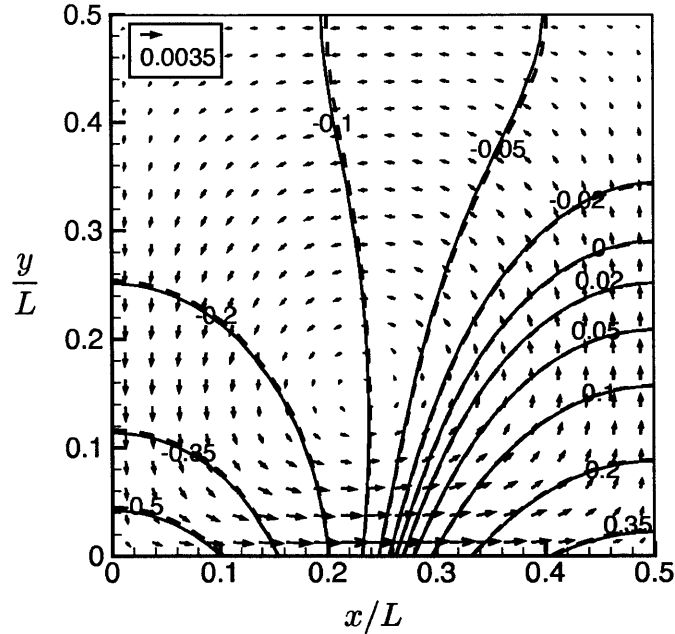


Figure 6-13: Response of argon gas to spatially-varying boundary temperature with  $Kn = 1$  and  $\epsilon = 0.5$ . Contour plot of the dimensionless temperature ( $\epsilon^{-1}(T/T_0 - 1)$ ) as obtained by LVDSMC (dashed) and DSMC (solid). The velocity field  $\epsilon^{-1}\mathbf{u}/c_0$  is the LVDSMC solution for  $\epsilon = 0.5$ .

### 6.3.5 BGK collision model simulations

As a test of the BGK collision algorithm developed in Chapter 5, two simple validation cases were performed. First, a one-dimensional Couette flow was simulated for a range of Knudsen numbers in the low Mach number limit. The resulting steady-state shear stress plotted in Figure 6-14 which shows excellent agreement with the numerical data reported by Loyalka [41]. Secondly, the transient response of a gas confined between parallel plates with accommodation coefficients  $\alpha = 0.7$  is considered, where the boundaries are impulsively heated from initial temperature  $T_0$  to  $1.5T_0$ . In Figure 6-15, the transient temperature response is compared to a DSMC simulation, again showing excellent results for all time steps.

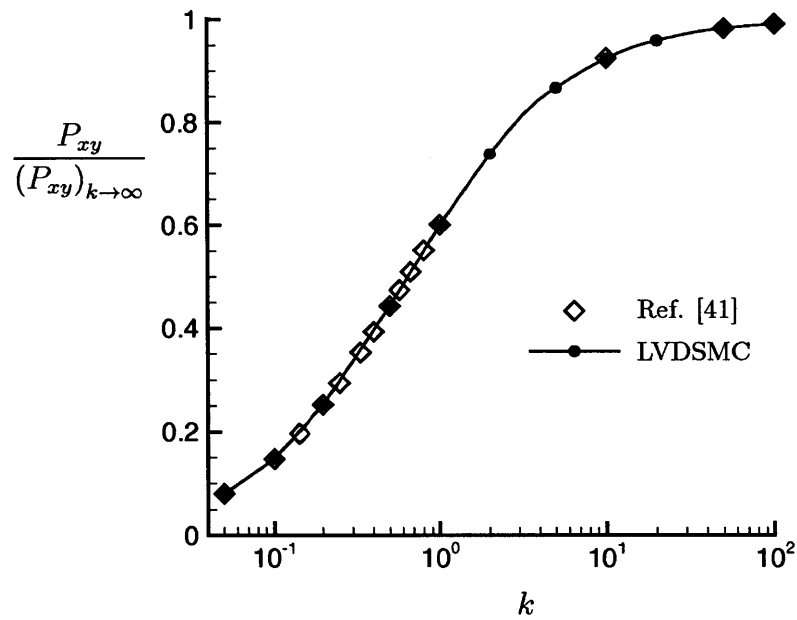


Figure 6-14: Validation of the LVDSMC simulation method for steady Couette flow of a BGK gas. The Knudsen numbers  $k = \frac{\sqrt{\pi}}{2}Kn$  are based on the separation width, and the shear stress is normalized by the free molecular flow limit  $(-P_{xy})_{k \rightarrow \infty} = \frac{1}{\sqrt{\pi}}c_0U$ , where the bounding walls have (tangential) velocities  $\pm U/2$ .

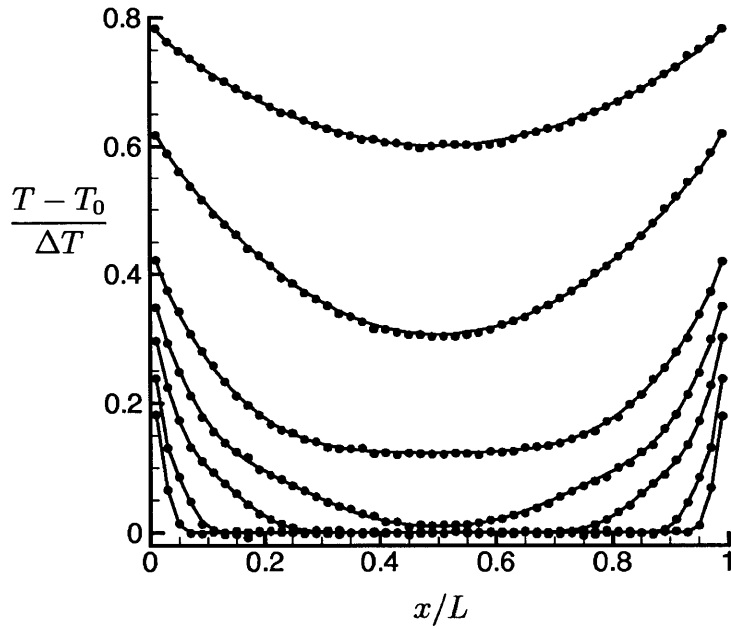


Figure 6-15: Validation of the LVDSMC simulation method for the transient temperature response of a BGK gas with Knudsen number  $k = \frac{\sqrt{\pi}}{2} Kn = 0.2$  and initial state  $(\rho_0, T_0)$ . Here, the LVDSMC (lines) and DSMC (symbols) results are shown for times  $c_0 t / L = \{0.02, 0.04, 0.1, 0.2, 0.4, 1, 2\}$ . The temperature is shown in dimensionless form, scaled by the characteristic temperature rise  $\Delta T = 0.5T_0$ .

# Chapter 7

## Selected Applications

In this chapter, two important applications of the LVDSMC methodology to problems of practical/scientific interest are presented. In both cases, substantial computational savings compared to DSMC are achieved. In the second case, namely the evaluation of the second-order temperature jump coefficient, these calculations are only possible using the LVDSMC (hence the absence of a rigorous calculation of the second-order temperature jump coefficient until now). Additional applications of the LVDSMC methodologies to phonon transport in the context of nanoscale solid-state heat transfer can be found in [49].

### 7.1 Simulation of Knudsen compressors

Knudsen compressors are devices with no moving parts, which exploit thermal transpiration effects in order to pump or pressurize a gas. These devices generally consist of many stages, each with a capillary section with a positive streamwise temperature gradient, followed by a connector section with a negative temperature gradient. The number of open design and optimization issues [46] still open have reinforced the need for computationally efficient simulation techniques. While actual Knudsen compressors feature relatively small temperature gradients, previous DSMC simulations [4, 58] have used artificially large temperature gradients in order to obtain a sufficiently noise-free results. Some researchers [4] have also resorted to using PDE based

solution approaches based on the BGK model; this is problematic because the BGK model has an incorrect Prandtl number (ratio of momentum diffusivity to thermal diffusivity), introducing significant error due to the coupling between the temperature and velocity fields.

In contrast, the present method is able to efficiently simulate arbitrarily small temperature gradients without resorting to approximations. LVDSMC, as developed in this thesis, is currently being used to investigate various design tradeoffs for Knudsen compressors [35], including the effect of various cross-sections for long channels and various design configurations for Knudsen compressors. An example of the later is shown in figure 7-1, where the thermal transpiration flow of a hard-sphere gas through a single section of periodic configuration ( $T(x, y) = T(x + 2L, y)$ , etc.) is simulated. The lower boundary is diffusely-reflecting with a temperature given by

$$\frac{T_B - T_0}{\Delta T} = \begin{cases} 2(x/L) - 1 & \text{for } x < L \\ 3 - 2(x/L) & \text{for } x > L \end{cases}, \quad (7.1)$$

while the upper boundary imposes a symmetry; the Knudsen number (based on  $L$ ) is  $Kn = 1$ . Another study [58] which simulated the same configuration used a dimensionless temperature difference of  $\Delta T/T_0 = 1/2$  in order to obtain reasonably smooth results using DSMC. In contrast, the method developed here is able to efficiently capture the  $\Delta T/T_0 \rightarrow 0$  limit with essentially zero statistical uncertainty.

## 7.2 Second order temperature jump

For gas flows with a characteristic length scale which is moderately larger than the mean free path (typically with  $Kn$  of order 0.1 or less), the Navier-Stokes description remains valid in the bulk of the flow field, but fails near the boundaries [57, 27]. This flow regime can be analyzed by solving the NS equations in combination with boundary conditions that allow for velocity slip and temperature jumps at the boundaries; the resulting solution is valid everywhere except in a layer of thickness  $\sim \lambda$  near the boundaries (known as the Knudsen layer) containing the region where kinetic effects

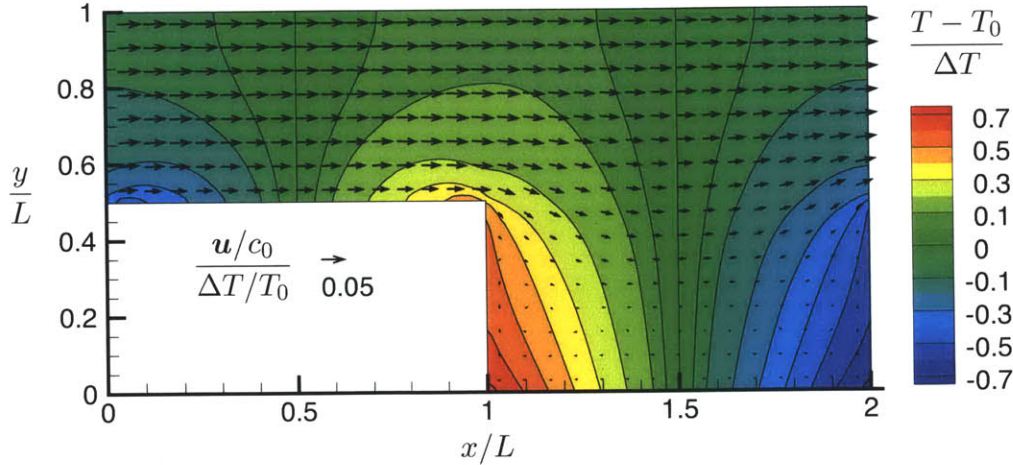


Figure 7-1: Simulation of a simple Knudsen compressor with  $Kn = 1$  and arbitrarily small temperature gradients. The arrows are velocity vectors and the contours are isothermal lines.

are important. This is a very important result, because it allows the use of a significantly simpler NS description and postpones the need for solving the considerably more expensive BTE.

Determination of slip coefficients requires high accuracy, which also implies low statistical uncertainty. Moreover, slip and jump coefficients have to be extracted from simulation data performed at low driving forces, in order to avoid non-linear or cross effects. This makes temperature jump calculations particularly challenging because the presence of temperature gradients (necessary for temperature jumps) implies density gradients, and in unsteady problems, flow velocities. Furthermore, at finite temperature differences, the temperature dependence of transport coefficients may alter the result. LVDSMC simulations are naturally suited to these problems; in fact, they make a solution of the specific problem considered here *possible for the first time*.

## 7.2.1 Theory

Velocity slip/temperature jump boundary condition models are generally based on an asymptotic solution [57] of the BTE. These solutions show that in the bulk, the

Navier-Stokes description is valid, while close to the boundary, kinetic effects become important (the Chapman Enskog distribution [59] cannot satisfy boundary conditions for the distribution function). These kinetic effects are accounted for using a kinetic inner solution. Slip/jump relations are obtained from matching this inner solution to the outer Navier-Stokes solution.

As an example, for a quiescent gas near a flat surface, the first-order temperature jump condition [57] resulting from this matching procedure is given by

$$\hat{T}(\hat{\mathbf{x}}_B) - \hat{T}_B = d_1 k \frac{d\hat{T}}{d\hat{n}}(\hat{\mathbf{x}}_B), \quad (7.2)$$

where  $k = \frac{\sqrt{\pi}}{2}Kn$ ,  $\hat{\mathbf{x}}_B = \mathbf{x}_B/L$  denotes the boundary location,  $n$  is the dimensionless (inward) normal direction,  $L$  is the system length scale, and the numerical constant  $d_1$  has non-adjustable values (reported in Reference [57]) of 2.4001 for a hard sphere gas and 1.30272 for a BGK gas; both values here correspond to diffusely-reflecting ( $\alpha = 1$ ) boundaries.

Although relation (7.2) is typically adequate for  $Kn \lesssim 0.1$  or less<sup>1</sup> the error becomes appreciable for  $Kn \gtrsim 0.1$ . Asymptotic expansion to second order in  $k$  shows that [57] the second-order temperature jump model takes the form

$$\hat{T}(\hat{\mathbf{x}}_B) - \hat{T}_B = d_1 k \frac{d\hat{T}}{d\hat{n}}(\hat{\mathbf{x}}_B) + d_2 k^2 \frac{d^2\hat{T}}{d^2\hat{n}}(\hat{\mathbf{x}}_B). \quad (7.3)$$

Calculation of slip coefficients is very challenging in general and becomes increasingly more challenging as the order of the expansion increases. For this reason,  $d_2$  is, in general, not known. It is only known in the special case of the BGK model for steady, linear flows [57], which in the present context imply that the temperature equation is of the form  $\nabla^2 T = 0$  (no unsteady or source terms). In this section we use the LVDSMC methodology to calculate  $d_2$  for the hard sphere gas for the first time and thus enable the use of Fourier's Law at higher  $Kn$  than before for a realistic gas model.

---

<sup>1</sup>The usefulness of first-order slip/jump models primarily depends on the amount of error that can be tolerated. However, temperature jump coefficients (both first-order and the second-order measured here) are larger than the velocity slip counterparts. As a result, the second-order temperature jump correction becomes important at smaller Knudsen numbers.

We will achieve this objective using a problem for which the NS/Fourier solution based on (7.3) can be analytically written down. By comparing this solution to LVDSMC results, we can extract the value of  $d_2$ . The problem we have chosen is that of a gas layer subject to internal heat generation.

In dimensionless form, the one-dimensional heat equation with internal heat generation can be written as

$$-\frac{4}{5}\gamma_2 \frac{d^2\hat{T}}{d\hat{x}^2} = \epsilon, \quad (7.4)$$

where  $\gamma_2$  is a dimensionless form of the thermal conductivity, which is equal to [57] 1.9228 for hard spheres and unity for BGK. The departure from equilibrium in this case is the dimensionless version of the volumetric internal heat generation  $\dot{Q}$

$$\epsilon = \frac{L\dot{Q}}{c_0 P_0} \ll 1. \quad (7.5)$$

For a gas in contact with two boundaries with temperatures  $T_B(\pm L/2) = T_0$ , the solution to Equation (7.5) subject to boundary conditions (7.3) gives the desired second order temperature jump solution

$$\hat{T} = \frac{1}{2} \frac{4\epsilon}{5\gamma_2} \left[ \left( \frac{1}{4} - \hat{x}^2 \right) + d_1 k - 2d_2 k^2 \right]. \quad (7.6)$$

## 7.2.2 Implementation

An essential step in simulating the kinetic version of the above problem is introducing an internal heat generation term in the LVDSMC simulation methodology. As was done for pressure and temperature gradient driven flows, this can be introduced using the “effective body force” approach of section 3.3, by generating deviational particles corresponding to an internal energy change of the equilibrium state, given by

$$\left[ \frac{\partial f^d(\mathbf{c})}{\partial t} \right]_{\text{H}} = \left[ \frac{\partial f^{\text{eq}}(\mathbf{c})}{\partial t} \right]_{\text{H}} = \epsilon \frac{c_0}{L} \left( \frac{2}{3} \frac{\|\mathbf{c} - \mathbf{u}_0\|^2}{c_0^2} - 1 \right) f^0(\mathbf{c}). \quad (7.7)$$

The relation between specific internal energy  $\frac{3}{2}RT$  and volumetric heat generation

$$\dot{Q} = \rho_0 \frac{d}{dt} \left( \frac{3}{2} RT \right) \quad (7.8)$$

was used to produce the above result. As this application involves modeling heat transfer through a quiescent gas, the choice of  $\mathbf{u}_0 = \mathbf{0}$  is appropriate.

Multiplying the above expression by the total simulation volume  $V$ , time step  $\Delta t_{\text{body}}$ , and differential element in velocity space  $d^3\mathbf{c}$  gives the total change in deviantial particles due to heat generation for velocities within  $d^3\mathbf{c}$  per time step

$$\begin{aligned} \left[ \frac{\partial f^d(\mathbf{c})}{\partial t} \right]_{\text{H}} V \Delta t_{\text{body}} d^3\mathbf{c} &= \epsilon \frac{c_0}{L} \left( \frac{2}{3} \xi^2 - 1 \right) f^0(\mathbf{c}) V \Delta t_{\text{body}} d^3\mathbf{c} \\ &= \epsilon \frac{\rho_0 c_0}{L} F^{\text{H}}(\mathbf{c}) V \Delta t_{\text{body}} d^3\xi, \end{aligned} \quad (7.9)$$

where  $\xi = \mathbf{c}/c_0$  and

$$F^{\text{H}}(\mathbf{c}) = \frac{c_0^3}{\rho_0} \left( \frac{2}{3} \xi^2 - 1 \right) f^0(\mathbf{c}). \quad (7.10)$$

This term was sampled using the ratio-of-uniforms method as was done for the standard “body force” terms (see sections 3.2, 3.3, and A.3.1), resulting in sampling bounds

$$0 \leq H \leq a^{\text{H}} = \frac{1}{\pi^{3/5}} \left( \frac{2}{3e} + 1 \right)^{2/5} \quad (7.11)$$

$$-b^{\text{H}} \leq \eta_x, \eta_y, \eta_z \leq b^{\text{H}} = \frac{1}{\pi^{3/10}} \left[ \frac{2}{3} \left( \frac{7}{2e} \right)^{7/2} + \left( \frac{5}{2e} \right)^{5/2} \right]^{1/5}, \quad (7.12)$$

and total number of trial samples

$$\begin{aligned}
& \frac{1}{mW_{\text{eff}}} \int_{\mathcal{R}^3} d^3\mathbf{c} \left| \left[ \frac{\partial f^d(\mathbf{c})}{\partial t} \right]_{\text{H}} V \Delta t_{\text{body}} \right| \\
&= \frac{\rho_0 c_0 V \Delta t_{\text{body}}}{mW_{\text{eff}} L} \int_{\mathcal{R}^3} d^3\xi |F^{\text{H}}(\mathbf{c})| \\
&= \frac{\rho_0 c_0 V \Delta t_{\text{body}}}{mW_{\text{eff}} L} \int_{\mathcal{R}^3} d^3\boldsymbol{\eta} \left| \frac{\partial (|F^{\text{H}}(\mathbf{c})|, \boldsymbol{\xi})}{\partial (H, \boldsymbol{\eta})} \right| H(\boldsymbol{\eta}) \\
&< \frac{\rho_0 c_0 V \Delta t_{\text{body}}}{mW_{\text{eff}} L} \int_{-b^{\text{H}}}^{b^{\text{H}}} d\eta_x \int_{-b^{\text{H}}}^{b^{\text{H}}} d\eta_y \int_{-b^{\text{H}}}^{b^{\text{H}}} d\eta_z \frac{5}{2} a^{\text{H}} \\
&= 20 \frac{\rho_0 c_0 V \Delta t_{\text{body}}}{mW_{\text{eff}} L} a^{\text{H}} (b^{\text{F}})^3 = N_{\text{H}}^{\text{trial}}. \tag{7.13}
\end{aligned}$$

For the heat generation substep (which takes the place of the ordinary body force substep), a sample  $(H, \boldsymbol{\eta})$  is generated (uniformly) utilizing bounds (7.11–7.12) for each trial step. Using  $\mathbf{c} = c_0 \boldsymbol{\eta} / \sqrt{H}$ ,  $F^{\text{H}}$  is evaluated from Equation (7.10), and the trial particle generation is accepted if  $H < |F^{\text{H}}(\mathbf{c})|^{2/5}$ . Accepted particles are added to the simulation with sign  $\text{sgn}[F^{\text{H}}(\mathbf{c})]$  and with a position  $\mathbf{x}$  sampled uniformly from  $\mathcal{D}$ . As before, mass conservation is enforced using a stratified sampling approach (see section 3.2.2).

The original implementation using  $f^{\text{eq}} = f^0$  suffered from unusual variability, which made the resolution of the temperature field to the desired accuracy difficult. This is thought to be a result of the fact that the heat generation term (7.7) introduces a net energy into the simulation (unlike the pressure- and temperature-gradient driven body forces previously considered in Section 3.3) and the fact that calculations had to be run for  $Kn < 0.1$ , for which particle methods are typically inefficient. For this reason, algorithms using a spatially-variable equilibrium  $f^{\text{MB}}$ , were used (see Appendix B). As discussed in Chapter 2, these implementations take advantage of the presence of a local description ( $f \rightarrow f^{\text{loc}}$ ) as  $Kn \rightarrow 0$  to substantially reduce the number of particles required in that limit (or achieve higher accuracy for the same number of particles).

For the hard sphere operator, a specialized implementation based on a spatially-

variable equilibrium  $f^{\text{MB}}$ , which remained unchanged through the simulation was used. In other words, an initial run was performed in order to determine the approximate density and temperature fields, which were then used to define the equilibrium state of the subsequent calculation. The resulting temperature field from this approach was found to give sufficiently repeatable data to produce a good fit to the model for the second order jump coefficient. It is noted that this approach is not herein proposed as a method for solving general problems. The method outlined in Chapters 3–5 is efficient and well-behaved in all simulations performed in this thesis *except* those involving heat generation; the exact reason for the ill behavior of the heat generation term remains an open issue (see discussion in Chapter 8).

For the BGK operator, an implementation of a previously published method [52] described in Section 2.3 was modified to include the heat generation step. Because this method simulates a local equilibrium  $f^{\text{MB}}$  that is updated in the course of the simulation, the heat generation term can be introduced directly (and analytically) into  $f^{\text{MB}}$ , using (see Equation (7.8))

$$\dot{Q} = \rho_0 \frac{d}{dt} \left( \frac{3}{2} RT_{\text{MB}} \right). \quad (7.14)$$

Thus, implementing volumetric heating involves simply incrementing  $T_{\text{MB},j}$  by a fixed amount in each cell  $j$

$$\Delta T_{\text{MB},j} = \frac{2}{3} \frac{\epsilon c_0 T_0}{L} \Delta t_{\text{body}}. \quad (7.15)$$

### 7.2.3 Results

Numerical simulations of the uniform heat generation problem were performed in order to extract the second-order jump coefficients by comparing the calculated steady centerline temperature  $\hat{T}(\hat{x} = 0)$  with Equation (7.6). According to this relation,  $d_2$  can be extracted from the slope of

$$\frac{5\gamma_2}{4\epsilon k} \hat{T}(\hat{x} = 0) - \frac{1}{8k} - \frac{d_1}{2} \quad (7.16)$$

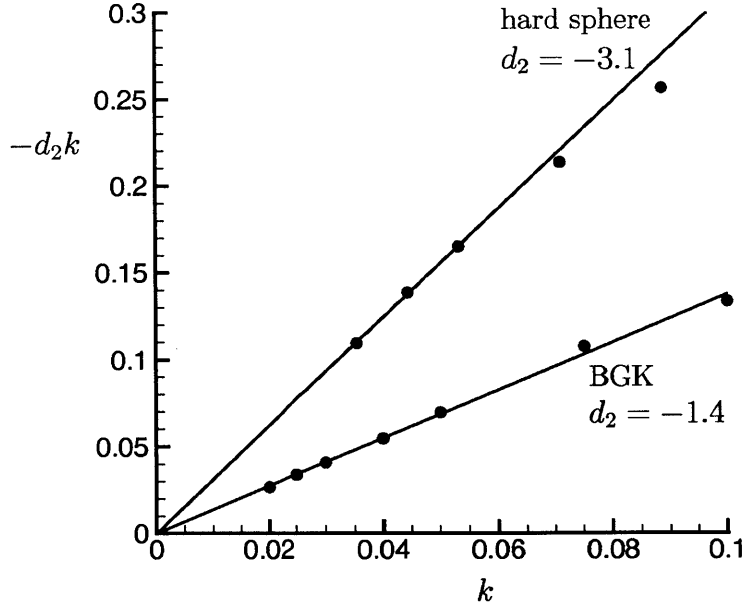


Figure 7-2: Fits used to extract the second-order jump coefficient  $d_2$  for the hard sphere and BGK collision models.

as a function of  $k$ . Figure 7-2, shows our numerical data for  $-kd_2$  and a linear least squares fit passing through the origin based on the data for  $k < 0.06$ , and the values  $d_1 = 1.30272$  for BGK and  $d_1 = 2.4001$  for the hard sphere gas [57]. Our results are  $d_2 = -1.4$  for BGK and  $-3.1$  for the hard sphere model; the very good fit proves that the leading order term is indeed  $k^2$ . To our knowledge, these are the first measurements of  $d_2$  for the more general case that includes a source term in the temperature equation and the first ever measurement of the hard sphere coefficient.

Figure 7-3 shows the temperature field for the hard sphere case with  $Kn = 0.05$  (equivalent to  $k = 0.044311$ ) using the value obtained above (namely  $d_2 = -3.1$ ) demonstrating excellent agreement everywhere except in the Knudsen layer in the boundary, as expected. By comparing the first- and second-order jump theories, it is clear that the second-order jump theory provides a significant improvement over the existing first-order theory, already at  $Kn = 0.05$ . For  $Kn = 0.1$  (Figure 7-4), the Knudsen layers are just beginning to merge in the center of the simulation, leading to a slight error in the second-order fit at  $\hat{x} = 0$  and a large discrepancy in the first-order fit.

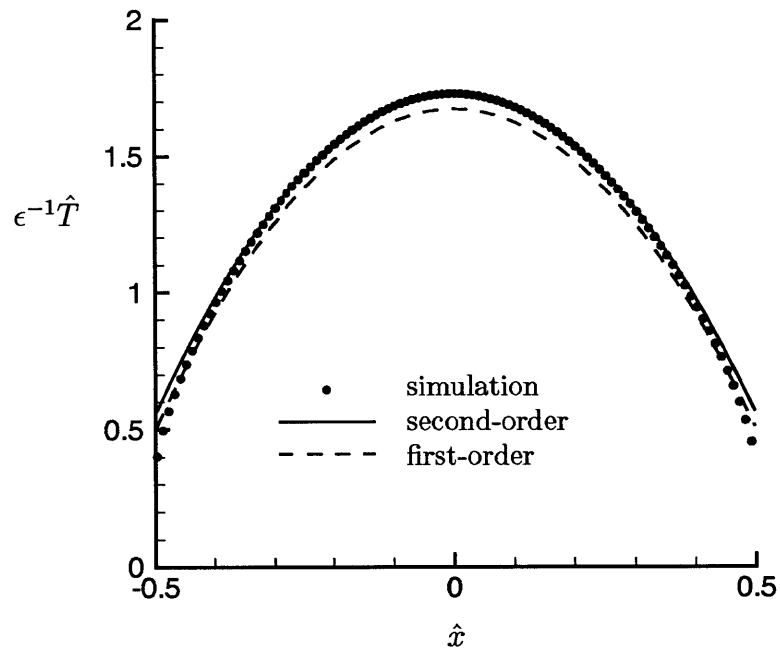


Figure 7-3: Second-order temperature jump solution (Equation (7.6)) to the uniform heat generation problem with Knudsen number  $Kn = 0.05$ , where the simulation results (symbols) are compared to the first- (dashed line) and second-order (solid line) jump theories.

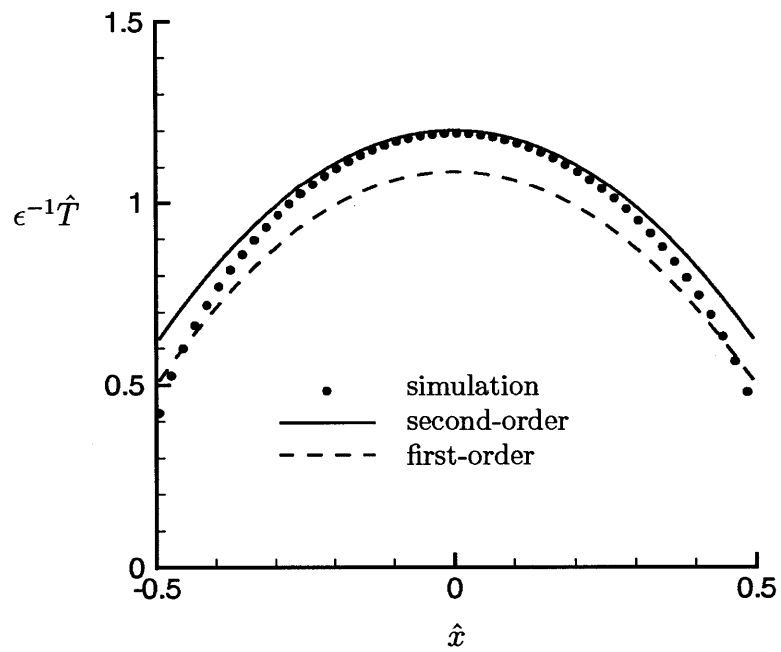


Figure 7-4: Second-order temperature jump solution (Equation (7.6)) to the uniform heat generation problem with Knudsen number  $Kn = 0.1$ , where the simulation results (symbols) are compared to the first- (dashed line) and second-order (solid line) jump theories.



# Chapter 8

## Conclusion

In this thesis, an advanced stochastic particle simulation method has been developed for simulating kinetic gas flows in micro- and nanoscale devices. This method, like previous variance-reduced simulation approaches, dramatically outperforms the prevalent DSMC method in near-equilibrium flow regimes; it also offers several important extensions and improvements over previous variance-reduced methods.

In particular, the present method simulates the more general VHS collision operator, which more accurately represents the viscosity law for real gases; previous particle methods incorporating variance-reduction were limited to the hard-sphere [22, 11, 33, 2] and BGK models [52, 56, 29, 39]. Efficient simulation of the VHS collision operator within the LVDSMC framework required the implementation of more complex algorithms for the collision step. By simulating collisions as a series of Markov creation and deletion events [61], the resulting method avoids intrinsic time step error within the collision step. A highly-efficient advection routine [52, 53] based on the ratio-of-uniforms sampling approach was also developed. Moreover, by enforcing mass conservation within each step, the present method provides a significant improvement, allowing accurate simulation with as few as ten particles or less per cell [53], which is in stark contrast to the hundreds to thousands per cell required for previous LVDSMC simulation methods. This result is important as it can drastically reduce the amount of memory used for larger simulations as well as permitting much more efficient computation for steady state problems.

This research focused on simulating the deviation from a fixed equilibrium distribution because simulating deviation from a spatially-variable equilibrium distributions using the algorithms described in this thesis is less efficient in multiple spatial dimensions for a wide range of Knudsen numbers. The primary reason for this is the complexity associated with the generation of particles at cell boundaries due to the discontinuities of the equilibrium distribution there and the rapid increase in the number of cell interfaces with problem dimension. Moreover, the added complications induced by the VHS Markov-based collision algorithms, as well as the mass conservation enforcement, made the full implementation of a simulation based on a variable equilibrium unnecessarily complicated. However, as the later approach provides a significant advantage for resolving the continuum limit [55], future development of such a technique may be warranted; perhaps the optimal approach would involve a continuously-distributed equilibrium where the additional particle generation in the advection step would be performed volumetrically, rather than concentrated at the cell interfaces.

Additional directions for future research include rigorous convergence studies, in order to accurately quantify the convergence rate, as has been done for the DSMC method [51], and the extension of LVDSMC to other gas models—most importantly, polyatomic gas models, which would involve developing an analogue to the widely-used Larsen-Borgnakke procedure [15]. As variance-reduced simulation of polyatomic molecules is likely to be a difficult undertaking, perhaps an initial step would be simulate the recently-developed polyatomic versions of the ES-BGK collision model [6], which is significantly less complex than VHS. Theoretically, it would be trivial to extend the LVDSMC methodology for multi-species transport; and this, combined with successful implementation of polyatomic molecular models would provide a framework for developing chemical reaction procedures.

In this thesis numerous validations were performed, demonstrating the overall accuracy and efficiency of the method. Two useful applications from active research areas in nanotechnology were presented. In both cases, the desired problem could be accurately and efficiently simulated using the LVDSMC simulation approach, al-

though for the second application which required simulation of a uniform heat generation term, the method required simulation of a spatially-variable equilibrium in order to prevent random walks in the temperature field. As this issue only presented with the simulation of internal heat generation, which was implemented via a special “effective body force term,” and was not noticed for the large number of other simulation configurations including “body force” terms for pressure and temperature gradient driven flows, it seems certain that the problem lies with the heat generation term and not the method in general. However, further research may be necessary in order to understand the cause of this apparent pathology.

As simulations performed using previous LVDSMC methods have already contributed to published research [44, 45], this method is also expected to become a useful computational tool for use in the wider scientific and engineering community. Moreover, due to its robustness and wide generality, it is hoped that the method will be used alongside DSMC simulations, fulfilling a complementary role by simulating problems with small departures from equilibrium, where DSMC methods are extraordinarily inefficient.

Another development based on the BGK collision model is the extension of the LVDSMC methodology to treat phonon transport in nanoscale heat transfer applications [49]. The phonon distribution (density of states times the occupation number) satisfies a similar BTE as molecular gas transport, only with a different equilibrium distribution (the equilibrium phonon occupation number follows Bose-Einstein statistics) [21]. Phonon collisions are treated using the BGK model, where it is known as the relaxation-time approximation, only with frequency dependent relaxation times. In phonon simulations, energy conservation is critical to avoid random walks in the temperature and heat flux. In Reference [49], this was accomplished by solving the Boltzmann equation in terms of the energy density rather than particle density, enabling efficient simulation of solid-state heat transfer for semiconductor devices with small temperature gradients which drastically outperform traditional Monte Carlo (DSMC-like) simulations.

The LVDSMC simulation approach for molecular gas, phonon, and other forms

of particle mediated transport, can be also thought of as a new class of multiscale simulation approaches [53] which are based on a decomposition of the kinetic description into a equilibrium part which is described deterministically, and the remainder which is described using a particle simulation method. Such a decomposition based on global equilibrium  $f^0$  (the focus of this thesis) leads to substantial computational gains in the limit of small departure from equilibrium, while decompositions based on a local equilibrium  $f^{\text{MB}}$ , leads to a dynamically and automatically adaptive multiscale method that seamlessly bridges the two descriptions (namely, equilibrium and kinetic) without introducing any approximation.

# Appendix A

## Particle Sampling Methods

This section outlines the basic particle sampling techniques used to sample the various distributions used in the algorithms discussed in this thesis. Each of these sampling techniques requires a high quality random number generator [50] which produces samples  $\mathfrak{R}$  which are uniformly distributed on  $[0, 1)$ .

### A.1 Direct inversion of the cumulative distribution function

A random sample from any probability distribution  $p(\xi)$  can be generated by setting the cumulative distribution function equal to a uniformly distributed random variable

$$\int_{-\infty}^{\xi} d\zeta p(\zeta) = \mathfrak{R} \tag{A.1}$$

and solving for  $\xi$ . Note, that the above procedure is only valid when  $p(\xi)$  is a probability distribution, requiring that  $p(\xi)$  is nonnegative and properly normalized, i.e.

$$\int_{-\infty}^{\infty} d\xi p(\xi) = 1. \tag{A.2}$$

Several examples follow in the subsections below.

### A.1.1 Sampling from an exponential distribution

For the exponential distribution  $p(\xi) = e^{-\xi}$ ,  $\xi \in (0, \infty)$ , the above procedure is trivial, resulting in the production of a sample  $\xi = -\ln(\mathfrak{R})$  from the random number  $\mathfrak{R}$ .

### A.1.2 Sampling from a Gaussian distribution

For a Gaussian distribution of the form  $p(\xi) = \frac{1}{\sqrt{\pi}}e^{-\xi^2}$ ,  $\xi \in \mathcal{R}$ , direct inversion of the cumulative distribution can be performed for a joint distribution of two independent Gaussian variables  $p(\xi_1, \xi_2) = \frac{1}{\pi}e^{-(\xi_1^2 + \xi_2^2)}$ , where the integration is performed by converting to polar coordinates—a technique known as the Box Muller method.

$$\xi_1 = \cos(2\pi\mathfrak{R}_1)\sqrt{-\ln(\mathfrak{R}_2)} \quad (\text{A.3})$$

$$\xi_2 = \sin(2\pi\mathfrak{R}_1)\sqrt{-\ln(\mathfrak{R}_2)} \quad (\text{A.4})$$

A faster version of the above procedure, which avoids the evaluation of the trigonometric functions is the more commonly used polar form of the Box Muller method which can be found in Reference [50].

Samples from the equilibrium distribution  $f^0(\mathbf{c})$  (equation (2.2)) are obtained as  $\mathbf{c} = \mathbf{u}_0 + c_0\boldsymbol{\xi}$ , where each (independent) component of  $\boldsymbol{\xi}$  is obtained from the above procedure.

### A.1.3 Sampling from a biased Gaussian distribution

Sampling from an equilibrium fluxal distribution (e.g. distribution (3.7)) of the form  $p(\xi_1, \xi_2, \xi_3) = \frac{2\xi_1}{\pi}e^{-(\xi_1^2 + \xi_2^2 + \xi_3^2)}$ , where  $\xi_1 \in [0, \infty)$  and  $\xi_2, \xi_3 \in \mathcal{R}$  can be obtained from the Box Muller technique in the section above for  $\xi_2$  and  $\xi_3$ , while the remaining variable  $\xi_1$  is easily sampled by inverting the cumulative distribution, resulting in  $\xi_1 = \sqrt{-\ln(\mathfrak{R})}$ .

### A.1.4 Sampling uniformly from a unit sphere

Producing samples from a uniform unit sphere is another procedure which is based on inversion of the cumulative distribution function. Straightforward analysis leads to the following expressions for the components of a unit vector on the unit sphere

$$\Omega_1 = \chi \cos(\theta) \tag{A.5}$$

$$\Omega_2 = \chi \sin(\theta) \tag{A.6}$$

$$\Omega_3 = \sqrt{1 - \chi^2} \tag{A.7}$$

where  $\chi = 2\mathfrak{R}_1 - 1$  and  $\theta = 2\pi\mathfrak{R}_2$  and  $\mathfrak{R}_1$  and  $\mathfrak{R}_2$  are uniformly distributed random variables.

## A.2 The acceptance-rejection method

The acceptance-rejection method is a basic technique for producing samples from a distribution  $p(\xi)$  which has a known bound  $p(\xi) \leq p_{\max}$ . First, a trial sample  $\xi$  uniformly distributed in the domain of  $p$  is generated, and accepted with probability  $p(\xi)/p_{\max}$ . If the trial sample is rejected, the procedure is simply repeated until an accepted sample is obtained. This method can be extremely inefficient when the probability is concentrated on a certain region because of the large number of rejections.

## A.3 The ratio-of-uniforms method

The ratio-of-uniforms method is an alternative sampling approach which is often drastically more efficient for generating samples from a distribution than the acceptance-rejection method. This method was used primarily to sample a deviational distribution which is represented as a product of a polynomial and a Gaussian in three dimensions; it was also used to develop a simple generation routine for a probability

Table A.1: Ratio of uniforms bounds

$i$	$F^i(\boldsymbol{\xi})$	$\pi^{3/2} (a^i)^{5/2}$	$\pi^{3/2} (b_1^i)^5$	$\pi^{3/2} (b_2^i)^5$	$\pi^{3/2} (b_3^i)^5$
1	$\pi^{-3/2} e^{-\xi^2}$	1	$[5/(2e)]^{5/2}$	$[5/(2e)]^{5/2}$	$[5/(2e)]^{5/2}$
2	$\pi^{-3/2} \xi_1 e^{-\xi^2}$	$1/\sqrt{2e}$	$(3/e)^3$	$5^{5/2}/(2e)^3$	$5^{5/2}/(2e)^3$
3	$\pi^{-3/2} \xi_1^2 e^{-\xi^2}$	$1/e$	$[7/(2e)]^{7/2}$	$(5/2)^{5/2} e^{-7/2}$	$(5/2)^{5/2} e^{-7/2}$
4	$\pi^{-3/2} \xi_1 \xi_2 e^{-\xi^2}$	$1/(2e)$	$27e^{-7/2}/\sqrt{2}$	$27e^{-7/2}/\sqrt{2}$	$5^{5/2}/(2e)^{7/2}$
5	$\pi^{-3/2} \xi^2 e^{-\xi^2}$	$1/e$	$[7/(2e)]^{7/2}$	$[7/(2e)]^{7/2}$	$[7/(2e)]^{7/2}$
6	$\pi^{-3/2} \xi_1 \xi^2 e^{-\xi^2}$	$[3/(2e)]^{3/2}$	$(4/e)^4$	$20^{5/2}/(27e^4)$	$20^{5/2}/(27e^4)$

distribution in a single dimension: both are discussed below.

### A.3.1 Ratio-of-uniforms sampling of a product of a polynomial and a Gaussian

Here the multivariate approach of Wakefield [62] is reviewed and modified to sample the deviational distribution

$$F(\boldsymbol{\xi}) = \sum_{i=1}^6 p_i F^i(\boldsymbol{\xi}), \quad (\text{A.8})$$

where the  $F^i$  are shown in table A.1 and  $\boldsymbol{\xi} \in \mathcal{R}^3$ ; note, that these functions are not true probability distributions because they are neither nonnegative nor normalized.

As a first step, the ratio-of-uniforms is applied to a single deviational distribution  $F^i(\boldsymbol{\xi})$  via the variable transformation [62]

$$\boldsymbol{\xi} = \boldsymbol{\eta}/H^r \quad (\text{A.9})$$

$$|F_i| = H^{1+3r}, \quad (\text{A.10})$$

where the parameter  $r$  can be chosen to maximize the acceptance probability. Since  $r = 1/2$  results in optimal efficiency for sampling a pure Gaussian [62], this value was

adopted for all cases, yielding:

$$\boldsymbol{\xi} = \boldsymbol{\eta}/\sqrt{H} \quad (\text{A.11})$$

$$|F_i| = H^{5/2}. \quad (\text{A.12})$$

An important advantage of this formulation is that the transformed variables are all bounded quantities; in this case ( $\boldsymbol{\xi} \in \mathcal{R}^3$ ), ratio-of uniforms variables are bounded quantities

$$0 \leq H \leq a^i \quad (\text{A.13})$$

$$- \leq b_1^i \leq \eta_1 \leq b_1^i \quad (\text{A.14})$$

$$- \leq b_2^i \leq \eta_2 \leq b_2^i \quad (\text{A.15})$$

$$- \leq b_3^i \leq \eta_3 \leq b_3^i, \quad (\text{A.16})$$

where the bounds are evaluated according to [62]

$$a^i = \sup_{\boldsymbol{\xi} \in \mathcal{R}^3} |F^i|^{2/5} \quad (\text{A.17})$$

$$b_1^i = \sup_{\boldsymbol{\xi} \in \mathcal{R}^3} |\xi_1| |F^i|^{1/5} \quad (\text{A.18})$$

$$b_2^i = \sup_{\boldsymbol{\xi} \in \mathcal{R}^3} |\xi_2| |F^i|^{1/5} \quad (\text{A.19})$$

$$b_3^i = \sup_{\boldsymbol{\xi} \in \mathcal{R}^3} |\xi_3| |F^i|^{1/5}, \quad (\text{A.20})$$

for which the calculated results are given in table A.1.

Next, the bounds for the overall deviational distribution (A.8)

$$0 \leq H \leq a \quad (\text{A.21})$$

$$- \leq b_1 \leq \eta_1 \leq b_1 \quad (\text{A.22})$$

$$- \leq b_2 \leq \eta_2 \leq b_2 \quad (\text{A.23})$$

$$- \leq b_3 \leq \eta_3 \leq b_3 \quad (\text{A.24})$$

are calculated; shown below is the full calculation for the bound  $a$ .

$$\begin{aligned} \sup_{\xi \in \mathcal{R}^3} |F|^{2/5} &= \left[ \sup_{\xi \in \mathcal{R}^3} |F| \right]^{2/5} = \left[ \sup_{\xi \in \mathcal{R}^3} \left| \sum_{i=1}^6 p_i F^i \right| \right]^{2/5} \leq \left[ \sum_{i=1}^6 |p_i| \sup_{\xi \in \mathcal{R}^3} |F^i| \right]^{2/5} \\ &= \left[ \sum_{i=1}^6 |p_i| \left( \sup_{\xi \in \mathcal{R}^3} |F^i|^{2/5} \right)^{5/2} \right]^{2/5} = \left[ \sum_{i=1}^6 |p_i| (a^i)^{5/2} \right]^{2/5} = a \quad (\text{A.25}) \end{aligned}$$

Bounds  $b$  are derived in a similar manner to obtain

$$\sup_{\xi \in \mathcal{R}^3} |\xi_1| |F|^{1/5} \leq \left[ \sum_{i=1}^6 |p_i| (b_1^i)^5 \right]^{1/5} = b_1 \quad (\text{A.26})$$

$$\sup_{\xi \in \mathcal{R}^3} |\xi_2| |F|^{1/5} \leq \left[ \sum_{i=1}^6 |p_i| (b_2^i)^5 \right]^{1/5} = b_2 \quad (\text{A.27})$$

$$\sup_{\xi \in \mathcal{R}^3} |\xi_3| |F|^{1/5} \leq \left[ \sum_{i=1}^6 |p_i| (b_3^i)^5 \right]^{1/5} = b_3. \quad (\text{A.28})$$

Using bounds (A.25–A.28), the overall process of sampling particles to construct a representation of the deviational distribution  $F$  in the form  $mW_{\text{eff}} \sum_{k=1}^N s_k \delta^3(\xi - \xi_j)$  proceeds by first drawing a trial number  $N_{\text{trial}}$  of particles, which is determined by the total integral bound on the distribution

$$\begin{aligned} \frac{1}{mW_{\text{eff}}} \int_{\mathcal{R}^3} d^3 \xi |F| &= \frac{1}{mW_{\text{eff}}} \int_{\mathcal{R}^3} d^3 \eta \frac{\partial(|F|, \xi)}{\partial(H, \eta)} \Big|_H \\ &\leq \frac{1}{mW_{\text{eff}}} \int_{-b_1}^{b_1} d\eta_1 \int_{-b_2}^{b_2} d\eta_2 \int_{-b_3}^{b_3} d\eta_3 \frac{5}{2} a = \frac{20ab_1b_2b_3}{mW_{\text{eff}}} = N^{\text{trial}}, \quad (\text{A.29}) \end{aligned}$$

where extensions to distributions over different domains are obvious (for example, if  $0 \leq \xi_1 \leq \mathcal{R}$ , then  $N_{\text{trial}}$  is reduced by half, etc.). Note that the Jacobian of the transformation was used in the derivation above.

Finally, the samples are generated by repeating the following steps  $N^{\text{trial}}$  times: (i) draw a set of independent random variables  $H, \eta$  uniformly distributed according to bounds (A.25–A.28), (ii) determine trial sample independent variable  $\xi = \eta/\sqrt{H}$ , (iii) if  $H < |F(\xi)|^{2/5}$  then accept the particle with sign  $\text{sgn}(F)$ .

### A.3.2 Ratio of uniforms sampling of $2\xi^3 e^{-\xi^2}$

In this section, a simple application of the ratio-of-uniforms method is presented by developing an algorithm for producing samples  $\xi \in [0, \infty)$  from the probability distribution  $p(\xi) = 2\xi^3 e^{-\xi^2}$ . Using the one-dimensional formulation from Reference [62] (with  $r = 1/2$ ), the desired variable transformation is

$$\xi = \eta/\sqrt{H} \tag{A.30}$$

$$p = H^{3/2}, \tag{A.31}$$

where the bounds on the transformed variables were calculated to be

$$a = \sup_{\xi \in [0, \infty)} p^{2/3} = \frac{3}{2^{1/3}e} \tag{A.32}$$

$$b = \sup_{\xi \in [0, \infty)} \xi p^{1/3} = \frac{2^{1/3}3}{e}. \tag{A.33}$$

This results in the following algorithm, used in Section 4.3.1 to produce a single sample  $\xi$ .

**Algorithm A.1.** Algorithm for sampling  $2\xi^3 e^{-\xi^2}$

1. Generate a uniform random variate  $\mathfrak{R}_1 \in [0, 1)$ , and calculate  $H = 3\mathfrak{R}_1/(2^{1/3}e)$ .

2. Generate a uniform random variate  $\mathfrak{R}_2 \in [0, 1)$ , and calculate  $\xi = 2^{1/3}3\mathfrak{R}_2/e$ .
3. If  $H < (2\xi^3e^{-\xi^2})^{2/3}$  then exit routine with sample  $\xi$ .
4. Go back to step 1.

# Appendix B

## Mass-conservative Simulation Based on a Local Equilibrium

This section contains the modifications to the LVDSMC algorithm described in Chapter 7 for simulating deviation from a spatially-variable equilibrium distribution  $f^{\text{MB}}$ . Unlike previous approaches [33, 52], the equilibrium is not updated during the collision step. This simpler approach was chosen; as this procedure was only required for a single application (uniform heat generation, presented in Section 7.2); a simulation method for the VHS model with automatically updated equilibrium would be considerably more complex and was not presented.

The spatially-variable equilibrium distribution is defined as

$$f^{\text{MB}}(\mathbf{c}) = \frac{\rho_{\text{MB}}}{\pi^{3/2} c_{\text{MB}}^3} \exp\left(-\frac{\|\mathbf{c} - \mathbf{u}_{\text{MB}}\|^2}{c_{\text{MB}}^2}\right), \quad c_{\text{MB}} = \sqrt{2RT_{\text{MB}}}, \quad (\text{B.1})$$

where the hydrodynamic properties  $(\rho_{\text{MB}}, \mathbf{u}_{\text{MB}}, T_{\text{MB}})$  are cell-based values. For simplicity, the implemented method is based on a motionless equilibrium state:  $\mathbf{u}_{\text{MB}} = \mathbf{u}_0 = \mathbf{0}$ . The advection routine is an extension of the procedure developed in Reference [52] and discussed in Section 2.3, only extended to include mass conservation and to treat moderate departures from equilibrium.

## B.1 Advection step

Using the spatially-variable equilibrium distribution, the advection step for deviational particles (2.7) retains the term on the right hand side.

$$\left[ \frac{\partial f^d(\mathbf{c})}{\partial t} + \mathbf{c} \cdot \frac{\partial f^d(\mathbf{c})}{\partial \mathbf{x}} \right]_{\text{adv}} = -\mathbf{c} \cdot \frac{\partial f^{\text{MB}}(\mathbf{c})}{\partial \mathbf{x}} \quad (\text{B.2})$$

The left hand side of the above equation corresponds precisely to the advection procedures for simulating deviation from a fixed equilibrium distribution (Section 3.2), which forms the homogeneous solution. The homogenous part of the solution requires generation of additional particles at every cell interface, in addition to the boundaries of the simulation domain, in order to account for the discontinuities of the equilibrium  $f^{\text{MB}}$  across the cell interfaces; each is discussed in turn.

The procedure for generating particles at the boundaries is only slightly modified from the the previously considered version to account for different equilibrium states in the cells next to the boundary. Specifically, for Equations (3.9), (3.12–3.14), (3.32), and (3.38), the properties  $(\rho_0, c_0)$  are replaced by  $(\rho_{\text{MB},\ell_k}, c_{\text{MB},\ell_k})$ , where  $\ell_k$  is the index of cell touching surface element  $\Delta A_k$ . An additional step consists of sampling particles from the distribution below for each cell interface  $k$  [33].

$$\mathcal{F}_{\text{int},k} \Delta A_k^{\text{int}} \Delta t_{\text{adv}} d^3 \mathbf{c} = \mathbf{c} \cdot \mathbf{n}_k^{\text{int}} \left[ f_{\ell_k^-}^{\text{MB}} - f_{\ell_k^+}^{\text{MB}} \right] (\mathbf{c}) \Delta A_k \Delta t_{\text{adv}} d^3 \mathbf{c} \quad (\text{B.3})$$

In the above, we introduce additional notations for the  $k^{\text{th}}$  cell interface; defined between cell indices  $\ell_k^\pm$  with shared surface area  $\Delta A_k^{\text{int}}$  and surface normal  $\mathbf{n}_k^{\text{int}}$  which points from cell  $\ell_k^-$  to  $\ell_k^+$ .

Generating particles on the cell interfaces is performed by a similar approach to generating particles on the boundary surface elements; a key difference being that particles are emitted from the surface in all directions. The required procedure is nearly identical with the one presented in Section 3.2.1; this is presented below, where without loss of generality, the surface normal  $\mathbf{n}_k^{\text{int}}$  is assumed to be in the positive  $x$  direction.

First, the ratio-of-uniforms sampling bound estimates are evaluated

$$\begin{bmatrix} (a^{\text{MB}0,k})^{5/2} \\ (b_x^{\text{MB}0,k})^5 \\ (b_y^{\text{MB}0,k})^5 \\ (b_z^{\text{MB}0,k})^5 \end{bmatrix} = \frac{1}{\pi^{3/2}} \begin{bmatrix} 1/\sqrt{2e} & [3/(2e)]^{3/2} \\ (3/e)^3 & (4/e)^4 \\ 5^{5/2}/(2e)^3 & 20^{5/2}/(27e^4) \\ 5^{5/2}/(2e)^3 & 20^{5/2}/(27e^4) \end{bmatrix} \cdot \begin{bmatrix} \frac{\rho_{\text{MB},\ell_k^-} - \rho_{\text{MB},\ell_k^+}}{\rho_{\text{MB},k}} - 3 \frac{c_{\text{MB},\ell_k^-} - c_{\text{MB},\ell_k^+}}{c_{\text{MB},k}} \\ 2 \frac{|c_{\text{MB},\ell_k^-} - c_{\text{MB},\ell_k^+}|}{c_{\text{MB},k}} \end{bmatrix}, \quad (\text{B.4})$$

in terms of the average properties of the cells  $\ell_k^\pm$

$$\overline{\rho_{\text{MB}}} = \frac{1}{2} (\rho_{\text{MB},\ell_k^-} + \rho_{\text{MB},\ell_k^+}) \quad (\text{B.5})$$

$$\overline{c_{\text{MB},k}} = \frac{1}{2} (c_{\text{MB},\ell_k^-} + c_{\text{MB},\ell_k^+}). \quad (\text{B.6})$$

These bounds (B.4) are corrected by numerical factors, which are dynamically updated in the identical manner to Equations (3.34–3.37).

$$a^{\text{MB},k} = Y_a^{\text{MB}} a^{\text{MB}0,k} \quad (\text{B.7})$$

$$b_x^{\text{MB},k} = Y_{b,x}^{\text{MB}} b_x^{\text{MB}0,k} \quad (\text{B.8})$$

$$b_y^{\text{MB},k} = Y_{b,y}^{\text{MB}} b_y^{\text{MB}0,k} \quad (\text{B.9})$$

$$b_z^{\text{MB},k} = Y_{b,z}^{\text{MB}} b_z^{\text{MB}0,k} \quad (\text{B.10})$$

The overall sampling procedure consists of

$$N_{\text{B},k}^{\text{trial}} = 10 \frac{\alpha_k \overline{\rho_{\text{B},k}} \overline{c_{\text{B},k}} \Delta A_k \Delta t_{\text{adv}}}{mW_{\text{eff}}} a^{\text{B},k} b_x^{\text{B},k} b_y^{\text{B},k} b_z^{\text{B},k} \quad (\text{B.11})$$

trial steps, in which a uniform sample  $(H, \boldsymbol{\eta})$  is generated using bounds

$$0 \leq H \leq a^{\text{MB},k} \quad (\text{B.12})$$

$$-b_x^{\text{MB},k} \leq \eta_x \leq b_x^{\text{MB},k} \quad (\text{B.13})$$

$$-b_y^{\text{MB},k} \leq \eta_y \leq b_y^{\text{MB},k} \quad (\text{B.14})$$

$$-b_z^{\text{MB},k} \leq \eta_z \leq b_z^{\text{MB},k}, \quad (\text{B.15})$$

and the corresponding trial particle velocity is determined via  $\mathbf{c} = \overline{c_{\text{MB},k}} \boldsymbol{\eta} / \sqrt{H}$ . The function  $F^{\text{MB},k}(\mathbf{c})$  is evaluated, and particles are accepted when  $H < |F^{\text{MB},k}(\mathbf{c})|^{2/5}$ . Accepted particles are advected a random fraction of the advective time step away (performing ordinary DSMC reflection procedures for any subsequent boundary interactions) from a uniformly distributed random position on the boundary interface element  $\Delta A_k^{\text{int}}$  and added to the simulation with sign  $\text{sgn}[F^{\text{MB},k}(\mathbf{c})]$ .

Since (like the boundary sampling distribution) the cell interface sampling distribution has zero mass

$$\int_{\mathcal{R}^3} d^3 \mathbf{c} \left[ \frac{\partial f(\mathbf{c})}{\partial t} \right]_{\text{int},k} = 0, \quad (\text{B.16})$$

mass conservation is again implemented by the stratified sampling approach as before (Section 3.2.2).

## B.2 Collision step

The modifications to the collision step due to a spatially-variable equilibrium are minimal, and result from the fact that the collision kernels, as well as the collision rate function are now defined in terms of the spatially-variable equilibrium, i.e.:

$$K_{\beta}^{(1)}(\mathbf{c}, \mathbf{c}_*) = \frac{4C_{\beta}}{\|\mathbf{c} - \mathbf{c}_*\|} \int_{\Gamma_{\perp}(\mathbf{c} - \mathbf{c}_*)} d^3\zeta \frac{f^{\text{MB}}(\mathbf{c} + \zeta)}{\|\mathbf{c} - \mathbf{c}_* - \zeta\|^{1-\beta}} \quad (\text{B.17})$$

$$K_{\beta}^{(2)}(\mathbf{c}, \mathbf{c}_*) = 4\pi C_{\beta} \|\mathbf{c} - \mathbf{c}_*\|^{\beta} f^{\text{MB}}(\mathbf{c}) \quad (\text{B.18})$$

$$\nu_{\beta}(\mathbf{c}) = 4\pi C_{\beta} \int_{\mathcal{R}^3} d^3\mathbf{c}_* \|\mathbf{c} - \mathbf{c}_*\|^{\beta} f^{\text{MB}}(\mathbf{c}_*). \quad (\text{B.19})$$

The entire procedure in Chapter 4 can be implemented as before, by replacing  $f^0$ , as well as its properties  $(\rho_0, \mathbf{u}_0, c_0)$  by the spatially-variable equilibrium  $f^{\text{MB},j}$  and its properties  $(\rho_{\text{MB},j}, \mathbf{u}_{\text{MB},j}, c_{\text{MB},j})$ , where  $j$  is the appropriate cell index.



# Bibliography

- [1] H. A. Al-Mohssen. *An Excursion with the Boltzmann Equation at Low Speeds: Variance-Reduced DSMC*. PhD thesis, Massachusetts Institute of Technology, 2010.
- [2] H. A. Al-Mohssen and N. G. Hadjiconstantinou. Low-variance direct Monte Carlo using importance weights. *ESAIM: Mathematical Modelling and Numerical Analysis*, 44(5):1069–1083, 2010.
- [3] F. J. Alexander and A. L. Garcia. The direct simulation Monte Carlo method. *Computers in Physics*, 11(6):588–593, 1997.
- [4] A. A. Alexeenko, S. F. Gimelshein, E. P. Muntz, and Ketsdever A. Modeling of thermal transpiration flows for Knudsen compressor optimization. In *Proceedings of the 43rd AIAA Aerospace Sciences Meeting and Exhibit, Reno, Nevada, 2005*.
- [5] M. R. Allshouse and N. G. Hadjiconstantinou. Low-variance deviational Monte Carlo simulations of pressure driven flow in micro- and nanoscale channels. In *Proceedings of the 26th International Symposium on Rarefied Gas Dynamics, Kyoto, Japan*, pages 1015–1020, 2008.
- [6] P. Andries, J-F. Bourgat, P. le Tallec, and B. Perthame. Numerical comparison between the Boltzmann and ES-BGK models for rarefied gases. *Computer Methods in Applied Mechanics and Engineering.*, 191(31):3369–3390, 2002.
- [7] S. Asmussen and P. W. Glynn. *Stochastic Simulation: Algorithms and Analysis*. Springer, New York, 2007.
- [8] L. L. Baker. *Efficient numerical methods for solving the Boltzmann equation for small scale flows*. PhD thesis, Massachusetts Institute of Technology, 2007.
- [9] L. L. Baker and N. G. Hadjiconstantinou. Variance reduction for Monte Carlo solutions of the Boltzmann equation. *Physics of Fluids*, 17(5):051703, 2005.
- [10] L. L. Baker and N. G. Hadjiconstantinou. Variance reduction in particle methods for solving the Boltzmann equation. In *Proceedings of the 4th International Conference on Nanochannels, Microchannels and Minichannels, Limerick, Ireland*, pages 377–383, 2006.

- [11] L. L. Baker and N. G. Hadjiconstantinou. Variance-reduced particle methods for solving the Boltzmann equation. *Journal of Computational and Theoretical Nanoscience*, 5(2):165–174, 2008.
- [12] P. L. Bhatnagar, E. P. Gross, and M. Krook. A model for collision processes in gases. I. Small amplitude processes in charged and neutral one-component systems. *Physical Review*, 94(3):511–525, 1954.
- [13] G. A. Bird. Monte Carlo simulation in an engineering context. *Progress in Astronautics and Aeronautics*, 74:239–255, 1981.
- [14] G. A. Bird. *Molecular Gas Dynamics and the Direct Simulation of Gas Flows*. Clarendon Press, Oxford, 1994.
- [15] C. Borgnakke and P. S. Larsen. Statistical collision model for Monte Carlo simulation of polyatomic gas mixture. *Journal of Computational Physics*, 18(4):405–420, 1975.
- [16] C. Cercignani. *The Boltzmann Equation and its Applications*. Springer Verlag, New York, 1988.
- [17] C. Cercignani. *Mathematical Methods in Kinetic Theory*. Plenum Press, New York, second edition, 1990.
- [18] C. Cercignani. *Slow Rarefied Flows: Theory and Application to Micro-Electro-Mechanical Systems*. Birkhauser-Verlag, Basel, 2006.
- [19] C. Cercignani and A. Daneri. Flow of a rarefied gas between two parallel plates. *Journal of Applied Physics*, 34(12):3509–3513, 1963.
- [20] G. Chen. Ballistic-diffusive equations for transient heat conduction from nano to macroscales. *Journal of Heat Transfer*, 124(2):320–328, 2002.
- [21] G. Chen. *Nanoscale Energy Transfer and Conversion*. Oxford, USA, 2005.
- [22] J. Chun and D. L. Koch. A direct simulation Monte Carlo method for rarefied gas flows in the limit of small mach number. *Physics of Fluids*, 17(10):107107, 2005.
- [23] G. Dimarco and L. Pareschi. On the application of the BGK kinetic model to the analysis of gas-structure interactions in MEMS. *Computers and Structures*, 85(11–14):810–817, 2007.
- [24] T. Doi. Numerical analysis of the Poiseuille flow and the thermal transpiration of a rarefied gas through a pipe with a rectangular cross section based on the linearized Boltzmann equation for a hard sphere molecular gas. *Journal of Vacuum Science and Technology A*, 28(4):603–612, 2010.

- [25] M. A. Gallis and J. R. Torczynski. An improved Reynolds-equation model for gas damping of microbeam motion. *Journal of Microelectromechanical Systems*, 13(4):653–659, 2004.
- [26] A. L. Garcia. *Numerical Methods for Physics*. Prentice-Hall, Upper Saddle River, NJ, USA, second edition, 1999.
- [27] N. G. Hadjiconstantinou. The limits of Navier-Stokes theory and kinetic extensions for describing small-scale gaseous hydrodynamics. *Physics of Fluids*, 18(11):111301, 2006.
- [28] N. G. Hadjiconstantinou, A. L. Garcia, M. Z. Bazant, and G. He. Statistical error in particle simulations of hydrodynamic phenomena. *Journal of Computational Physics*, 187(1):274–297, 2003.
- [29] N. G. Hadjiconstantinou, G. A. Radtke, and L. L. Baker. On variance reduced simulations of the Boltzmann transport equation for small-scale heat transfer applications. *Journal of Heat Transfer*, 132(11):112401, 2010.
- [30] Y. L. Han, E. P. Muntz, A. Alexeenko, and Y. Markus. Experimental and computational studies of temperature gradient-driven molecular transport in gas flows through nano/microscale channels. *Nanoscale and Microscale Thermophysical Engineering*, 11(1–2):151–175, 2007.
- [31] T. M. M. Homolle. Efficient particle methods for solving the Boltzmann equation. Master’s thesis, Massachusetts Institute of Technology, Cambridge, MA, 2008.
- [32] T. M. M. Homolle and N. G. Hadjiconstantinou. Low-variance deviational simulation Monte Carlo. *Physics of Fluids*, 19(4):041701, 2007.
- [33] T. M. M. Homolle and N. G. Hadjiconstantinou. A low-variance deviational simulation Monte Carlo for the Boltzmann equation. *Journal of Computational Physics*, 226(2):2341–2358, 2007.
- [34] A. A. Joshi and A. Majumdar. Transient ballistic and diffusive phonon heat transport in thin films. *Journal of Applied Physics*, 74(1):31–39, 1993.
- [35] T. A. Klein. Master’s thesis, Massachusetts Institute of Technology, Cambridge, MA, in progress.
- [36] M. Knudsen. Die Gesetze der Molekularströmung und der inneren Reibungsströmung der Gase durch Röhren. *Annals of Physics*, 333(1):75–130, 1909.
- [37] C. D. Landon. Weighted particle variance reduction of direct simulation Monte Carlo for the Bhatnagar-Gross-Krook collision operator. Master’s thesis, Massachusetts Institute of Technology, Cambridge, MA, 2010.
- [38] C. D. Landon. PhD thesis, Massachusetts Institute of Technology, Cambridge, MA, in progress.

- [39] C. D. Landon and Hadjiconstantinou. Variance-reduced direct simulation Monte Carlo with the Bhatnagar-Gross-Krook collision operator. In *Proceedings of the 27th International Symposium on Rarefied Gas Dynamics, Pacific Grove, CA*, pages 277–282, 2011.
- [40] S. K. Loyalka and J. W. Jr. Cipolla. Thermal creep slip with arbitrary accommodation at the surface. *Physics of Fluids*, 14(6):1656–1661, 1975.
- [41] S. K. Loyalka, N. Petrellis, and T. S. Storick. Some numerical results for the BGK model: thermal creep and viscous slip problems with arbitrary accommodation at the surface. *Physics of Fluids*, 18(9):1094–1099, 1975.
- [42] M. Lundstrom. *Fundamentals of Carrier Transport*. Cambridge University Press, Cambridge, second edition, 2000.
- [43] M. N. Macrossan. A particle simulation method for the BGK equation. In *Proceedings of the 22nd International Conference on Rarefied Gas Dynamics, Sydney, Australia*, pages 426–433, 2001.
- [44] A. Manela and N. G. Hadjiconstantinou. Gas motion induced by unsteady boundary heating in a small-scale slab. *Physics of Fluids*, 20(11):117104, 2008.
- [45] A. Manela and N. G. Hadjiconstantinou. Gas-flow animation by unsteady heating in a microchannel. *Physics of Fluids*, 22(6):062001, 2010.
- [46] E. P. Muntz, Y. Sone, K. Aoki, S. Vargo, and Young M. Performance analysis and optimization considerations for a Knudsen compressor in transitional flow. *Journal of Vacuum Science and Technology A.*, 20(1):214–224, 2002.
- [47] T. Ohwada. Higher order approximation methods for the Boltzmann equation. *Journal of Computational Physics*, 139(1):1–14, 1998.
- [48] H. C. Öttinger. *Stochastic processes in polymeric fluids*. Springer-Verlag, New York, 1995.
- [49] J-P. M. Peraud. Low variance methods for Monte Carlo simulation of phonon transport. Master’s thesis, Massachusetts Institute of Technology, Cambridge, MA, 2011.
- [50] W. H. Press, S. A. Teukolsky, W. T. Vetterling, and B. P. Flannery. *Numerical Recipes. The Art of Scientific Computing*. Cambridge University Press, third edition, 2007.
- [51] D. J. Rader, M. A. Gallis, J. R. Torczynski, and W. Wagner. Direct simulation Monte Carlo convergence behavior of the hard-sphere-gas thermal conductivity for Fourier heat flow. *Physics of Fluids*, 18(7):077102, 2006.
- [52] G. A. Radtke and N. G. Hadjiconstantinou. Variance-reduced particle simulation of the Boltzmann transport equation in the relaxation-time approximation. *Physical Review E*, 79(5):056711, 2009.

- [53] G. A. Radtke, N. G. Hadjiconstantinou, and W. Wagner. Low-noise Monte Carlo simulation of the variable hard sphere gas. *Physics of Fluids*, 23(3):030606, 2011.
- [54] G. A. Radtke, N. G. Hadjiconstantinou, and W. Wagner. Low variance particle simulations of the Boltzmann transport equation for the variable hard sphere collision model. In *Proceedings of the 27th International Symposium on Rarefied Gas Dynamics, Pacific Grove, CA*, pages 307–312, 2011.
- [55] G. A. Radtke, J-P. M. Peraud, and N. G. Hadjiconstantinou. On multiscale particle simulations of kinetic transport. *Philosophical Transactions of the Royal Society*, submitted.
- [56] S. Ramanathan and D. L. Koch. An efficient direct simulation Monte Carlo method for low Mach number noncontinuum gas flows based on the Bhatnagar-Gross-Krook model. *Physics of Fluids*, 21(3):033103, 2009.
- [57] Y. Sone. *Molecular Gas Dynamics: Theory, Techniques, and Applications*. Birkhauser, Boston, 2007.
- [58] S. Takata, H. Sugimoto, and S. Kosuge. Gas separation by means of the Knudsen compressor. *European Journal of Mechanics B*, 26(2):155–181, 2007.
- [59] W. G. Vincenti and C. H. Kruger. *Introduction to Physical Gas Dynamics*. Wiley, New York, 1965.
- [60] W. Wagner. A convergence proof for Bird’s direct simulation Monte Carlo method for the Boltzmann equation. *Journal of Statistical Physics*, 66(3–4):1011–1044, 1992.
- [61] W. Wagner. Deviation particle Monte Carlo for the Boltzmann equation. *Monte Carlo Methods and Applications*, 14(3):191–268, 2008.
- [62] J. C. Wakefield, A. E. Gelfand, and A. F. M. Smith. Efficient generation of random variates via the ratio-of-uniforms method. *Statistics and Computing*, 1(2):129–133, 1991.